Low-friction surfaces with recoverable super-hydrophobicity for water transmission

Liliane C. C. Auwerter

Imperial College London

Department of Civil and Environmental Engineering
Imperial College London

Submitted in part fulfilment of the requirements for the degree of Doctor of Philosophy in Civil and Environmental Engineering of Imperial College London.

Low-friction surfaces with recoverable super-hydrophobicity for water transmission

Liliane C. C. Auwerter

Under supervision of Dr Maarten van Reeuwijk, Prof. Christopher Cheeseman and Prof. Michael Templeton

Abstract

Super-hydrophobic surfaces are of considerable interest as they can reduce friction losses and thus lead to substantial reductions in the energy consumption of water distribution networks. However, super-hydrophobic surfaces are not durable, as they are known to lose their friction-reducing properties rapidly due to loss of small air-pockets in the roughness elements of the surface. This thesis describes the development and testing of a novel porous low-friction surface with recoverable super-hydrophobicity for use under fully turbulent water flow conditions.

Preliminary experiments carried out as part of this dissertation showed that samples with super-hydrophobic coatings immersed in water lost their super-hydrophobicity quickly due to depletion of trapped air. Furthermore, the loss of particles on the surface that form the surface structure can lead to irreversible loss of super-hydrophobicity. Therefore a durable super-hydrophobic surface was designed and manufactured, using sintered soda-lime glass granules that provided an increased level of particle bonding compared to coatings.

The surface of the materials was made hydrophobic through a reaction with one of several surface modifying agents. Combinations of granules of five different particle sizes and three different surface modifying agents (hexamethyldisilazane, trichloro-(1H,1H,2H,2H-perfluorooctyl)silane and 1H,1H,2H,2H-perfluorooctyltriethoxysilane) were considered. The hydrophobicity of the materials was analysed by measuring

the water contact angle. The best performing material, sample ST, showed a mean water contact angle of 153°. The surface and structure of the best performing samples were characterised using scanning electron microscopy (SEM), x-ray tomography and Fourier Transformed Infra-red (FTIR) spectroscopy. FTIR spectroscopy confirmed the reaction between trichloro- (1H,1H,2H,2H-perfluorooctyl)silane and the soda-lime glass substrate. SEM micrographs showed that samples formed with smaller particle sizes presented 30% less peak areas than surfaces formed with larger particle sizes, and x-ray tomography showed that samples formed with smaller particle sizes presented higher relative surface roughness, with features up to 30 μm size. Lower peak area and high relative surface roughness affect the area of contact on the solid-liquid interface, and consequently the attachment of a liquid on a solid surface. X-ray tomography analysis showed that samples were porous throughout the material, with tile porosity in the range of 23-36% with mean pore size of 8-15 μm. The porosity of the material allowed for replenishment of the air pockets by pressurising an air layer on the other side of the surface which forces air through the material. This can take place under fully immersed conditions, allowing the material to recover its super-hydrophobicity.

The ability of the material to recover its super-hydrophobic properties was investigated experimentally in fully immersed setups under quiescent conditions and under turbulent flow conditions. Fully immersed conditions results showed recovery of the air pockets at the liquid-solid interface under both quiescent and turbulent flow conditions.

Under quiescent conditions the experiment was performed by exposing the samples to static water to a depth of 10 mm and applying an air pressure of 0.04 bar. The recovery of air pockets was analysed qualitatively by capturing the formation of air pockets and bubbles on the surface.

The turbulent flow experiments measured the friction factor f_d as a function of time. Values of f_d were obtained by measuring the pressure drop and volume flux. The

Reynolds number of the flow was approximately 4.5×10^4 for all experiments. Turbulent flow results showed reductions in f_d of 31-45% relative to a hydraulically smooth surface. The Cassie-Baxter state could be recovered by blowing air through the porous surface for 10 minutes. The durability of the drag-reduction, as quantified by the relaxation time T in which the surface loses its super-hydrophobic characteristics, were measured to be between 10-60 minutes depending on the initial head.

In contrast to models based on Darcy flow through a porous medium, this study indicates that there seems to be a critical water pressure beyond which the Cassie-Baxter state cannot be sustained for the material under consideration, which limits its use for water distribution purposes.

All the work presented in this thesis is that of the author. Any work or contributions made by others is referenced appropriately.

Liliane C. C. Auwerter

April 13, 2020

Acknowledgements

I would like to thank my supervisors Maarten van Reeuwijk, Christopher Cheeseman and Michael R. Templeton for the many helpful discussions and support during this project, allowing me to grow as a researcher. Maarten, Chris and Mike have always been very positive towards this multidisciplinary project and gave me the chance to explore this novel research field.

I would like to acknowledge support from David De Ruyter for his direct technical help with SolidWorks® and all the other steps that involved assembly of the experimental apparatus, and the technical staff across many departments that made it possible to obtain various analysis of samples. In addition, all my fluid dynamics lab peers, specially Ivo and my office, that helped me with all Matlab® and LaTeX debugging and hours of discussing flow on super-hydrophobic surfaces.

Finally I would like to thank all my friends and family for their love and support.

The research for this work was supported by the UK Engineering and Physical Sciences Research Council (EPSRC) who fund Centre for Doctoral Training in Sustainable Civil Engineering in the Department of Civil and Environmental Engineering at Imperial College London via grant EP/L016826/1.

List of Publications

Auwerter, C.C. L., Templeton, R. M., van Reeuwijk, M., Taiwo, O. O., Cheeseman, C. (2019). Development of porous glass surfaces with recoverable hydrophobicity. *Materials Letters: X*, 1, 100002. https://doi.org/10.1016/j.mlblux.2019.100002.

Auwerter, C.C. L., Templeton, R. M., van Reeuwijk, M., Cheeseman, C. (2019). Friction-reducing surfaces with recoverable super-hydrophobicity. ***Under review***.

Contents

List of figures

List of tables

Key symbols and abbreviations

Abbreviations

Me Methyl, CH_3

CVD Chemical Vapour Deposition

DPD N,N-diethyl-p-phenylenediamine

EGL Energy Grade Line

FTIR Fourier Transformed Infra-Red

HGL Hydraulic Grade Line

HMDS Hexamethyldisilazane

PFTS Trichloro(1H,1H,2H,2H-perfluorooctyl)silane

POTS 1H,1H,2H,2H-perfluorooctyltriethoxysilane

PTFE Polytetrafluoroethylene (Teflon)

SEM Scanning Electron Microscopy

SMA Surface modifying agent

UV Ultraviolet

WHO World Health Organisation

Constants

μ Dynamic viscosity [$\mathtt{N\ s\ m^{-2}}$]

ν Kinematic viscosity [$\mathtt{m^2\ s^{-1}}$]

ρ Density [$\mathtt{kg\ m^{-3}}$]

g Gravitational acceleration of Earth [$\mathtt{m\ s^{-2}}$]

Symbols

ΔH Head loss [$\mathtt{m}$]

Δp Pressure drop [$\mathtt{Pa}$]

δ Channel height [$\mathtt{m}$]

δ_* Thickness of viscous sublayer [$\mathtt{m}$]

ℓ_s Slip length [$\mathtt{m}$]

γ_{LG} Surface tension [$\mathtt{J\ m^{-2}}$]

γ_{SG} Solid-vapour interfacial energy [$\mathtt{J\ m^{-2}}$]

γ_{SL} Solid-liquid interfacial energy [$\mathtt{J\ m^{-2}}$]

κ Permeability coefficient [$\mathtt{m^2}$]

ν_t Turbulent viscosity [$\mathtt{m^2\ s^{-1}}$]

Re Reynolds number [-]

Re_s Roughness Reynolds number [-]

τ_w Shear stress [$\mathtt{kg\ m^{-1}\ s^{-2}}$]

θ Apparent water droplet-solid surface contact angle [°]

θ_L Water droplet-smooth solid surface contact angle [°]

ε Wall Roughness [m]

A Area [m^2]

D Pipe diameter [m]

d Flat projected size of roughness length [m]

d_g Soda-lime glass particle size [m]

D_h Hydraulic diameter [m]

d_s Thickness of super-hydrophobic surface [m]

DR Drag reduction [%]

E Total energy along a streamline [J m^{-3}]

f_0 Initial friction factor [-]

f_c Friction factor in the Cassie-Baxter state [-]

f_d Darcy-Weisbach friction factor [-]

f_w Friction factor in the Wenzel state [-]

H Energy head [m]

h Piezometric head [m]

L Length [m]

P Perimeter [m]

p Pressure [Pa]

P_w Power [W]

Q Flow rate [m^3 s^{-1}]

q Darcy velocity [$\mathtt{m\ s^{-1}}$]

R_f Relative surface roughness [-]

RA Rolling angle [$\mathtt{^\circ}$]

T Relaxation time [$\mathtt{s}$]

U Average fluid velocity over the pipe cross-section [$\mathtt{m\ s^{-1}}$]

u Reynolds averaged velocity [$\mathtt{m\ s^{-1}}$]

u_w Slip velocity [$\mathtt{m\ s^{-1}}$]

u_* Friction velocity [$\mathtt{m\ s^{-1}}$]

z Elevation above reference plane [$\mathtt{m}$]

1

Introduction

Transporting of liquids in pipes is an energy intensive activity. From catchment to screening, treatment, and distribution, the energy consumed worldwide by the water industry in 2016 was 850 TWh. Most of this energy was consumed in the form of electricity, representing around 4% of global electricity consumption which is equivalent to the total energy demand of Australia (IEA, 2016). For water to be transported from the reservoir to its destination, a substantial amount of energy is needed – Boulos & Bros (2010) estimate that friction energy losses in the water industry range from 2.3 to 26.8% of the total energy lost, including losses at valves and customer taps based on a study conducted with eight European water distribution networks.

Energy losses in pipe networks are usually categorised in two classes: major and minor losses. Major losses are losses due to friction with the pipe walls, whereas minor losses comprise of entrance and exit losses, changes in the pipe cross-sections (contractions/expansion) and junctions, among others (Jones, 2011a). To provide a simple illustration of the required power to maintain a volume flux Q (m^3/s) in a pipe of diameter D with a fluid of density ρ (kg/m^3), we assume that all losses are

due to friction (major losses). In this case, the power P_w is given by (Nakayama, 2018):

$$P_w = a\rho\overline{f}_d U^3 \tag{1.1}$$

where $U = Q/A$ is the cross-sectionally averaged velocity, $\overline{f}_d$ is mean the friction factor of the pipe, $a = (AL)/(2D)$ encapsulates the pipe geometry, $A = \pi D^2/4$ is the cross-sectional area and L is the pipe length. The equation above shows that the largest energy reduction can be obtained by reducing the velocity in the pipe, for example by making the pipe diameter D very large. However, apart from the costs associated with very large diameter pipes, low velocities will cause organic and inorganic particle sedimentation, which is undesirable (Bennett & Glaser, 2011). Thus, assuming that the velocity U and diameter D are determined by other considerations, the main parameter to reduce energy consumption is to reduce the pipe friction factor f_d. Friction forces occur on the area of contact between the material of the pipe and the fluid, and are dependent on the physical and chemical characteristics of the material of the pipe, e.g. roughness and surface energy.

Friction is the force that resists the relative motion of fluids and solid surfaces sliding against each other (Kay, 1998). Friction forces in a water pipe are the result of the interaction between the fluid and surface of the pipe. Two main factors cause wall friction: 1) skin friction and 2) inertia caused by roughness elements 'blocking' the flow. Skin friction is caused by the chemical interaction between the surface of the pipe and the fluid. Hydrogen bonds and Van Der Waals forces act as a weak adhesive on the fluid-solid interface (Nosonovsky & Bhushan, 2008a), and wall roughness causes resistance to the fluid close to the wall (Colebrook & White, 1937). To investigate the effect of roughness on wall friction, Colebrook and White[1], among others experimented passing fluid flow (e.g. air or water) in pipes with various internal wall roughnesses (Colebrook & White, 1937, Nikuradse, 1933). The influence of wall roughness is shown in the Moody diagram in Figure (1.1). The Moody

[1]In the Hydrodynamics Laboratory in the Department of Civil and Environmental Engineering at Imperial College London

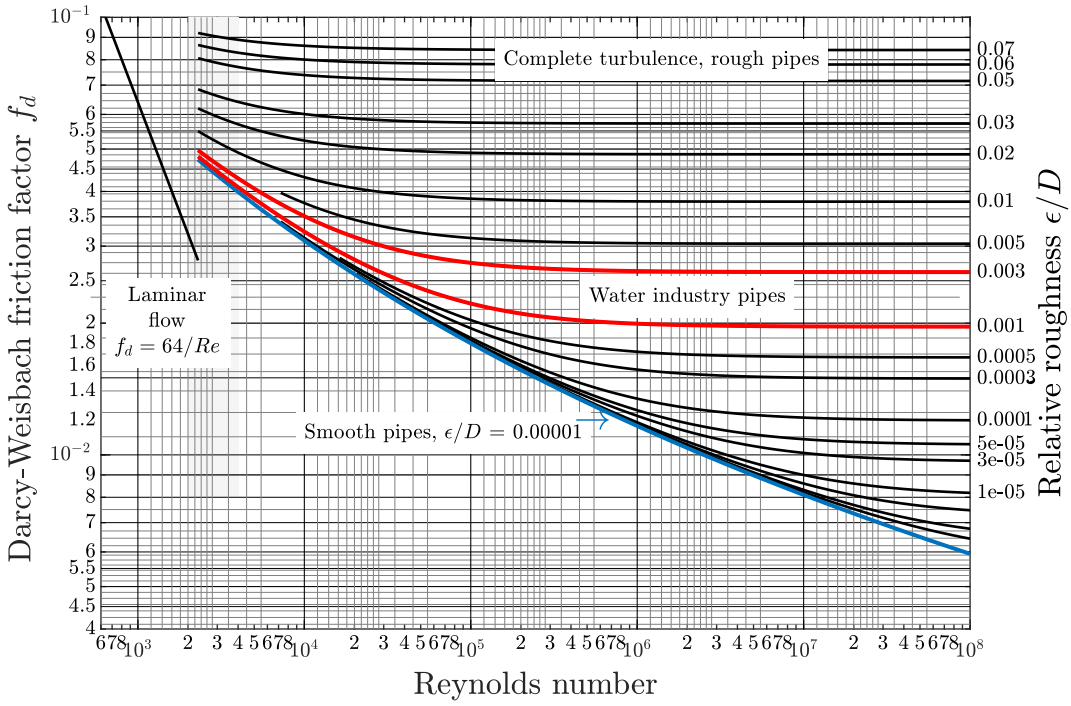

FIGURE 1.1: Moody Diagram (Munson et al., 2009)

diagram presents the observed correlation between wall roughness (ε), wall friction factor (f_d), and Reynolds number from experiments conducted initially by Nikuradse (1933), and reinforced by Colebrook & White (1937) and Moody (1944), among others. The Reynolds number is the ratio of inertial forces to viscous forces: $Re = \rho U L_d/\mu$, where L_d is the characteristic length (e.g. diameter of a pipe) and μ is the dynamic viscosity of the fluid. The results show a correlation between wall roughness and energy loss: larger roughness causes greater friction losses, i.e. $f_d = f_d(Re, \varepsilon/D)$, (Munson et al., 2009).

In the Moody diagram (Figure 1.1) it can be seen that smaller roughness and high Re translate into a smaller friction factor. The friction factor f_d decreases as the surface becomes smoother. The lowest possible friction factor for solid surfaces is found in complete smooth surfaces ($\varepsilon/D \ll 10^{-6}$). However, nano- to micro-size features on materials of *low-surface* free energy can result in an even lower friction factor than a hydraulically smooth surface. Those surfaces are super-hydrophobic and their properties have been observed in nature for instance on the leaves of the

Lotus flower.

1.1 Super-hydrophobic surfaces

Super-hydrophobicity is the property of surfaces to repel water and is seen in nature, for example, on the leaves of the Lotus flower (Figure 1.2). Super-hydrophobic surfaces present characteristically high water contact angles of above 150° and very low rolling angles close to 1°. The contact angle (θ, equilibrium contact angle of the droplet on the solid) and rolling angle (θ_r) are used to quantify the wettability of a solid surface (Figure 1.3). The contact angle is defined as the angle of a droplet where the liquid-vapour interface meets the solid surface, and the rolling angle, or roll-off angle, is the angle of inclination of a surface at which a drop rolls off it, shown in Figure 1.3 (Nosonovsky & Bhushan, 2008a).

Hydrophobic surfaces present a water contact angle of $\geq 90°$, and surfaces with water contact angle below 90°are considered hydrophilic (Nosonovsky & Bhushan, 2008b). Due to the low adhesion of super-hydrophobic surfaces, water molecules of a droplet resting on a super-hydrophobic surface are pulled inwards. The gravitational force is negligible compared to the surface tension, resulting in a practically spherical shape (Zhou & Michael, 2017). These surfaces also present self-cleaning properties, shown in Figures 1.2 b and c, where dirt particles on a Lotus leaf are dissolved in water, consequently leaving the surface since the surface of the Lotus leaf has low water adhesion. This mechanism works as anti-biofouling on the Lotus leaf and protects the plant against attachment of microbes.

1.1.1 Contact angle in low-adhesion surfaces

The adhesion forces of a fluid on a solid surface depend on the chemical attraction between the two, and the result can be measured in the form of contact angle (CA,

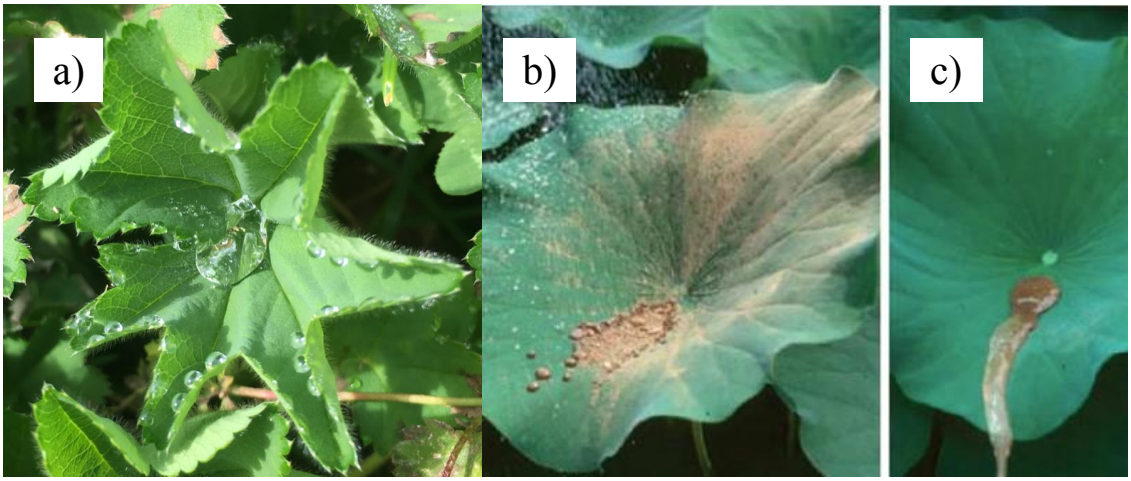

Figure 1.2: Examples of super-hydrophobicity found in nature. In a) is a super-hydrophobic leaf of a plant found in the Alpine region of Surselva (Picture taken by the author), and in b) and c) is the Lotus leaf, probably the most known example of super-hydrophobicity found in flora. In b) dirt particles sit on the surface of the lotus leaf, and in c) water leaves the surface with dirt particles, cleaning the leaf (Barthlott et al., 2017).

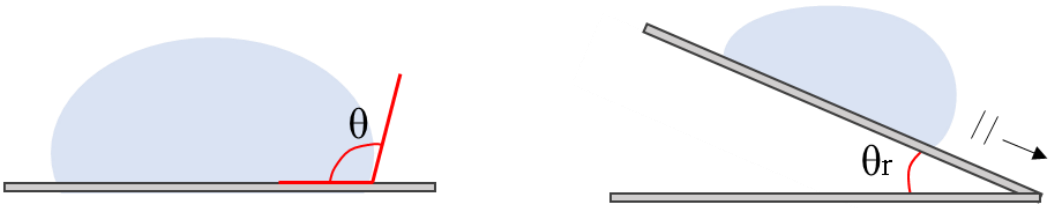

Figure 1.3: Contact angle (θ) of a droplet resting on a smooth surface and Rolling angle (θ_r) of a droplet on a inclined surface.

θ) of a droplet of the fluid resting on the surface of the solid, as shown in Figure 1.5. Young's equation of contact angle for smooth surfaces in equilibrium considers the solid-liquid and solid-vapour interfacial energies and the surface tension of the fluid, resulting in resting contact angle:

$$\gamma_{SG} - \gamma_{SL} = \gamma_{LG} \cos\theta \tag{1.2}$$

where γ_{SG}, γ_{SL}, γ_{LG} and θ are respectively the solid-vapour, solid-liquid interfacial energy, and the surface tension of the liquid, and the equilibrium contact angle of the droplet on the solid. The solid-vapour interfacial energy, or surface free energy or surface energy of a material is the excess energy per unit area due to the existence of the free surface (Krevelen & Nijenhuis, 2009). In liquids the equivalent free surface energy is called surface tension, and the solid-liquid interfacial energy is equal to the solid-liquid interfacial excess free energy per unit area (Krevelen & Nijenhuis, 2009, Binder et al., 2016). According to equation (1.2), if the free surface energy of a solid has a lower value than the solid-liquid interfacial energy, the left hand side becomes negative and consequently the contact angle is above 90°. Thus, studies have been conducted to estimate the lowest possible surface free energy of a solid (Zhou & Michael, 2017). While it is possible to obtain the value of surface tension of a fluid, theories diverge on the calculations of solid-liquid energy of contact, resulting in values differing by a factor of 1.5. To date, it is estimated that a smooth surface with the lowest possible surface free-energy yields a resting contact angle of circa 120° (Zhou & Michael, 2017). If the maximum possible resting contact angle for a smooth surface is approximately 120°, then how is it possible that natural materials such as Lotus leaves (*Nelumbo nucifera*, Figure 1.4) present contact angles of 160°?

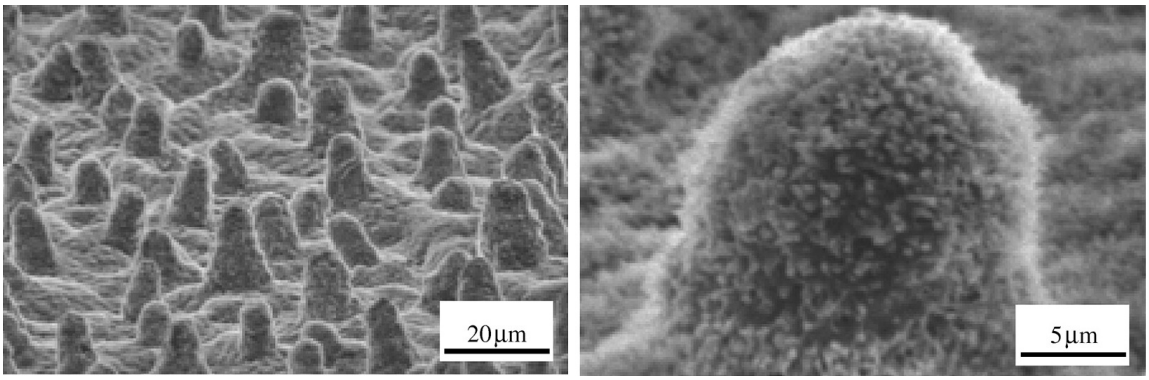

Figure 1.4: Scanning Electron Microscope (SEM) micrograph of the micro structure of a small section of the Lotus leaf (*Nelumbo nucifera*) (Nosonovsky & Bhushan, 2008b)

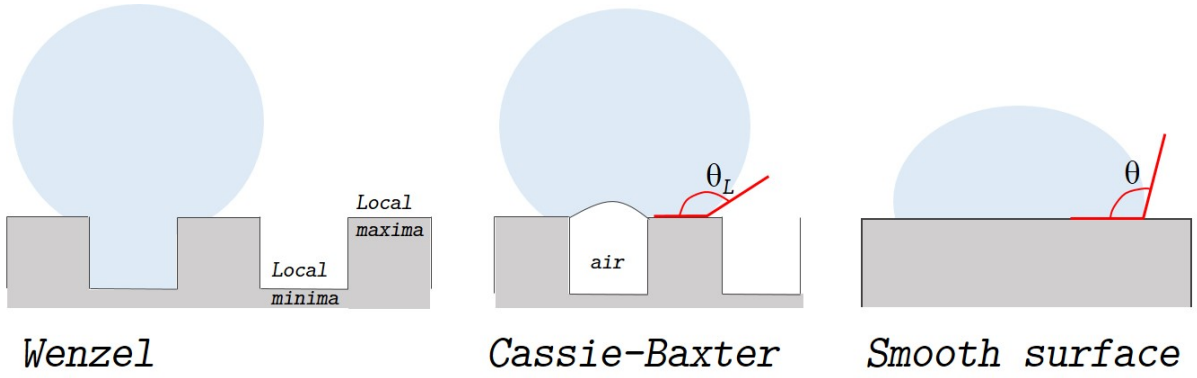

Figure 1.5: Illustration of wetting states in super-hydrophobic surfaces. In the Cassie-Baxter state air is trapped between the peaks - this usually causes drag reduction in water systems. In the Wenzel state, there are no air pockets on the rough surface, causing drag to increase. The symbol θ represents the contact angle between the droplet of water and the solid surface.

1.1.2 Surface roughness and the Cassie-Baxter state

Surfaces with ultra high water contact angles above 150° (super-hydrophobic surface) present a rough structure, that combined with a hydrophobic material exhibit super-hydrophobicity, and the Cassie-Baxter state of wetting. Figure 1.4 shows the rough structure of the Lotus leaf. The leaf is covered in a low-adhesion material that combined with the rough structure on the surface traps air pockets and reduces friction at the solid-liquid-air interface. The Cassie-Baxter state of wetting is the condition when a droplet resting on the solid surface is kept above the roughness elements, as seen in Figure 1.5 due to the air trapped on the rough hierarchical

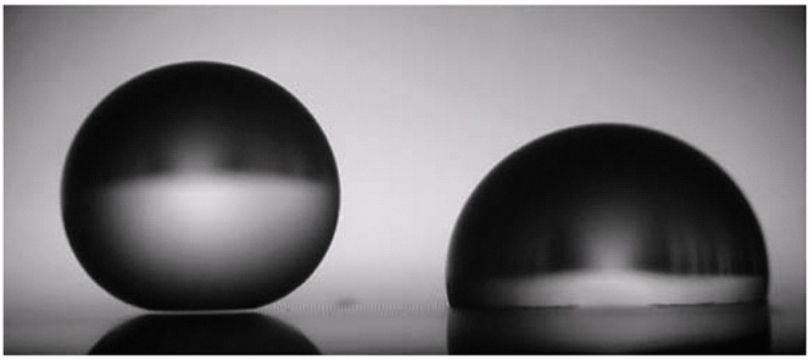

Figure 1.6: The Cassie-Baxter state of wetting on the left side and Wenzel state of wetting on the right side. In the Cassie-Baxter state the droplet is partially suspended by the air trapped on the solid surface. The Wenzel state on the right was induced and the liquid wets the surface. Reproduced with permission from Callies & Quere (2005).

structure[2]. Conversely, when there is no air trapped on the rough structure the wetting is said to be in the Wenzel state (Nosonovsky & Bhushan, 2008a). Figure 1.5 illustrates the two wetting states. A real example of the Cassie-Baxter and Wenzel states are shown in Figure 1.6. Light passes between the water-solid interface on the left side droplet, indicating the presence of the Cassie-Baxter state and contact angles much higher than 90°. On the right side droplet water is fully in contact with the solid.

However, in a fully submerged state, surfaces in the Cassie-Baxter state lose the air pockets due to diffusion of air in water. When in addition the fluid is flowing and in a turbulent state the air pockets can also be removed by hydrostatic and shearing forces (Du et al., 2017, Bobji et al., 2009). If the air pockets are completely removed the wetting state changes to Wenzel and the super-hydrophobic effects are lost. Consequently, the roughness on the surface causes friction to increase. The air pockets are key in decreasing friction in surfaces with the Cassie-Baxter state. Therefore, studies have attempted to produce a surface that can hold the air pockets for longer. However, it is inevitable that eventually they will vanish completely from the surface.

[2]Hierarchical structures contain textures on two or more length scales (Kota & Tuteja, 2014)

A micro- to nano-scale rough structure is crucial for a surface to exhibit the Cassie-Baxter state of wetting, and studies have been conducted to improve the relation surface-roughness and super-hydrophobicity, usually measured in the form of changes the apparent contact angle (θ_L). The size of roughness elements and distribution, that is, distance between pillars, geometry of roughness elements, hierarchical levels on the surface, among others, affect the apparent contact angle (Tao et al., 2016, Li et al., 2006, Zhang et al., 2016a). The surface roughness $R_f = \varepsilon/d_L$ is defined as a dimensionless relation of the area of a surface with fluctuations in height, characterised by asperities (ε, local maxima) and valleys (local minima), and the projected flat area (d_L) of a completely smooth surface (i.e. without asperities and valleys) (Nosonovsky & Bhushan, 2008a). A water droplet resting upon a rough surface of roughness R_f presents a contact angle θ, and resting upon a smooth surface it presents a contact angle θ_L, as shown in Young's equation (1.2) and in Figure 1.5. The relation between θ and θ_L for roughened surfaces is approximated by the Wenzel equation (Wenzel, 1936):

$$\cos\theta \approx R_f \cos\theta_L \tag{1.3}$$

The Wenzel equation is a simple method to estimate the influence of roughness in super-hydrophobic surfaces through changes in the contact angle. It is important to note that the changes in contact angle can only be measured on non-submerged surfaces. The contact angle cannot be measured whilst fluid flows on a super-hydrophobic surface, as the contact angle is the measurement of the angle of a droplet of a fluid on a super-hydrophobic surface. It should be noted that the contact angle is only one of the variables used to compare surfaces with various hydrophobicity in fluid flow studies. Moreover, surfaces of various roughening geometries (e.g. spikes, ridges, pillars, etc.), may present similar relative R_f, but different contact angles (Tao et al., 2016, Li et al., 2006, Zhang et al., 2016a).

Several studies have been conducted on roughening surfaces to improve hydrophobicity. The surface structure can be random - generally in super-hydrophobic paints where nano-particles are deposited on a surface; or engineered to have an optimal

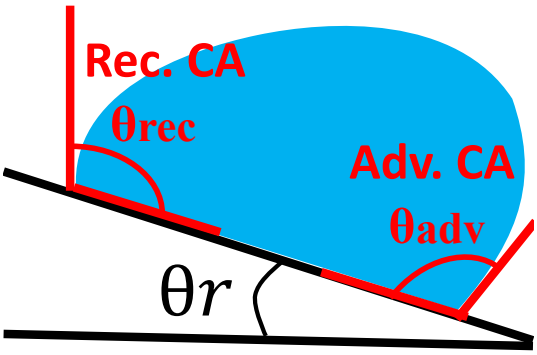

Figure 1.7: Droplet of water sliding on solid surface of rolling angle θ_r. The droplet shape shows the advancing contact angle θ_{adv} and receding contact angle θ_{rec} (Teisala & Butt, 2019).

structure. For instance, Ybert et al. (2007) simulated the ratio of the solid surface in relation to the gas fraction between the pillars on the roughened surface. The authors found an optimum relation of pillars of diameter 50 to 100 nm, 5 μm apart, resulting in a contact angle of 179°. Lu et al. (2016a) engineered a range of surfaces of pillars, ridges and grids to improve hydrophobicity, using electron beam lithography on polymers. Several methods exist to manufacture super-hydrophobic surfaces, with variations of methods to roughen the surface, and several types of surface modifying agents (SMA) used to change the surface chemistry, changing the surface from hydrophilic to hydrophobic. Some are shown in Table 1.1, where the super-hydrophobicity is generally quantified in terms of apparent water contact angle θ_L, but also as advancing (Adv. CA) and receding (Rec. CA) water contact angles, shown in Figure 1.7.

Table 1.1 shows that the majority of the studies listed created a random surface roughness by deposition of nano-particles to form the asperities on the surface of the substrate, especially silica nano-particles. Randomly arranged surfaces also presented higher water contact angles than surfaces where the surface roughness was engineered - engineered surfaces are presented in the work of Knaust et al. (2016)[3] (Adv. CA

[3]high advancing and receding contact angles (CA > 150°) are also an indication of super-hydrophobicity.

up to 136°and Rec. CA up to 114°), Lu et al. (2016b) showing a maximum CA of 140°, and Guan et al. (2015) showing a maximum contact angle of 149°. In contrast, surfaces with randomly arranged micro-nano sized particles deposited on the surface or chemically etched to form nanoscale roughness presented water contact angles as high as 175°.

Surfaces that were formed by roughening materials of low surface energy[4] did not have to be modified by applying a SMA, and surfaces that were formed by roughening a hydrophilic substrate or hydrophilic nano-particles (e.g. titanium dioxide (TiO_2) or silica dioxide (SiO_2)) were modified with hydrophobic coatings such as hexamethyldisilazane (HMDS) or fluorinated compounds such as trichloro(1H,1H,2H,2H-perfluorooctyl)silane (PFTS). The hydrophobic coatings were used as the SMAs to change the affinity of the nanoparticles with water - TiO_2 and SiO_2 are hydrophilic. By reacting or coating a hydrophilic substrate with HMDS or PFTS, a hydrophobic tail is added to the substrate, changing their chemical affinity with water. Figure 1.8 illustrates the reaction of a hydrophilic silica substrate with HMDS (Crick & Parkin, 2011)).

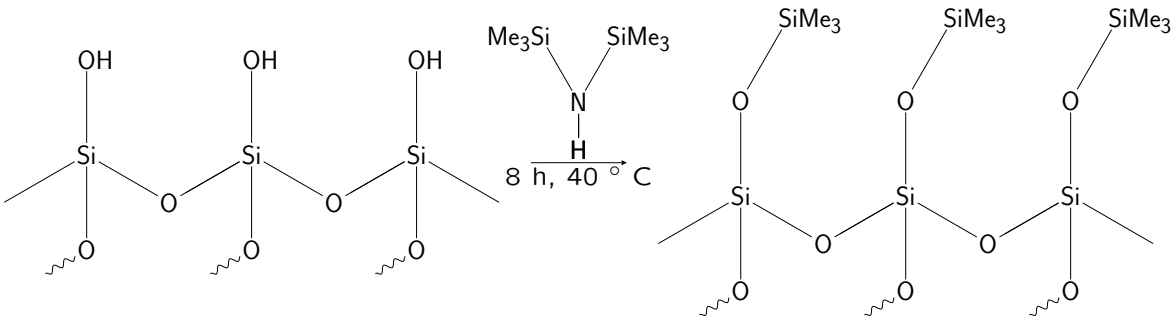

Figure 1.8: Illustration of reaction of hydrophilic porous silica glass into hydrophobic. Extracted from Crick & Parkin (2011). The radical Me_3 is $(CH_3)_3$.

[4]Surface free energy or surface energy is equal to the energy needed to create a surface with the unit area (Nosonovsky & Bhushan, 2008a). The surface energy influences significantly the wettability of solids by liquids and optimisation of coating processes.

Moreover Table 1.1 compares the resulting contact angle from surface modified with the same SMA but with different methods to create surface roughness. For instance Maharjan et al. (2020) and Zhang et al. (2016b) modified their samples with PFTS. However, Maharjan et al. (2020) created a hierarchical rough surface by etching a glass substrate with two abrasive materials resulting in a contact angle of 104°, and Zhang et al. (2016b) created roughness on a glass substrate by random deposition of silica nano-particles resulting in a considerably higher contact angle of 157°.

Table 1.1: Materials used to roughen smooth substrates and modify hydrophilic surfaces, and their resulting contact angle.

Author	**Roughness**	**SMA[i]**	**Max CA[ii]**	**Adv. CA[iii]**	**Rec. CA[iv]**
Knaust et al. (2016)	90 μm Trenches made from chemical etching and UV lithography	DMDCS[v]		97	89
		PFTS[vi]		136	114
Zhao et al. (2012)	Surface replica of shark skin on PDMS[vii]		103		
Crick & Parkin (2010)	Random, film grown by aerosol assisted CVD[xiii] of Dyneon FC-2120		104		
Maharjan et al. (2020)	Mechanical etching, then random deposition of SMA[i]	PFTS[vi]	104		
Yan et al. (2014)	Randomly arranged MgF_2sol-gel deposited on glass	Methyl silicone	115		
Dou et al. (2016)	Randomly arranged silica nano-particles by sol-gel	POTS[xiv]	131		
Lu et al. (2016b)	Electro beam lithography on PDMS[vii]		140		
Guan et al. (2015)	Surface replica of Water Bamboo Leaves on PDMS[vii]		149		

Author	Roughness	SMA	Max CA	Adv. CA	Rec. CA
Yuyang et al. (2008)	Randomly arranged chitosan particles	polysiloxane emulsion	150		
Pan et al. (2008)	Etched Cu mesh	n-dodecanethiol	151		
Li et al. (2006)	Randomly arranged silica nano-particles	PVDF[viii]	153		
Spathi et al. (2015)	Randomly arranged Paper Sludge Ash particles	Stearic acid	153		
Yin et al. (2020)	Randomly arranged $Cu(OH)_2$ on steel mesh	n-dodecanethiol	154		
Tao et al. (2016)	Randomly arranged silica nano-particles	HMDS[ix]	156		
Zhang et al. (2016b)	Randomly arranged silica nano-particles	PFTS[vi]	157		
Ohkubo et al. (2010)	Sandblast followed by Electrolytic etching	HDFS[x]	159		
Bahng et al. (2015)	Randomly arranged ZnO nano-particles	OTMS[xi]	160		
Crick & Parkin (2010)	Random, CVD[xiii] with SYLGARD 184		160		
Xu et al. (2020)	PMMA-b-PTFMA-1[xii] onto cotton fabric		160		
Crick & Parkin (2010)	Random, film grown by CVD[xiii] of NuSil Med-4850		162		
Crick & Parkin (2009)	Random, film grown by CVD[xiii] of SYLGARD 184		167		

Author	**Roughness**	**SMA**	**Max CA**	**Adv. CA**	**Rec. CA**
Lu et al. (2015)	Randomly arranged TiO_2 nano-particles	POTS[xiv]	168		
La et al. (2011)	Etched Cu mesh	POTS[xiv]	170		
Lin et al. (2020)	Randomly arranged silica nano-particles	polyvinylidene fluoride	172		
Crick & Parkin (2011)	Film grown by aerosol assisted CVD[xiii] of silica microparticles	HMDS[ix]	175		

[i] Surface modifying agent

[ii] Maximum contact angle

[iii] Advancing contact angle

[iv] Receding contact angle

[v] DMDCS: dimethyldichlorosilane

[vi] PFTS: trichloro(1H,1H,2H,2H-perfluorooctyl)silane

[vii] PDMS: Polydimethylsiloxane

[viii] PVDF: polyvinylidene fluoride

[ix] HMDS: hexamethyldisilazane

[x] HDFS: Heptadecafluoro-1,1,2,2-tetrahydrodecyltrimethoxysilane

[xi] OTMS: (7-octen-1-yl) trimethoxysilane

[xii] PMMA-b-PTFMA-1: poly(methyl methacrylate)-b-(trifluoroethyl methacrylate)

[xiii] CVD: Chemical Vapour Deposition

[xiv] POTS: 1H,1H,2H,2H-perfluorooctyltriethoxysilane

1.2 Super-hydrophobic surfaces in water transport systems

The use of super-hydrophobic surfaces in drag reducing applications has been recently studied and shown friction reductions as high as 50% (Daniello et al., 2009). Super-hydrophobic surfaces reduce friction as the fluid has less contact with the actual surface due to the presence of the air pockets in between the low-adhesion surface structures. As the air acts as a lubricant, the fluid experiences less friction on the liquid-solid interface. In this section an introduction of flows on no-slip surfaces is presented, then the effects of partial slip and its effect on water flow is introduced in a table summarising previous studies of turbulent water flow carried out on super-hydrophobic surfaces with the Cassie-Baxter state.

1.2.1 Head loss, shear stress and energy consumption modelling

Water contained in a reservoir upstream has a potential energy that is converted into kinetic energy as water flows downstream. In a steady flow the sum of all types of energy at all points is constant along a streamline, that is, the energy is conserved along a streamline. For steady flows of a fluid of constant density, the principle of energy conservation is captured with the Bernoulli equation, which stipulates that the total energy E along a streamline is conserved. Here,

$$E = p + \rho g z + \frac{1}{2}\rho U^2 \tag{1.4}$$

where p is the pressure, g is earths' gravitational acceleration, and z is the elevation of the point above a reference plane. The terms $\rho g z$ and $\frac{1}{2}\rho U^2$ correspond respectively to the gravitational potential energy and kinetic energy. The units of the terms in equation (1.4) are given in J/m^3. Dividing equation (1.4) by ρg, the Bernoulli

equation can be expressed in terms of heads (m):

$$H = \frac{p}{\rho g} + z + \frac{U^2}{2g} \tag{1.5}$$

where H is the total energy head and $\frac{U^2}{2g}$ is the velocity head. In many situations, we are more interested in knowing the representative energy head for an entire cross section rather than for a single streamline. In this case, E takes exactly the same form, but U represent the cross-sectionally averaged velocity and a correction factor α emerges in front of the velocity head for the $\frac{U^2}{2g}$. For turbulent flows, this correction velocity is usually close to unity, and $\alpha = 1.0$ will be used in this study [5]). The term $\frac{p}{\rho g} + z$ is usually referred to as the piezometric head h, and equation (1.5) becomes simply:

$$H = h + \frac{U^2}{2g} \tag{1.6}$$

Figure 1.9 illustrates the terms in equation (1.6). The initial head is represented by H_0 and as water flows along the pipe of diameter 2δ, the total energy head H can be represented by the Energy Grade Line (EGL) and the piezometric head h by the Hydraulic Grade Line (HGL). In a frictionless system, the EGL would be a straight line parallel to the level of the reservoir, and $H_1 = H_0$ (total energy is conserved). However, a liquid flowing on a surface of certain roughness loses energy due to friction losses. In Figure 1.9 the EGL begins on the level of the liquid on a surface and has a negative slope due to friction. The HGL represents the height to which water rises in an open vertical tube when a flow passes through the closed system (Jones, 2011b), and the difference between the EGL and the HGL is the velocity head. The head loss (ΔH) is the difference between the energy head H_1 and H_2. If U^2 and δ inside the pipe are constant, then the slope in the EGL is equivalent to the slope in the HGL ($\Delta H \approx \Delta h{=}h_1 - h_2$).

Head losses are usually categorised in major and minor losses. Major losses are due

[5] Values of α are 2 for laminar and 1.05 for turbulent flows (Jones, 2011b)

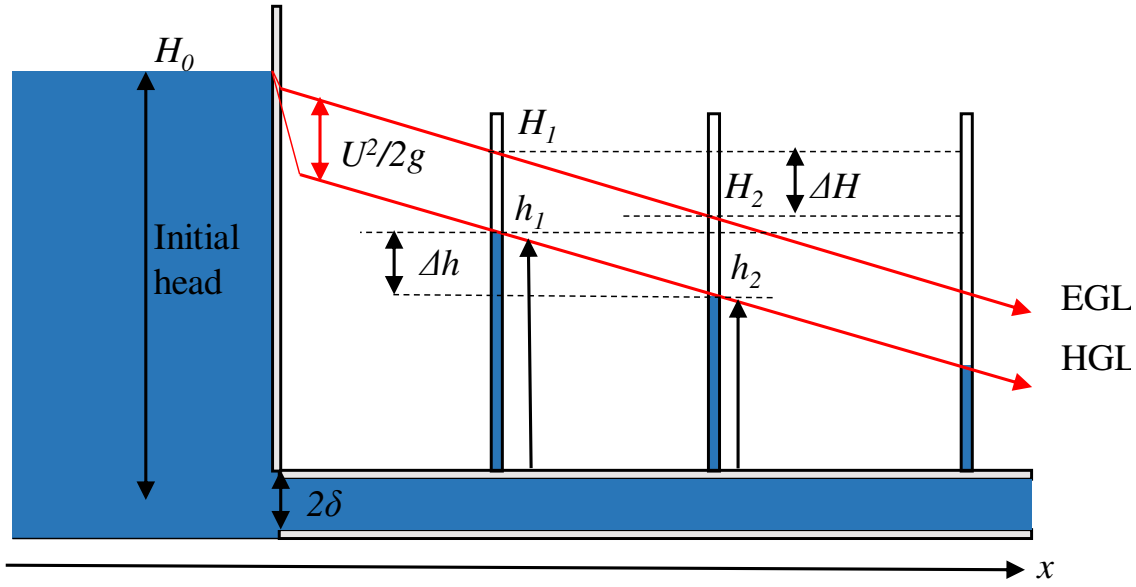

Figure 1.9: Head loss and hydraulic grade line (HGL) on a channel or pipe. EGL is the Energy Grade Line. If U^2 and δ inside the pipe are constant, then the slope in the EGL is equivalent to the slope in the HGL.

to friction, and are given by:

$$\Delta H = \overline{f}_d \frac{U^2}{2g} \frac{L}{D} \tag{1.7}$$

where $\overline{f}_d$ is the average (Darcy-Weisbach) friction factor. For non-circular pipes, D is replaced by the hydraulic diameter $D_h = 4\ A/P$, where A is the area and P is the perimeter of the cross section. A momentum balance over a pipe segment of length L and constant cross-section results in a balance between the pressure difference Δp across the segment and the wall shear stress τ_w:

$$\Delta p A = \tau_w P L \tag{1.8}$$

Substituting $\Delta p = \rho g \Delta H$ into equation (1.8), then equation (1.8) into equation (1.7), the wall shear stress τ_w can be expressed as:

$$\tau_w = \frac{1}{8} \overline{f}_d \rho U^2 \tag{1.9}$$

Friction losses affect directly the power needed to move water through a pipe. In terms of head, the power demand P_w can be calculated as the following:

$$P_w = Q \rho g \Delta H \tag{1.10}$$

where $Q = UA$ is the volume flux. Substituting equation (1.7) into equation (1.10) results in equation (1.1) ($P_w = a \rho \overline{f}_d U^3$).

As mentioned previously, the velocity U and cross-sectional area A are chosen on other grounds in water distribution networks, which implies that the main parameter to reduce energy consumption P_w is to decrease f_d. This can be achieved by using hydraulically smooth surfaces instead of rough surfaces (Moody, 1944). The relative size of the roughness element ε in relation to the viscous length scale ν/u_* where ν is the kinematic viscosity and $u_* = \sqrt{\tau_w/\rho}$ is the friction velocity, is commonly expressed in terms of the roughness Reynolds number $Re_s = \varepsilon u_*/\nu$. For values of $Re_s < 5$ (i.e. the roughness elements are inside the viscous sublayer), the wall is

considered hydraulically smooth, and for $Re_s > 70$ the wall is hydraulically rough (Nakayama, 2018, Masad, 1995).

The surface roughness affects the friction factor f_d as shown before in the Moody diagram (Figure 1.1). There are several ways to estimate the friction factor of a surface. For instance, if equation (1.7) is rearranged, the friction factor can be obtained using the piezometric head difference between two points:

$$\overline{f}_d = \Delta h \frac{D_h}{L} \frac{2g}{U^2} \tag{1.11}$$

1.2.2 Slip length

The shear stress for a hydraulically smooth surface is proportional to the velocity gradient du/dr at the wall:

$$\tau_w = \mu \left. \frac{du}{dr} \right|_w \tag{1.12}$$

where r is a coordinate perpendicular to the wall. The velocity gradient profile differs for laminar and turbulent flows, but in both regimes the velocity of the fluid near the wall u_w is approximately zero and the velocity is at its maximum in the centre of the conduit. At the surface, the flow is 'stopped' by the adhesion and frictional forces near the solid boundary. This effect is known as the **no-slip condition**, and holds for most engineering applications

$$u_w = 0 \tag{1.13}$$

On the other side of the spectrum, the free-slip condition represents surfaces that are frictionless. These surfaces are mathematically represented by

$$\left. \frac{\partial u}{\partial z} \right|_w = 0 \tag{1.14}$$

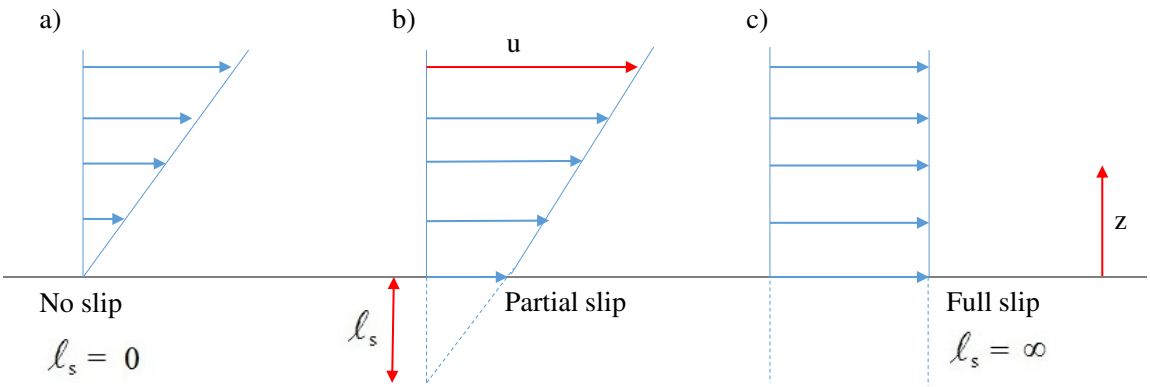

Figure 1.10: Illustrative explanation of slip velocity and slip length (ℓ_s)

These surfaces do not exist in reality, but provide a useful idealised case for studies in which friction is unimportant.

Super-hydrophobic surfaces can be modelled with *partial-slip* boundaries due to the air pockets trapped between the solid surface (Voronov et al., 2007, Priezjev et al., 2005, Rahman et al., 2013a, Tretheway & Meinhart, 2002). Partial-slip boundaries can be represented by a slip velocity (u_w) and slip length (ℓ_s). The slip length is the extrapolated distance to the wall that meets the tangential line extrapolated from the velocity, when the velocity at the wall is $\neq 0$ (Figure 1.10).

Figure 1.10 presents three cases: a) is the no slip condition, where $u_w = 0$ and $\ell_s = 0$; b) shows the partial slip, where $u_w > 0$ and $0 < \ell_s < \infty$; and c) where $u_w > 0$ and $\ell_s = \infty$.

The relationship between slip velocity (*i.e.* velocity at the wall) and slip length was proposed by Navier (1823) as:

$$u_w = \ell_s \frac{du}{dz}\bigg|_w \tag{1.15}$$

Typical values of ℓ_s are in the nano- to micrometer scale, varying accordingly to the viscosity, velocity and direction of the fluid, surface dimension and surface pattern,

among others. For turbulent flows, slip lengths of 70 to 120 μm have been found experimentally at Re $\geq$ 4,000 (Daniello et al., 2009).

1.2.3 Advantages of using super-hydrophobic surfaces in water flow

The use of super-hydrophobic surfaces in turbulent flows has been investigated numerically and experimentally, showing drag reduction and apparent slip on the surface due to the shear-free areas where the air is present (Costantini et al., 2018, Daniello et al., 2009, Yao et al., 2015, Min & Kim, 2004). Air is approximately 50 times less viscous than water, implying the shear stress will also be smaller by that factor and can be considered shear-free (Ybert et al., 2007, Davis & Lauga, 2009). In super-hydrophobic surfaces the high shear stress surface area is reduced and replaced by shear-free areas (air pockets), thus reducing the overall friction.

Experimental studies measured drag reduction in pipes and channels with super-hydrophobic walls by measuring pressure drop and velocity of the fluid. Table 1.2 presents an overview of studies that quantified friction reduction of super-hydrophobic surfaces under turbulent conditions on super-hydrophobic channels, discs, spheres and others. Most studies quantified drag reduction as a means of demonstrating the positive effects of super-hydrophobic surfaces in turbulent flow. Daniello et al. (2009) obtained up to 50% drag reduction in a experiment of water flowing under turbulent conditions over engineered super-hydrophobic surfaces. The pressure drop was obtained using the height difference of water in piezometric tubes, and the velocity of water close to the wall was obtained using particle image velocimetry. Yao et al. (2015) obtained 12% drag reduction in a water tunnel experiment, which was calculated using pressure drop measurements from pressure sensors. Walker et al. (2016) measured the time, and consequently velocity, of 10-30 L and water flowing in a super-hydrophobic pipe of 0.015 m diameter, reporting a friction factor reduction of 33%. Additional examples are presented in section 1.2.3.

Drag reduction varies strongly with the type of super-hydrophobic surface and the value of Re. For instance, Moaven et al. (2013) performed experiments at $Re = 10^6$ using a rheometer with a super-hydrophobic surface disc of 160° water contact angle, resulting in a reduction of drag of 15% when compared with a smooth disc. However, Paik et al. (2015) performed experiments at similar $Re = 9 \times 10^6$ of a sphere coated with a super-hydrophobic material of 156° water contact angle, but obtained a lower drag reduction of 3-5%.

Table 1.2: Summary of experiments that determined drag reduction of flow on super-hydrophobic surfaces

Author	**Details**	**Re**	ℓ_s (μm)	**CA**[xv]	**Adv. CA**[xvi]	**RA**[xvii]	τ_w **(kPa)**	**DR**[xviii]	u_s/u
Min & Kim (2004)	Channel		2×10^2					0%	0.035
			5×10^2					1%	0.088
			1×10^3					2%	0.176
			2×10^3					5%	0.349
			5×10^3					10%	0.845
			1×10^4					18%	1.618
			2×10^4					29%	3.006
Daniello et al. (2009)	Channel	4×10^3	120		125			20-60%	
		8×10^3							
		4×10^3			110			50%	
		8×10^3							
		4×10^3	70		125		0.75	22%	
					110		1	20%	
Nouri et al. (2012)	Channel	180[xix]	2					1%	
		180[xix]	1					1%	
		395[xix]	2					4%	
		395[xix]	1					9%	
		500[xix]	2					10%	

Author	**Details**	**Re**	ℓ_s (μm)	**CA**	**Adv. CA**	**RA**	τ_w **(kPa)**	**DR**	u_s/u
		500[xix]	1					27%	
Moaven et al. (2013)	Disc	10^5-10^6		160				15%	
Rahman et al. (2013a)	Pipe		up to 23.9						
Brassard et al. (2015)	Sphere	3×10^4		156		4		16%	
Paik et al. (2015)	Water tunnel	9×10^6		85.5				3-5%	
Tian et al. (2015)	Channel			161		0.9		10%	
Yao et al. (2015)	Water tunnel	1×10^6		105					
Fuaad et al. (2016)	Channel	180[xix]							
	Posts							22%	
	Ridges							10-19%	
Walker et al. (2016)	Pipe		65					20-30%	

[xv] Contact angle

[xvi] Advancing contact angle

[xvii] Rolling angle

[xviii] Drag reduction

[xix] Re_τ: Shear Reynolds number, $Re_\tau = u_*\delta/\nu$, u_* is the friction velocity

1.3 Maintaining the Cassie-Baxter state in immersed conditions

The transport of drinking water in pipes occurs under turbulent conditions, and the walls of the pipe are constantly in contact with water. If one were to use a super-hydrophobic material to reduce friction inside the pipe, the super-hydrophobic surface would be subjected to water pressure and turbulence which disrupts the air pockets trapped on the surface (Fukuda et al., 2000, Murai et al., 2007, Park et al., 2015, Zhang et al., 2018). Since the air pockets are key to decrease friction in super-hydrophobic surfaces, this will result in a rapid decrease of the drag reduction with time due to the loss of trapped air, causing the wetting state to transition from Cassie-Baxter to the Wenzel state (Bobji et al., 2009, Lee & Kim, 2011, Boreyko & Chen, 2009). Loss of super-hydrophobicity may also be caused by abrasion of the surface or loss of trapped air by diffusion into the water (Mohamed et al., 2015, Bobji et al., 2009). The loss of trapped air at super-hydrophobic surfaces with different textures occurs at different rates.

Although studies show that surfaces in the Cassie-Baxter state reduce drag, these surfaces may ***increase*** drag if the air pockets are removed and the wetting state changes to Wenzel (Du et al., 2017, Wenzel, 1936). A surface in the Wenzel state presents high surface roughness, and without air the rough solid-liquid interface becomes a barrier for the fluid, that according to the Moody diagram (Figure 1.1) results in higher wall friction.

Entrapped gas was observed on various rough surfaces that were immersed in water under static conditions (Bobji et al., 2009, Wang et al., 2014), and the durations of air retention were compared, showing a high dependence on surface structure. The mean time for the trapped air to disappear ranged from approximately 35 minutes for surfaces with pillars and 25 minutes for surfaces with ridges (Bobji et al., 2009), to 1 hour for micro-grooved surfaces (Wang et al., 2014). Super-hydrophobic surfaces

with ridges have been shown to retain air pockets for more than 8 hours under very small static water pressure of 50 mm ($\sim$ 490 Pa), where the main factor to maintain the Cassie-Baxter state was the minimized environmental fluctuations such as no variation in temperature (Xu et al., 2014). Moreover, dissolved air and traces of surfactant may also increase the rate of removal of the air layer in super-hydrophobic surfaces (Mohammadi et al., 2004, Shirtcliffe et al., 2009).

Efforts have been made to overcome loss of super-hydrophobicity by manufacturing a durable super-hydrophobic material. Jenner et al. (2013) investigated the durability of super-hydrophobic coatings using combinations of layers of adhesion promoters and low surface-energy materials such as Hyflon. The adhesion promoters ensured the attachment of the top coating to the substrate and Hyflon, a fluoropolymer, increased the hydrophobicity of the surface. The authors found that samples coated with a combination of HMDS and Hyflon maintained rolling angles below 20° for at least 600 hours when immersed in water. Lee & Kim (2011) studied the restoration of gases on super-hydrophobic surfaces immersed in static water pressure by regenerating gas from electrolysis. Electrodes were placed on the bottom of the surface that were only activated when the surface became wet from losing entrapped gas, consuming 6 mW of power for 150 seconds on an area of 4 cm^2.

Bubble injection can be used as a means to recover the Cassie-Baxter state of a super-hydrophobic surface. A combination of techniques using super-hydrophobic materials and air injection has been previously proposed to decrease drag in boats with more durable air-solid-water interfaces (Fukuda et al., 2000). A maximum reduction of 80% in frictional resistance was achieved at a speed of 4 m/s and 55% at 8 m/s. High drag reduction by repetitive streamwise air bubble injection has been previously investigated in turbulent flow channels and ship hulls, showing reductions in drag of up to 60% (Murai et al., 2007, Park et al., 2015, Zhang et al., 2018).

Park et al. (2015) experimented with drag reduction by applying repetitive air bubble injection in a turbulent channel flow. In the experiment, air bubbles of various sizes

were applied near the upper smooth wall of the channel and caused drag to decrease by up to 30%. Murai et al. (2007) also applied micro-bubbles of air near the wall in a turbulent rectangular channel flow, and obtained a maximum drag reduction of 55% in their optimal experimental condition. Although these results are promising, further analysis is needed to assess the energy efficiency when applying an air flow continuously. In the research cited, the air bubbles are lost when injected. It would be ideal if the bubbles remained on the surface in order to continuously reduce drag.

A similar technique of repetitive bubble injection has been previously used in an experiment that aimed to maintain the air pockets on a super-hydrophobic surface under turbulent conditions, and obtained a maximum drag reduction of 20% in the Cassie-Baxter state (Du et al., 2017). In the experiment performed by Du et al. (2017) air was injected through a 0.6 mm hole and the air pockets were retained on the surface up to only 10 seconds. By repeatedly injecting air bubbles due to the short retention of the air pockets, the Cassie-Baxter state near the injection hole was recovered and consequently the feasibility of use of super-hydrophobic materials improved. The approach that will be taken in this dissertation is to inject bubbles in the flow by blowing air through a porous super-hydrophobic surface, thereby ensuring a reasonably homogeneous replenishment of the air pockets.

1.4 Reactions with the super-hydrophobic surface

One of the methods to disinfect drinking water is to add an oxidising agent such as free chlorine. The addition of sodium hypochlorite (NaClO) forming up to 0.5 mg/L of free chlorine species (HOCl and $^{-}$OCl) in water ensures the water is safe to drink by inactivating pathogens. The material developed in this research is new, therefore not yet listed in the list of approved materials for use in public water in the United Kingdom as stated in Regulation 31 of the Drinking Water Inspectorate (DWI) (Drinking Water Inspectorate, 2016). New products used in drinking water pipes need to be approved by DWI. According to DWI Regulation 31, the approval

of a product:

> "Approval is based upon consideration as to whether the use of a substance or product will adversely affect the quality of the water supplied, or cause a risk to the health of consumers; no consideration is given to fitness for purpose and approval by the Authorities must not be taken as a favourable assessment of the performance or merits of any substance or product. It is the responsibility of the end user to ensure fitness for purpose."

To ensure that the material developed in this research does not react with the free chlorine in drinking water pipes and will not affect the quality of the drinking water, the effects of water containing an oxidising must be investigated upon contact with the novel material.

1.5 Aims and Objectives

This research aims to develop a durable super-hydrophobic material capable of reducing the friction in water pipes. The durability of the surface will be analysed by the ability of the surface to maintain the Cassie-Baxter state underwater. Previous research has demonstrated that surfaces with the Cassie-Baxter state of wetting cause drag reduction in devices that are in contact with water, and inevitably lose the drag-reducing effect over time. In light of the potential of using these surfaces to decrease the energy demand in transporting water, and the weaknesses of this effect, the objectives of this research are to:

1 manufacture a robust super-hydrophobic material able to maintain/recover a Cassie-Baxter state underwater;

2 evaluate the viability of the new material for use in drinking water applications by studying the formation of toxic compounds upon contact with water

disinfectant agent NaOCl;

3 determine experimentally the friction reduction for the new super-hydrophobic material;

4 investigate the durability of the drag reduction for the new super-hydrophobic material.

1.6 Structure of this thesis

This report is structured as follows. The current chapter introduces the definition of super-hydrophobic surfaces and the effects in turbulent water flow when transporting water in super-hydrophobic ducts. Moreover, Chapter 1 presents the challenges of maintaining the super-hydrophobic effects over time and presents the four objectives identified to overcome the low durability of super-hydrophobic surfaces. Chapters 2, 3 and 4 describe the manufacturing of a robust super-hydrophobic material able to maintain/recover a Cassie-Baxter state underwater (Objective 1). Chapter 2 presents initial research on the durability of super-hydrophobic coatings. Chapter 3 presents the changes in water contact angle of surfaces manufactured with various particle sizes of soda-lime glass and three different surface-modifying agents. Soda-lime glass is hydrophilic and was modified by adding a hydrophobic tail to the Si-O bonds. The hydrophobicity of samples was quantified by measurements of the water contact angle. Chapter 4 presents the results of recovery of the Cassie-Baxter state for three samples tested under static water pressure and evaluates the viability of the new material as a drinking water pipe, fulfilling Objective 2 (to evaluate the viability of the new material for use in drinking water applications by studying the formation of toxic compounds upon contact with water disinfectant agent NaOCl). Super-hydrophobic surfaces lose their hydrophobicity by loss of the trapped air pockets. By applying an air pressure across the material, the recovery of the Cassie-Baxter state was assessed. These samples were selected based on the results presented in Chapter 3. Chapter

5 presents the design of an experimental setup for quantifying drag in a duct with a super-hydrophobic top surface under turbulent flow conditions, fulfilling Objective 3 (to determine experimentally the friction reduction for the new super-hydrophobic material). Finally, Chapter 6 investigates the durability of the drag reduction for the new super-hydrophobic material (Objective 4). Furthermore, Chapter 6 presents the experimental results for drag and durability for the experiment as outlined in Chapter 5. Concluding remarks and recommendations for future work will be made in Chapter 7.

2

Preliminary study on durability of super-hydrophobic coatings

2.1 Introduction

Super-hydrophobic coatings in the Cassie-Baxter state of wetting have been demonstrated to decrease drag in water transporting applications by reducing the area of contact between the solid surface and water, substituting partially the solid surface by air pockets. However, previous studies have demonstrated that the super-hydrophobic effects do not last indefinitely and super-hydrophobic coatings have to be reapplied to the surface of interest. As discussed in chapter 1, loss of super-hydrophobicity occur due to: a) loss of trapped air pockets that change the wetting state of the surface from Cassie-Baxter to Wenzel (Du et al., 2017); b) loss of surface structure (loss of nanoparticles on the surface) (Jenner et al., 2013); and c) change of surface chemistry (Boinovich et al., 2010).

This Chapter presents a study of the durability of three super-hydrophobic coatings

by assessing the loss of the super-hydrophobic effects upon immersion in water for long periods of time. The results presented in the following sections will show that super-hydrophobic coatings are not robust for engineering applications where the material is constantly subjected to water pressure, and thus that a material that is intrinsically water repellent is needed. The experiments presented in this chapter consist of measuring over time the contact angle (θ_L) and rolling angle (θ_r) of of a droplet of water resting on acrylic surfaces coated with super-hydrophobic materials that were immersed in water for extended durations.

2.2 Materials

Pieces of acrylic (substrates) of size 7 cm × 3 cm × 0.5 cm were coated each with a super-hydrophobic material. Three super-hydrophobic materials were used: a) hydrophobic Paper Sludge Ash (HPSA); b) a TiO_2 based super-hydrophobic paint diluted in ethanol provided by a researcher of super-hydrophobic coatings, prepared as published in Lu et al. (2015); and c) NeverWet® (NeverWet LLC, Lancaster, United States), a commercially available super-hydrophobic spray coat. Coatings a) and b) were attached to the acrylic piece with double sided tape, and c) with a base coat provided by the manufacturer. A more detailed composition of each super-hydrophobic coating is presented below.

2.2.1 Hydrophobic Paper Sludge Ash

Paper Sludge Ash is a waste material generated from paper recycling. The ash contains calcium minerals. When dry milled with stearic acid, the hydrophobic tail of stearic acid bonds with calcium and forms calcium stearate, a water repellent material, forming a hydrophobic paper sludge ash (Spathi et al., 2015). The micro-particles from HPSA create a random rough structure on the surface which is rich in air, as described previously as a property of super-hydrophobic materials. HPSA has

been added to concrete in previous studies in order to produce a super-hydrophobic material for civil engineering applications (Wong et al., 2015).

2.2.2 TiO_2 paint

TiO_2 paint was provided by a former Imperial College researcher from the Department of Chemistry. The formulation of the paint has been published by the authors in a scientific journal (Lu et al., 2015). It was prepared with a range of TiO_2 nanoparticles (60 to 200 nm) dissolved in ethanol. A hydrophobic chemical, 1h,1h,2h,2h-perfluorooctyltriethoxysilane (POTS) was used to coat the titanium dioxide particles. The paint contained nano-particles to create a random rough surface and a hydrophobic surface, forming a super-hydrophobic paint (Lu et al., 2015).

2.2.3 NeverWet®

NeverWet® is a two-spray coat made of a base coat and a top coat. The base coat product aims to attach the materials contained in the top coat spray. The top coat has nano-particles attached to a hydrophobic chemical. The exact composition is unknown because this is a commercial product. However, the presence of nano-particles can be confirmed using SEM, shown in Figure 2.1 and the general composition indicates the hydrophobic chemical coating the nano-particles is a organosilane. The scale bar on Figure 2.1 represents 1 μm and the particles agglomerated on the surface are considerably smaller than the scale bar in the range of nano-meters. The material has been patented and is described as follows (Sikka et al., 2016):

> "A composition for coating surfaces and objects giving rise to a hydrophobic coating comprising: an acrylic binder, nano-particles from about 8 nm to about 100 nm associated covalently or non-covalently with alkyl or fluoroalkyl groups, and a solvent,[...] "

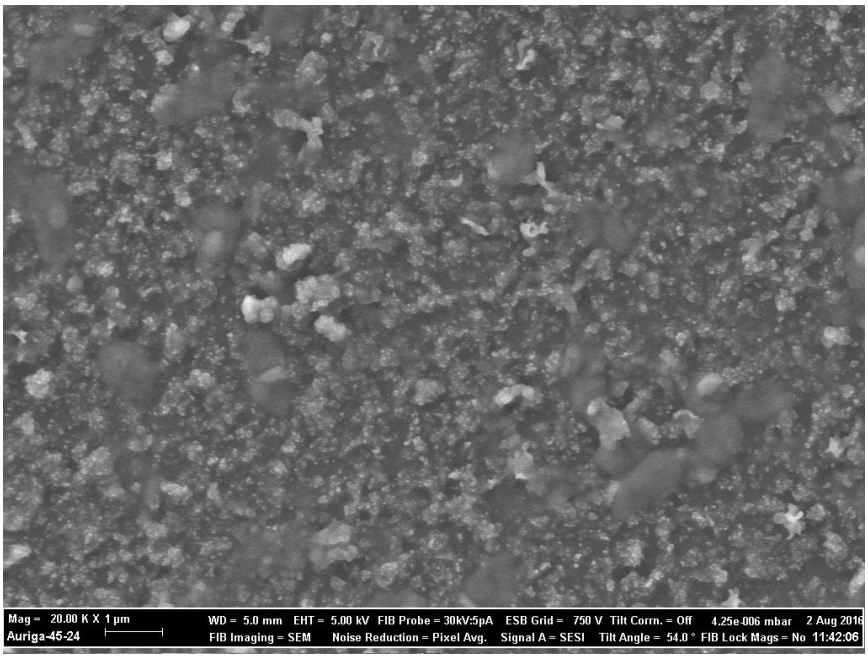

Figure 2.1: SEM micrograph of NeverWet®. The scale bar indicates 1 μm.

2.3 Methods

2.3.1 Sample preparation

Acrylic substrates coated with HPSA and TiO_2 paint were attached to the acrylic with double sided tape (Lu et al., 2015). Neverwet is sold as a two spray coat. The top coat was attached to the acrylic substrates by spraying firstly a base coat provided by the manufacturer to the surface of the acrylic substrate.

Each piece of acrylic was placed in a plastic container immersed in deionized water, shown in Figure 2.2. The contact angle was measured by placing $10\mu L$ droplets of deionised water dyed with methylene blue onto the super-hydrophobic surface. The droplet image was obtained using a camera IPEVO Point 2 View (IPEVO, United States) and the angle was determined using MB-Ruler software of Dance Patterns Company (Iffezheim, Germany). In this method the angle is determined by the user, oppositely to other methods of contact angle measurement that use built-in software, such as in drop-shape analysis equipment. Chakraborty et al. (2013) used the same

Figure 2.2: Sample immersed in water.

software used in this study, MB-Ruler, and found an error of 2° in their contact angle measurements. In the experiment presented in this chapter this is sufficiently accurate for the intended purpose: to distinguish between hydrophilic (contact angle below 90°), hydrophobic (contact angle above 90°) and super-hydrophobic surfaces (contact angle above 150°). Therefore, large contact angle measurement errors (e.g. 5°) are not relevant in this experiment when compared with the 60° difference between hydrophobic and super-hydrophobic contact angles. The rolling angle was measured by placing $10\mu L$ droplets of deionised water dyed with methylene blue onto the super-hydrophobic surface and the inclination of the surface (rolling angle) was determined using a digital inclinometer (Max Measure, United Kingdom).

Pieces of acrylic coated with super-hydrophobic materials were placed in plastic containers and filled with deionised water, as shown previously in Figure 2.2. The plastic containers were placed in a equipment with wooden discs attached to the side. These discs rotate and promotes mixing of the fluid around the samples (Figure 2.3).

2.3.2 Sample analysis

To evaluate their degree of hydrophobicity, the contact angle and rolling angle were measured for all samples at times t at 1, 3, 6, 25 and 50 hours, then every 24 hours up

Figure 2.3: Plastic containers placed in an equipment with wooden discs attached to the side. The wooden discs rotate, preventing stagnation of the water in the plastic containers. The motion of water in the plastic containers contributed to the depletion of air trapped on the surface of the super-hydrophobic coatings.

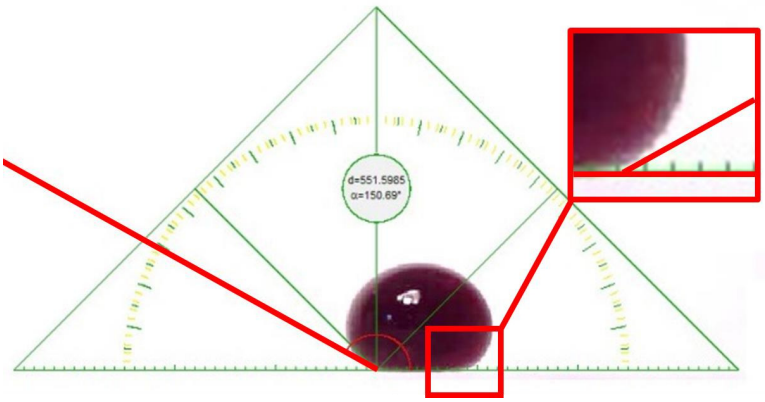

Figure 2.4: Measurement of contact angle of droplet of water dyed with methylene blue using software MB-Ruler.

to 362 hours. Figure 2.4 shows an example of how the contact angle measurements were taken in this experiment. Pictures were taken of a droplet of 10 μL died with methylene blue (methylthioninium chloride) on the sample, which were analysed at the end of each cycle using the software MB-Ruler®. Chakraborty et al. (2013) used MB-Ruler to determine the contact angle of super-hydrophobic surfaces and reported an error of 2°.

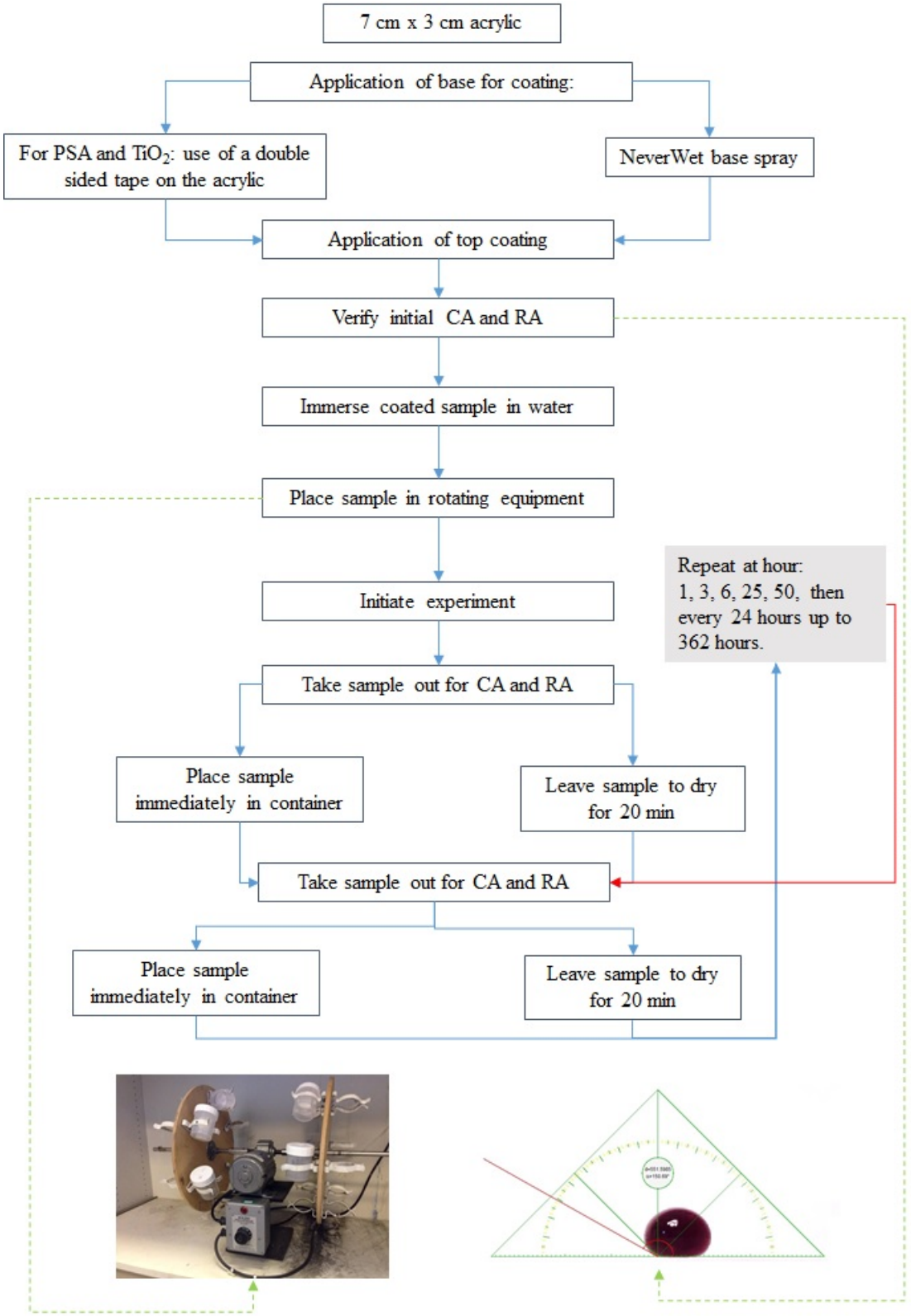

Figure 2.5: Diagram of experimental procedure for super-hydrophobic coating durability test.

Figure 2.5 shows a diagram of the experimental method to evaluate the loss of super-hydrophobic effects over time. The equipment is shown in the bottom left where plastic containers filled with water and containing one coated sample each were attached to wooden discs. The speed of the rotating wooden discs was set to 20 revolutions per minute. The coatings were attached to pieces of acrylic as described previously. Their contact and rolling angles were measured prior to immersion in water. Then, each sample was placed in the plastic container and filled with water as shown in Figure 2.2. At specific times t, the equipment was stopped and samples taken out for measurements of contact and rolling angles. The Samples were taken out of the water and split into two groups: dried and non-dried, each done in triplicates.

For the non-dried group, the contact and rolling angle was determined immediately after the samples were taken out of the water. For the dried group, the samples were dried for 20 minutes at room temperature before measuring the contact angle. This was done to study whether the loss of super-hydrophobicity is recoverable. Figure 2.6 illustrates the difference between the two groups graphically.

2.4 Results and discussion

The contact angle and rolling angle were measured for all the samples. Each result is shown individually in the graphs in Figures 2.7 and 2.8. Each group (dried, non-dried) and super-hydrophobic coating (Neverwet (NW), HPSA and super-hydrophobic TiO_2 paint) is represented by a different colour and symbol. The loss of hydrophobicity differed for the three coatings, specially between the two attached with double-sided tape (HPSA and TiO_2 paint) and the one attached with a base coat (NeverWet®).

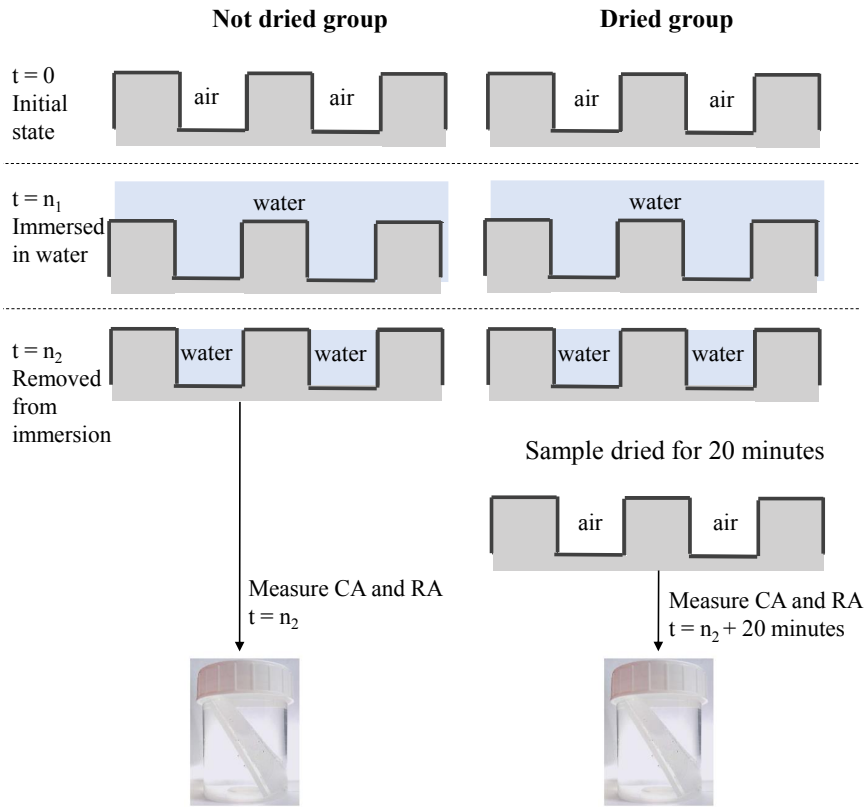

Figure 2.6: Illustration of the two groups: dried and non-dried samples. In both cases air had been replaced with water (Wenzel state). In the dried group, samples were left at ambient temperature for 20 minutes to dry. Air replaced the areas filled with water and transition back to the Cassie-Baxter state.

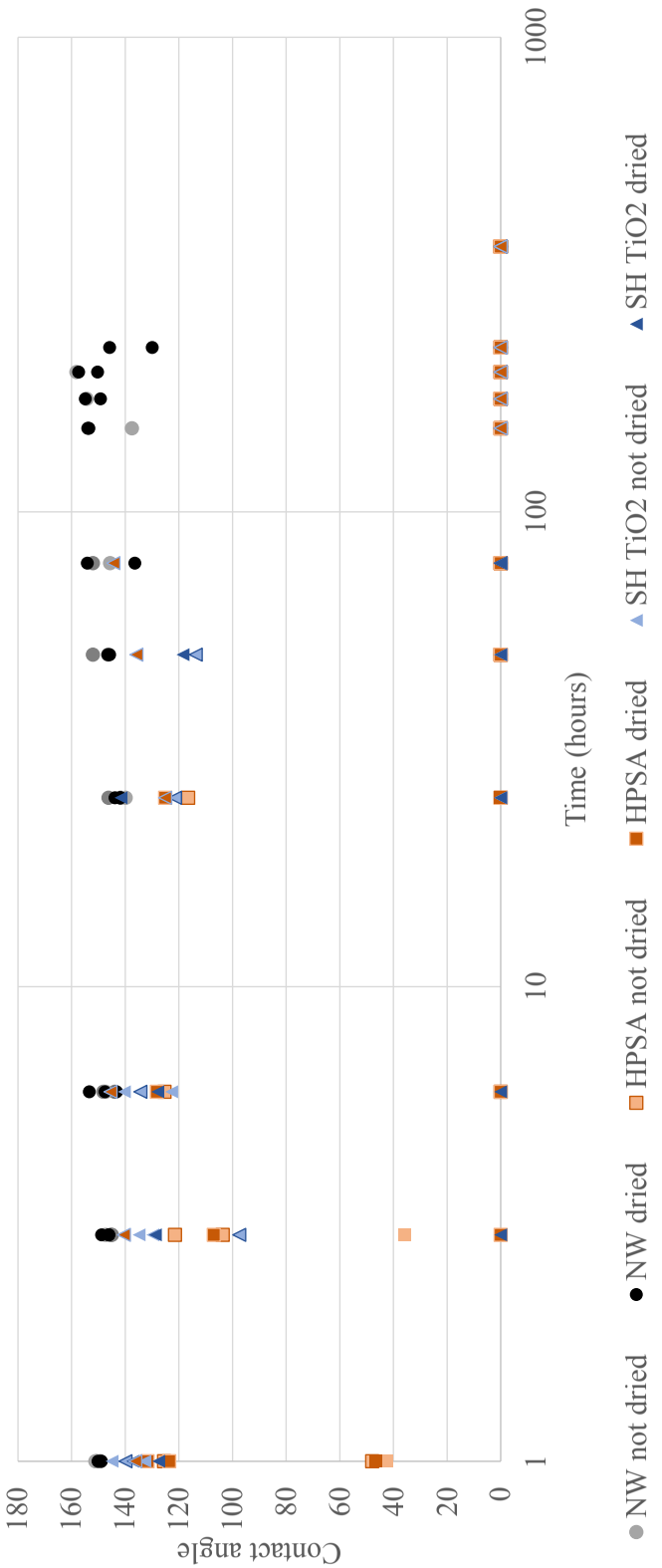

Figure 2.7: Evolution of contact angle over time of the three super-hydrophobic coatings, divided into dried and non-dried groups.

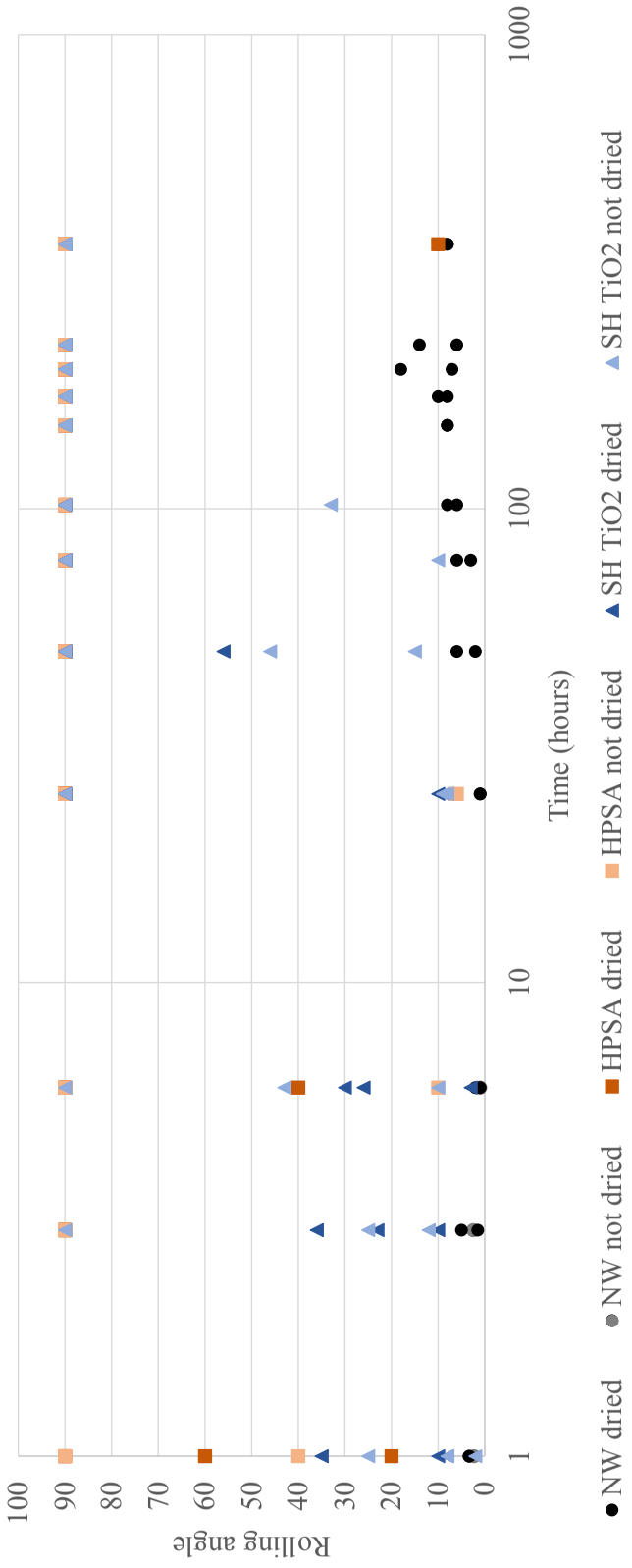

Figure 2.8: Evolution of rolling angle over time of the three super-hydrophobic coatings, divided into dried and non-dried groups.

2.4.1 Hydrophobic Paper Sludge Ash

HPSA samples transitioned rapidly to the Wenzel state. HPSA samples lost some hydrophobicity during the first hour, and by the 6^{th} hour five out of six samples no longer presented hydrophobicity. An example of a sample before initiating the experiment (Figure A.1) and after 3 (Figure A.2) and 6 hours (Figure A.3) of immersion in water is shown in Appendix A. Both dried and non-dried groups lost hydrophobicity completely, indicated by both decrease in the water contact angle and rapid increase of rolling angle.

The non-dried group presented a slightly higher averaged contact angle than the dried group in the third hour, which was simply because some samples of the non-dried group were still intact. Since the dried group did not recover super-hydrophobicity, it is inferred that the air pockets could not be recovered because the surface structure was damaged beyond recovery. In some areas the powder was present on the sample but did not present hydrophobicity and had absorbed the blue-dyed water, indicating that the surface had lost the trapped air from the rough structure. In some areas of the surface coated with HPSA, the double sided tape could be be seen, which confirmed the loss of the surface structure.

2.4.2 TiO_2 paint

The sample coated with TiO_2 super-hydrophobic paint lost some of its hydrophobicity from the 27^{th} hour, partially due to loss of particles, but note there were areas on the sample where powder was present but which did not present hydrophobicity and had absorbed the blue-dyed water, similarly to HPSA results. Samples coated with TiO_2 began to lost hydrophobicity on the edges of the acrylic. An example of sample before initiating the experiment and after 3 and 78 hours of immersion in water is shown in Figure A.2 in Appendix A.

The non-dried group samples lost hydrophobicity completely by the 50^{th} hour and

the dried group by the 78^{th} hour. The TiO_2 paint remained attached to the substrate for longer periods than the HPSA coating, and the slower loss of hydrophobicity of the dried group indicates that the air pockets, and consequently the Cassie-Baxter state, were recovered in some areas of the surface.The surface structure remained intact in those areas for a period of approximately 50 hours - after the 50^{th} hour the contact angle dropped below 90°and thus became hydrophilic.

2.4.3 NeverWet®

Samples coated with NeverWet® presented longer periods of hydrophobicity, that lasted longer on the centre of samples rather than on the edges. The edges began to lose hydrophobicity on the 25^{th} hour of immersion in water, and by the 50^{th} hour one sample (non-dried) had already lost most of its hydrophobicity. By the 150^{th} hour two non-dried and one dried samples had lost almost completely their hydrophobic properties. An example of sample before initiating the experiment and after 3 and 78 hours of immersion in water is shown in Figure A.3 in Appendix A.

The loss of hydrophobicity could have been caused by three effects: a) damage of the surface structure (such as loss of micro to nano-particles) (Jenner et al., 2013); b) loss of trapped air into water (Bobji et al., 2009, Lee & Kim, 2011); or c) hydrophilization due to chemical interaction between water and the organosilane coat (Boinovich et al., 2010). The latter is less probable since Boinovich et al. (2010) reported that the change in chemical composition occurred as a second stage process, occurring only a few days after exposure to water.

The loss of nano-particles was confirmed with SEM and the loss of air trapped on the surface was confirmed by placing a sample coated with NeverWet® in an ultrasound bath for 10 seconds. Ultrasound bath, or ultrasonic cleaning is a process that uses ultrasound to vibrate a fluid at a certain frequency. The sample inside the ultrasonic bath is agitated promoting the detaching of particles glued onto the surface. The ultrasonic bath simulated an environment subjected to vibrations. Once the sample

was placed in the ultrasound bath air bubbles were observed leaving the surface of the sample and when removed, the surface of the sample was completely wet. After drying, the surface recovered its super-hydrophobicity (recovered the Cassie-Baxter state) but when immersed for 3 minutes the super-hydrophobicity was lost completely. SEM micrographs shown in Figure 2.9 confirmed that the surface was intact and the loss of air layer was the cause of the loss of hydrophobicity.

2.5 Conclusions from preliminary experiment

The loss of super-hydrophobicity was quantified by changes in the contact and rolling angle. HPSA samples lost hydrophobicity earlier than TiO_2 paint and NeverWet in both non-dried and dried groups. Results of contact and rolling angle show that the non-dried group of samples coated with TiO_2 paint and NeverWet lost their hydrophobicity earlier than the dried group. Non-dried samples coated with TiO_2 paint lost hydrophobicity completely by the 50^{th} hour. Non-dried samples coated with NeverWet® lost their hydrophobicity completely by 150 hours of immersion in water - one by the 25^{th} hour, one by the 50^{th} and two by the 150^{th} hour. The loss of air was confirmed by placing samples coated with NeverWet® in a ultrasound bath for 10 seconds. Air bubbles were observed leaving the surface and recovered their super-hydrophobicity after the sample was dried.

Results showed that loss of hydrophobicity occurred also due to loss of micro- to nano-particles that composed the rough structure. SEM micrographs confirmed that the surface structure of NeverWet® was intact when subjected to small periods in the ultrasound bath, but longer periods caused damage to the surface structure by loss of particles that form the rough surface.

The dried group of samples coated with TiO_2 paint lost hydrophobicity completely by the 78^{th} hour, whilst dried samples coated with NeverWet® remained hydrophobic after 200 hour immersion in water. Samples in the dried groups were dried before

a)

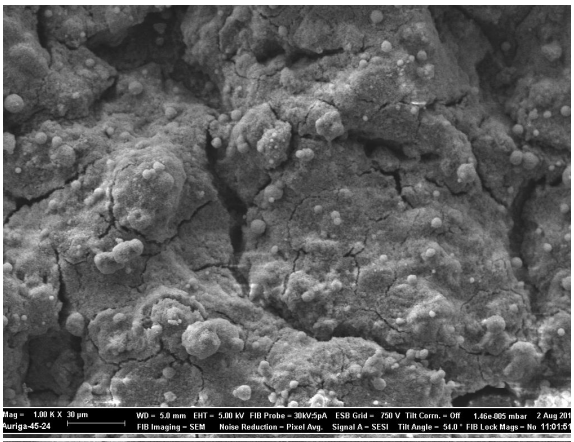

b)

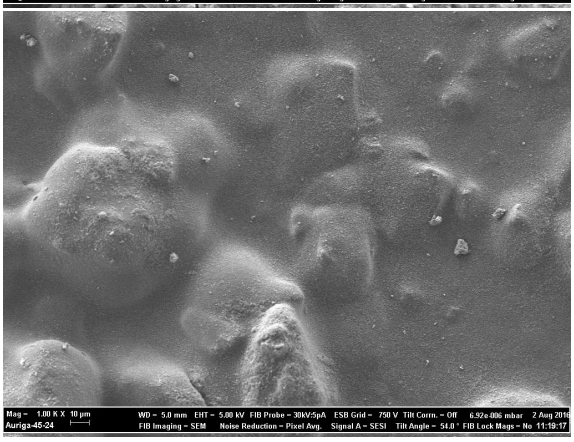

c)

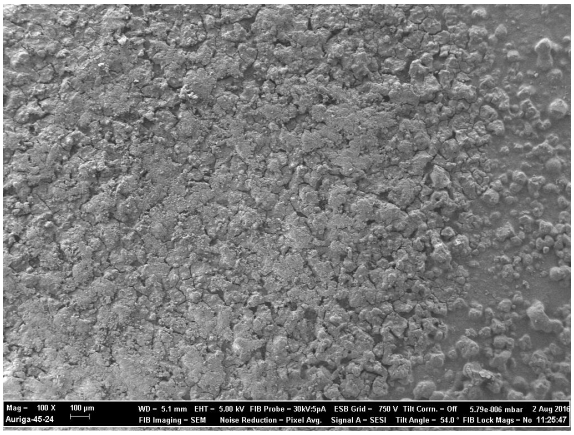

Figure 2.9: SEM micrographs of surface coated with NeverWet® before and after immersion in ultrasound bath for 3 minutes. a) Surface of NeverWet® before immersion in ultrasound bath; b) Surface of NeverWet® after immersion in ultrasound bath. It can be seen that the surface is less rough than before immersing in the ultrasound bath; c) The transition between parts of the surface that were still super-hydrophobic after immersion in ultrasound bath was captured in this SEM micrograph. In the bottom right corner it is seen that the surface is less rough than the rest of the figure.

measurement and re-immersion, providing the opportunity for the air pockets to reform and thus the hydrophobicity to recover. Results indicate that the Cassie-Baxter state can be recovered simply by drying the samples once the surface had transitioned to the Wenzel state, as long as the the surface structure is intact. The dried group of samples coated with NeverWet® retained higher contact angles than the other super-hydrophobic coatings because the particles were attached to the substrate using a special adhesive, provided by the manufacturer in the the form of base coat. HPSA and TiO_2 paint were attached to the substrate with double sided tape, which contributed to the loss of surface particles since there was no strong bond between the particles, and between the particles and the substrate.

Generally, dried groups presented longer periods of lower rolling angles and higher contact angles due to recovery of the air pockets, but eventually the loss of super-hydrophobic effects caused by loss of surface structure was irreversible.

The experiments conducted in this chapter indicate that an ideal super-hydrophobic material that is constantly in contact with water should be resilient to the loss of its surface structure, and capable of replacing air that is lost from the surface. The coatings used in this chapter are not suitable for application in the water industry as the loss of trapped air occurred within days. The damage of the surface structure could be overcome with more robust materials. However, the transition from Cassie-Baxter to Wenzel state is inevitable, independently of the surface coating. Therefore, a robust super-hydrophobic material applied as a drinking water pipe must be able to recover the Cassie-Baxter state.

3

Manufacturing a porous material with a super-hydrophobic surface

3.1 Introduction

Chapter 2.3 demonstrated that super-hydrophobic coatings are only able to maintain the Cassie-Baxter state for a few hours under immersion in water. Moreover, all coatings were permanently damaged within 150 hours, as was seem in SEM images. The low durability of the super-hydrophobicity prohibits the application of these coatings for drinking water transport. Therefore, a different approach must be taken. In this chapter, the manufacture of a novel super-hydrophobic material is presented which is capable of recovering the Cassie-Baxter state by applying an air across the material.

In Chapter 1 four methods to recover the trapped air pockets, i.e. the Cassie-Baxter state, were mentioned, including injecting air with a needle, and produce air pockets by hydrolysis of water by placing small electrodes across the surface. As purposely

producing hydrogen is unacceptable for use in water distribution due to the safety risks, it was decided that injecting air into the air pockets was the most suitable approach. However, since it is unacceptable to place objects in the pipe, an alternative to air injection by needles had to be sought. This led to the idea to manufacture a porous material, so air could be blown through the material and replenish the air pockets. This has the additional benefit of homogeneous replenishment of the air pockets, which is likely to improve performance.

A well known method to produce porous materials is by sintering of metal or/and ceramic powders (Kang, 2005). Sintering is a technique applied to metal or/and ceramic powders to produce density-controlled materials by applying thermal energy (Kang, 2005). Initially, samples were produced by sintering of pressed soda-lime glass in a hydraulic press. This method is described in Appendix B.1 and was discontinued because pressing fine powder produced smoother samples than by sintering the particles loose. It was observed from the results in Appendix B.1 that the sintering of loose particles could be the solution to form a porous material with a rough surface. Surface roughness is of great importance to form surfaces with the Cassie-Baxter state. To manufacture a porous material with a rough surface by sintering of a powder, soda-lime glass powder was used instead of a metal powder because it has a lower melting point. In addition, previous studies have produced super-hydrophobic surfaces on silica substrates that were modified with hydrophobic chemicals (Crick & Parkin, 2011, Zhang et al., 2016b, Dou et al., 2016). The surface of soda-lime glass is rich in SiO_2 and SiOH and to form a hydrophobic surface, soda-lime glass was initially modified with surface modifying agent (SMA), such as hexamethyldisilazane (HMDS). SMAs such as HMDS have been shown to provide a hydrophobic tail to the silica molecules of the tile. Nanoparticles of various compositions coated with HMDS have shown to present super-hydrophobic properties (Tao et al., 2016, Crick & Parkin, 2011). Tao et al. (2016) demonstrated that hollow silica nanoparticles coated with HMDS presented a maximum water contact angle of 156°, and Crick & Parkin (2011) obtained water contact angles approaching 180° from functionalised silica microparticle film treated with HMDS by deposition using chemical vapour

deposition (CVD). Tao et al. (2016) and Crick & Parkin (2011) produced super-hydrophobic particles of similar surface chemistry, but with different water contact angles.

The effect of roughness and surface-modifying agent (SMA) on the super-hydrophobicity was investigated by manufacturing soda-lime glass powder samples with various particle sizes, ranging from $\leq 45\ \mu m$ to $500\ \mu m$, and the surface chemistry was modified by applying a surface modifying agent hexamethyldisilazane. Two types of samples of specific size ranges were produced - samples made with one range of particle size, and samples made with a mixture of a particle size range with added particles of size diameter $d_g \leq 45 \mu m$. The latter was done because dual scales hierarchical structure creates a suitable surface geometry in super-hydrophobic surfaces (Li & Amirfazli, 2008).

3.2 Effect of particle size and roughness on the hydrophobicity of sintered soda-lime glass surfaces

In the previous chapter a preliminary study showed that super-hydrophobic coatings lose super-hydrophobicity by detachment of particles from the surface. The use of sintering provides a solution to the detachment of particles from the surface. Sintering is the thermal treatment of a powder, where the material is heated to a temperature below the sintering point of the powder. Sintering of the surface of particles bonds particles together is illustrated in Figure 3.1.

3.2.1 Materials

Soda-lime glass powder was obtained from clear bottles. A crucible of dimensions 10.6 cm × 5.3 cm × 2.0 cm was used to sinter the samples. A reference sample of smooth soda-lime glass microscope slide (SG) was used to compare the water

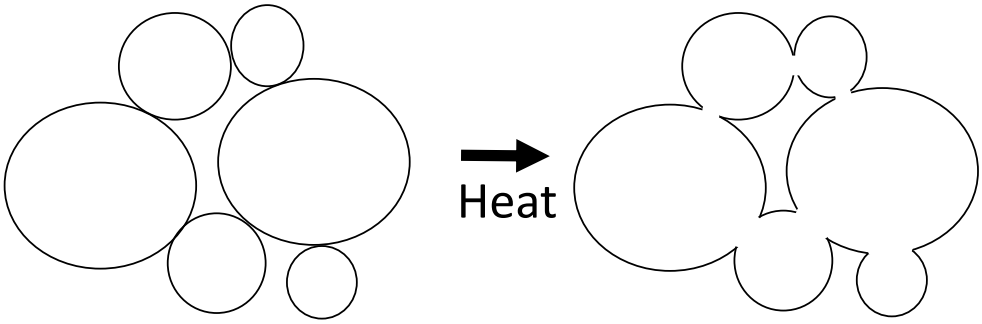

Figure 3.1: Illustration of the sintering process. Loose particles are heated up and the surface of particles sinter, forming a porous material.

contact angles between roughened and non-roughened surfaces. Hexametyldisilazane (HMDS) and anhydrous toluene were purchased from Merck®(Germany). Deionised water was used to measure the water contact angle.

3.2.2 Methods

Soda-lime glass powder was obtained from crushing clear bottles in a hammer-mill. The bottles were initially broken into smaller pieces with a hammer. The smaller pieces were fed to a hammer mill. The hammer mill was fitted initially with a larger perforated sieve, and as the glass pieces became smaller from grinding, the resulting particles were fed repeatedly to the hammer mill, and the sieves with larger mesh aperture were replaced by sieves with smaller aperture. The sieves aperture sizes ranged from 1 to 5 mm. Then, the granules formed were sieved using a mechanical sieve shaker into different particle diameter (d_g) with $355 \leq d_g \leq 500\ \mu m$, $212 \leq d_g \leq 355\ \mu m$,$75 \leq d_g \leq 212\ \mu m$, $75 \leq d_g \leq 150\ \mu m$, $45 \leq d_g \leq 75$ and $d_g \leq 45\ \mu m$.

The sintered rough soda-lime glass samples and the smooth reference sample of hydrophilic soda-lime glass were placed in a solution containing HMDS (20% v/v in toluene) and heated to 40°C. The surface of sintered glass is rich in SiO_2 and

Si-OH groups, and reacted with HMDS. This has the structure shown in Figure 1.8. Porous glass tiles were then formed by controlling the blend of glass particles in a homogeneous mix that was loosely packed into the alumina crucible and fired in an electric furnace at a range of temperatures of 660-680°C for 30 minutes, as shown in the results section in Table 3.1. Blends with 50% d_g $\leq$45 μm powder were produced in order to create a hierarchical surface, inspired by the work of Li & Amirfazli (2008). Each 10 gram mix was placed loosely in an alumina crucible. The crucible was then placed in a pre-heated furnace at 200°C, and heated to the desired sintering temperature, as shown in Table 3.1 along with each sample's composition. The ideal sintering temperature was determined experimentally. The ideal temperature for this purpose was determined by sintering samples in a furnace ranging from 660°and 690°C. The lowest temperature at which samples reached minimum particle bonding and were able stick together was 680°C, and for sample with $d_g \leq 45$ μm at 660°C produced sufficient particle bonding. At temperatures below 660°C sintering did not occur and above 680 °C the contact angle for all samples was below 90°.

Samples were analysed according to their water contact angle by placing a droplet of deionised water on the top of each surface, and the angle was determined using an automated goniometer with Ramé-Hart DROPimage software (Ramé-Hart DROPimage goniometer, Ramé-Hart Instruments Co., USA). The automated goniometer places a droplet of a liquid onto a surface and the software Ramé-Hart DROPimage detects the shape of the droplet at the surface, and determines the water contact angle. A minimum of nine contact angle measurements from water droplets were taken.

Scanning Electron Micrographs of samples were produced to observe the surface structure of samples using a Scanning Electron Microscope (SEM) Jeol JSM-6400 (JEOL Ltd., Japan). Samples analysed with SEM images were coated with 10 nm of gold.

Table 3.1: Resulting water contact angles of samples of various particles modified with HMDS. Samples A-E were made with 10g of one size range, and samples F-I were made with 5g of two size ranges each, to a total of 10g.

	Size range					Temperature	Contact angle
Sample	355-212	212-150	150-75	75-45	<45	(°C)	(°)
A	10g					680	122 ± 3
B		10g				680	115 ± 6
C			10g			680	116 ± 11
D				10g		680	130 ± 11
E					10g	660	136 ± 6
F	5g				5g	680	113 ± 0.5
G		5g			5g	680	125 ± 4
H			5g		5g	680	117 ± 4
I				5g	5g	680	132 ± 3
SG							93 ± 0.5

3.2.3 Water contact angle of sintered soda-lime glass surfaces modified with HMDS

Table 3.1 shows the composition of soda-lime glass granules, the temperature at which they were sintered together with the mean water contact angle of a droplet of water resting onto the surface of each sample.

None of the samples presented in Table 3.1 have water contact angles above 150° and therefore they are not super-hydrophobic. However the contact angle of samples presented in Table 3.1 are at least 20° higher than the smooth reference sample. This indicates that samples had some areas in the Cassie-Baxter state of wetting, trapping air pockets in the asperities of the surface. The contact angles of a water droplet on the surfaces presented in Table 3.1 are approximately 30-40° below the ones presented by Tao et al. (2016) and Crick & Parkin (2011). The highest contact angle in Table 3.1 was obtained for the surface formed with lowest particle size range

(sample E). Samples E, D, G and I showed higher water contact angles than the other samples. Samples D, G and I were formed of particle sizes in the ranges 212-150 μm, 75-45 μm and $\leq$45 μm. Therefore samples of size range 355-212 and 150-75 μm were discarded for the following experiments and analysis.

3.2.4 Scanning Electron Micrograph of sintered soda-lime glass surfaces modified with HMDS

SEM micrographs of tiles made of size ranges 212-150 μm (B and G), 75-45 μm (D and I) and $\leq$45 μm (E) are shown in Figure 3.2. Samples E, G and I showed higher water contact angles (Table 3.1). The relative roughness of sample surfaces will be discussed in the following Chapter 4. The large particles in samples D and B appear clearly in the SEM pictures. The contact angle of a droplet on a super-hydrophobic surface is affected by the area of contact between the solid-liquid interface. Therefore it can be inferred from the SEM pictures and results in Table 3.1 that the resulting contact angle is dependent on the particle size that was used to manufacture the porous samples because the arrangement of the glass particles resulted in different degrees of relative surface roughness. The relative surface roughness is the ratio of peaks and valleys compared to a smooth surface. In Figure 3.2 it is evident that the surface of Sample G is covered with smaller particles. Sample G is a combination of 50% of particles in the range $\leq$45 μm and 50% 212-150 μm. Particles of size range d_g $\leq$45 μm remained on the surface, covering the larger particles of size range 212-150 μm, therefore increasing the surface roughness. Conversely, in Sample I the two particle size ranges were well blended and are shown on the surface of Sample I in Figure 3.2 b.

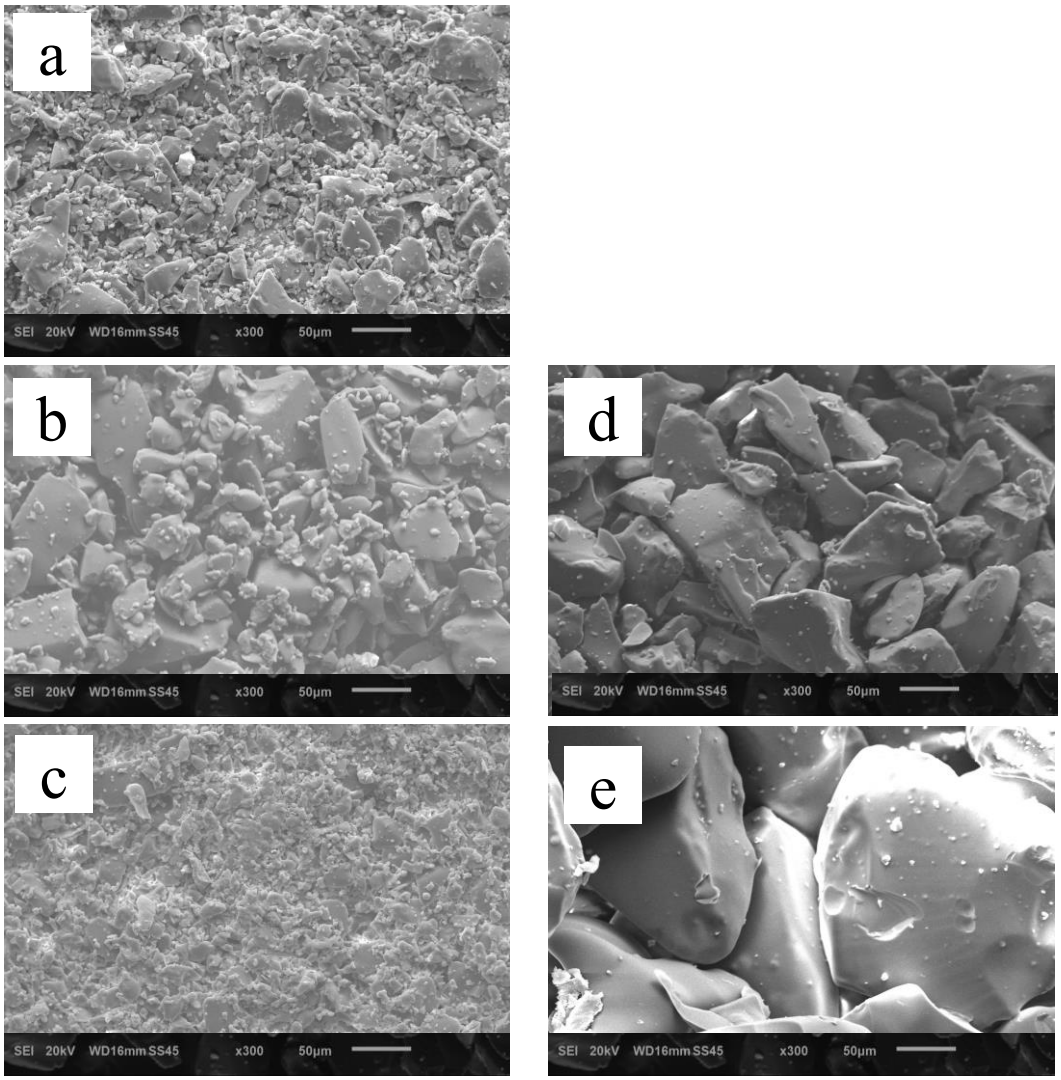

Figure 3.2: SEM micrographs of samples B, D, E, G and I. a) Sample E size range d_g $\leq$45 μm, b) Sample I with size range d_g 75-45 μm + 50% d_g $\leq$45 μm, c) Sample G with size range d_g 212-150 μm + 50% d_g $\leq$45 μm d) Sample D with size range d_g 75-45 μm, and e) Sample B with size range d_g 212-150 μm.

3.3 Effects of PFTS and POTS on the contact angle

The results in Table 3.1 indicate that changes in the surface roughness of a hydrophobic surface result in changes in the water contact angle when compared with the smooth reference sample. Samples D, E and I obtained higher water contact angles because the combination of surface roughness and a hydrophobic surface resulted in a surface with areas in the Cassie-Baxter wetting state.

Results from Table 3.1 and previous studies (Li & Amirfazli, 2008, Daniello et al., 2009, Ybert et al., 2007) indicate that the size of features on super-hydrophobic surfaces affect the water contact angle and friction on the water-solid interface. Since the results in Table 3.1 were below expected and did not reach 150° water contact angle, characteristic of super-hydrophobic surfaces, another soda-lime glass sample with particle size distributions of 50% cumulative mass (d_{50}) up to 18.0 μm and 90% cumulative mass (d_{90}) up to 80 μm were studied (Sample ST) (Trovotech GmbH, Germany). Using a commercial soda-lime glass powder is advantageous because it eliminates the step of producing soda-lime glass powder by hammer milling.

Using HDMS as a surface-modifying agent did not result in super-hydrophobic surface properties (Table 3.1). Thus, the hydrophilic samples D, E, I and ST were modified with two other SMAs:

1. trichlorotrichloro(1H,1H,2H,2H-perfluorooctyl)silane (PFTS; Figure 3.3);
2. 1H,1H,2H,2H-perfluorooctyltriethoxysilane (POTS; Figure 3.4).

An example of the reaction between the $Si(Cl)_3$ group in PFTS and OH group in the surface of soda-lime glass is shown in Figure 3.5. SMAs containing carbon-fluorine bonds such as Trichloro(1H,1H,2H,2H-perfluorooctyl)silane (PFTS), polytetrafluoroethene (PTFE, Teflon®) and 1H,1H,2H,2H-Perfluorooctyltriethoxysilane (POTS) are often used to reduce the surface energy of materials and decrease the interaction between a fluids and a solid surface containing these materials. Moreover, HMDS,

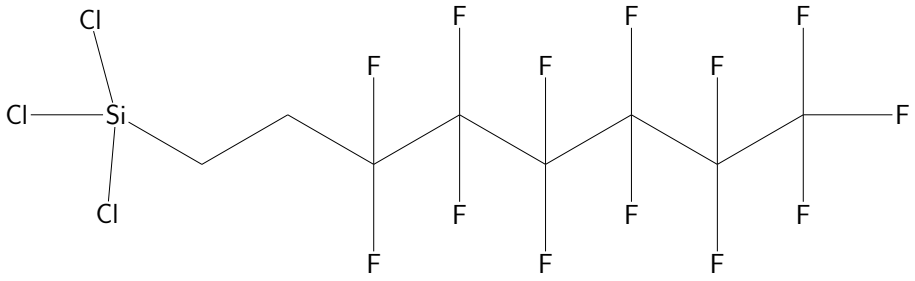

Figure 3.3: Molecular structure of trichloro(1H,1H,2H,2H-perfluorooctyl)silane.

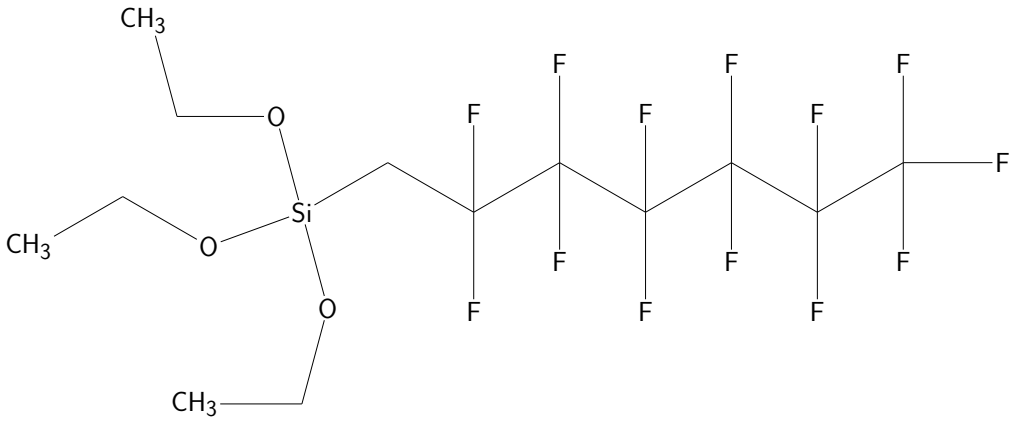

Figure 3.4: Molecular structure of 1H,1H,2H,2H-perfluorooctyltriethoxysilane.

PFTS and POTS have been applied to hydrophilic surfaces containing Si-O bonds (Crick & Parkin, 2011, Zhang et al., 2016b, Dou et al., 2016).

3.3.1 Materials and Methods

Porous soda-lime glass samples were prepared as in section 3.2. The surface modification with POTS was achieved by immersing each sample in 1% (v/v) solution of 1H,1H,2H,2H-perfluorooctyltriethoxysilane diluted in toluene (Sigma-Aldrich, USA) for 8 hours at 40 °C. The SMA treated samples were then dried at room temperature for 24 hours. The surface modification with PFTS occurred by immersing each sample in a solution containing 1% (v/v) of trichloro- (1H,1H,2H,2H-perfluorooctyl)silane

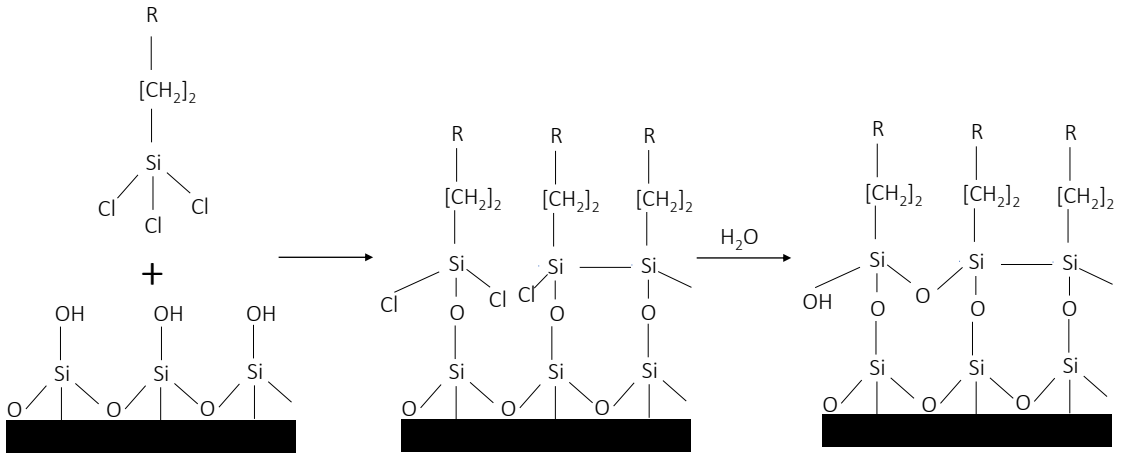

Figure 3.5: Schematic example of reaction between PFTS and glass surface rich in hydroxiles. According to Oyola-Reynoso et al. (2015) PFTS and POTS react with OH groups on the surface to either form a covalent or hydrogen bond. R = $CF_3(CF_2)_6$.

in toluene (Sigma-Aldrich, USA) for 8 hours at 40 °C. The SMA-treated samples were dried at room temperature for 24 hours (Walker et al., 2016, Crick & Parkin, 2011, Ahsan et al., 2013, Chen et al., 2016). The sample was then placed in deionized water at room temperature for 24 hours, and dried at room temperature again for 24 hours. An example of the results of the reaction between the $Si(Cl)_3$ group in PFTS and OH group in the surface of soda-lime glass is shown in Figure 3.5. Samples were analysed according to their water contact angle by placing a droplet of deionised water on the top of each surface, and the angle was determined using an automated goniometer with Ramé-Hart DROPimage software (Ramé-Hart DROPimage goniometer, Ramé-Hart Instruments Co., USA). A minimum of nine contact angle measurements from water droplets were taken.

3.3.2 Water contact angle of sintered soda-lime glass surfaces modified with PFTS and POTS

The results of water contact angles of soda-lime glass samples reacted with POTS and PFTS are presented in Table 3.2.

Table 3.2: Contact Angle of porous surfaces modified with PFTS and POTS.

SMA	Sample	Contact Angle (°)
PFTS	D	149 ± 5
	E	144 ± 3
	I	146 ± 5
	ST	153 ± 4
POTS	D	132 ± 10
	E	136 ± 8
	I	145 ± 5
	ST	137 ± 1

Even though most samples shown in Table 3.2 still presented contact angles below 150°, there was a significant increase in the contact angle between the PFTS/POTS-modified samples and HMDS. The samples reacted with PFTS presented, on average, higher contact angles than samples reacted with POTS, and both results indicate the presence of the Cassie-Baxter state from the increased contact angle as a result of higher relative roughness and hydrophobicity of the modified material. Sample ST showed the highest mean contact angle of 153°, indicating super-hydrophobicity.

3.4 Conclusions

In this Chapter it was demonstrated that the porous glass tiles made of sintered soda-lime glass particles and modified with SMA presented the Cassie-Baxter state of wetting, with air pockets trapped between the asperities of the surface. A smooth soda-lime glass substrate modified with HMDS (sample SG) presented a water contact angle of 93°, which was increased by manufacturing a rough soda-lime glass

surface by sintering of soda-lime glass powder. Smaller particles resulted in higher contact angles.

Two main factors affect the water contact angle: relative surface roughness and chemical affinity (hydrophobicity). Firstly the relative surface roughness was investigated for a surface modified with HMDS. It was found that the surface roughness plays an important role in manufacturing a surface with the Cassie-Baxter wetting state. Samples D, E and I were formed with smaller particle sizes, thus with more potential to present rougher surfaces, presented the highest contact angles when modified with HMDS. The Hydrophilic samples that were modified with PFTS and POTS were demonstrated to be more hydrophobic than surfaces treated with HMDS. Sample ST showed the highest contact angle of 153° and samples D and E had contact angles very close to super-hydrophobicity. Sample I presented contact angles approaching 150° when reacted with PFTS and POTS, but overall samples D and ST presented more measurements of contact angle approaching 150° when reacted with PFTS, and sample E presented the highest contact angle when reacted with HDMS. In the light of this, samples D, E and ST were selected to the next step of this research, which is to investigate whether these samples are able to recover the Cassie-Baxter state under static water pressure.

4

Surface characterisation and recovery of the Cassie-Baxter state under immersed conditions

4.1 Introduction

This chapter presents an analysis of the best performing materials produced in chapter 3. As a result of the findings in chapter 2.3, super-hydrophobic coatings have been discarded as suitable materials for drinking water pipe applications as they quickly transition from the Cassie-Baxter state to the Wenzel state and their surface structure can be easily damaged. Chapter 3 presented a solution for the recovery of air pockets and robustness of the surface. The analysis of the materials produced in chapter 3 was narrowed down to the three best performing samples - D, E and ST.

This chapter presents: a) the characterisation of the surface of samples D, E and ST using SEM micrographs, x-ray tomography and FTIR spectroscopy; b) the ability of

the new material to recover the Cassie-Baxter state under fully immersed conditions; and c) the suitability of the material for drinking water applications by measuring possible changes in the material upon contact with high free chlorine solution.

The characterisation of samples provides an understanding of the surface structure, such as the porosity and pore size throughout the material, relative surface roughness, surface structure and surface chemistry. The ability to recover from the Wenzel to the Cassie-Baxter state is analysed in this chapter and linked to the surface characterisation of samples. The ability of a super-hydrophobic surface to recover the Cassie-Baxter state is key to use the new material in water transport applications. Finally, the robustness of the surface and suitability as a drinking water pipe was measured to ensure that the material maintain its properties upon contact with high free chlorine solution.

4.2 Materials and methods

The samples analysed in this chapter are samples D, E and ST reacted with trichloro-(1H,1H,2H,2H-perfluorooctyl)silane. The method for producing these samples has been described in Chapter 3.

The properties of the new super-hydrophobic material is explored using SEM, FTIR spectroscopy and X-ray tomography, of which the methodology is described below.

4.2.1 Scanning Electron Microscope micrographs

Gold-coated surfaces of the porous glass samples were observed using scanning electron microscopy (SEM, JEOL JSM 6010). The SEM images were analysed to evaluate surface roughness. All pictures were taken using 20kV beam accelerating voltage and adjusted to the same brightness and contrast. Images were taken using magnification of $\times$1000, $\times$500, $\times$300 and $\times$100. The pixels of the images were binarised to

black and white. Areas of higher elevation (i.e. peaks) are bright in the SEM image, while areas of lower elevation such as valleys are dark. When binarised, brighter pixels of value η higher than the threshold η_{tr} were considered white and pixels of $\eta \leq \eta_{tr}$ were considered black. The threshold for pixels of a certain η_{tr} could be changed to analyse the pictures at different threshold values. Percentages of white peak areas were calculated using threshold levels of $0.4 \leq \eta_{tr} \leq 0.6$ using the following equation:

$$\%peaks = \frac{\sum wp}{\sum tp} \tag{4.1}$$

where tp = total pixels and wp = white pixels.

4.2.2 X-ray tomography

Surface roughness and bulk porosity were obtained using x-ray tomography (Phoenix Imaging X-ray, GE Sensing and Inspection Technologies GmbH, Germany) with image processing using MATLAB and ImageJ software. The output of data from the x-ray tomography is a series of 2D images that shows slices of the sample. With ImageJ software, the sliced 2D images were combined to form a 3D stacked image of the samples, as shown in Figure 4.1. The relative surface roughness (R_f) was quantified by measuring the the total surface area and dividing by the flat surface area ($R_f = \mathrm{A}_{peaks}/\mathrm{A}_{flat}$). Relative surface roughness values between 1.2 and 2 have been reported for surfaces in the Cassie-Baxter state with water contact angles of up to 150°(Yang et al., 2006). The total surface area is quantified by measuring the area of peaks and valleys of the surface texture.

The roughness elements of a surface are defined as the repetitive or random deviation from the nominal surface (n_0) that forms the three dimensional topography of the surface (Bhushan (2001)). Figure 4.2 demonstrates that the location of the nominal surface is not straightforward to identify, since the surface profile is highly porous. Methods to analyse the profile of the surface include scanning probe microscopy,

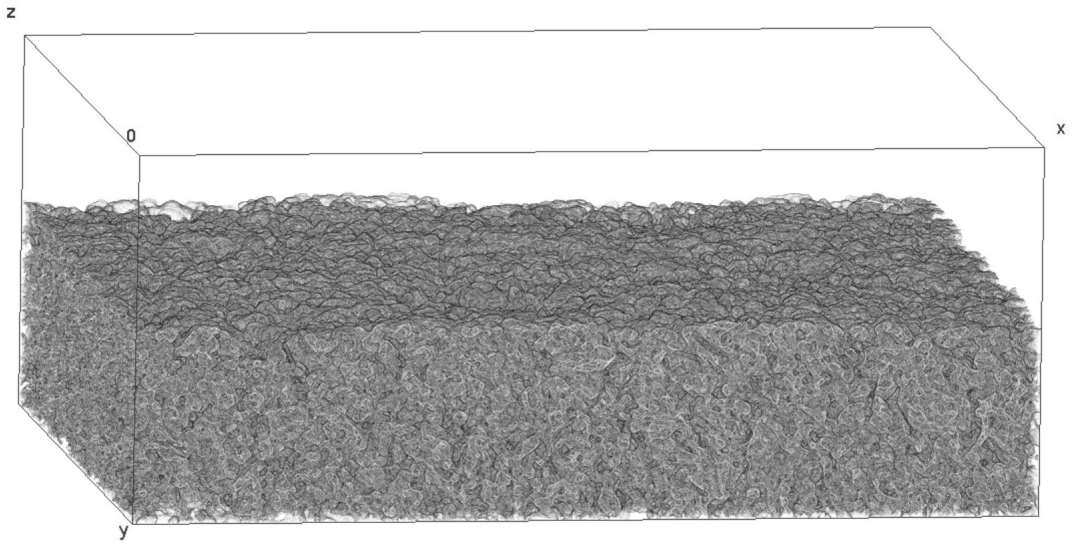

Figure 4.1: 3D-stacked image of sample volume showing the surface roughness and porosity.

mechanical stylus method, optical methods, among others (Bhushan (2001)), that scan the surface by direct contact or by light or electro-magnetic emission/reflection. The nominal surface in those methods are usually determined by the lowest point of contact that the tip (stylus method) or light or electro-magnetic waves reaches. Therefore the nominal surface is being determined from the average position of the most superficial voids, following the stylus method. The images were firstly binarised, so that the value of each voxel of each image was either 0 (black, background) or 1 (white, solid surface)[1] and peaks were given values according to their position in z axis (Figure 4.2).

Once the surface was determined, the surface area was calculated by triangulation of the surface (Figure 4.3). Vectors were created from neighbouring points in x, y and z directions, and the area of the product was obtained from the product of vectors

[1]In Figures 4.1 and 4.2 those were swapped to appear clear to the reader.

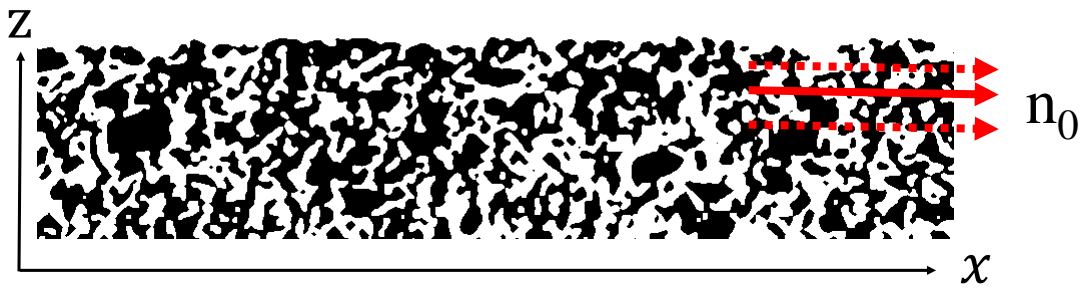

Figure 4.2: Example of binarised slice of porous sample. The X-ray tomography method produces a sequence of slices of the sample, showing the internal structure of the porous material. The black areas are the solid surface, and white areas are the porous channels.

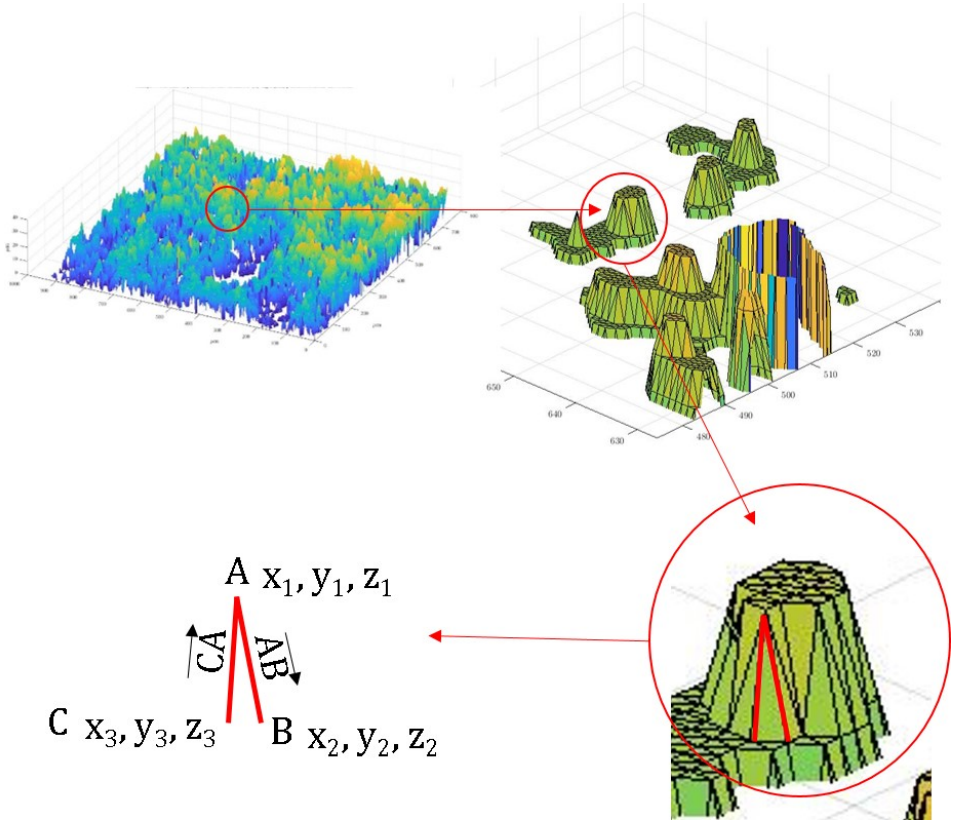

Figure 4.3: Example of surface structure of the porous super-hydrophobic material. The peaks were divided into triangles to facilitate the calculation of the surface area.

$\overrightarrow{AB} \times \overrightarrow{AC}$. The area (A) of each triangle is:

$$A = \frac{1}{2}|\overrightarrow{AB} \times \overrightarrow{AC}| \tag{4.2}$$

The pore diameter 3D distribution of the x-ray tomography scanned samples was evaluated in ImageJ software (Abramoff et al. (2004)) with the BoneJ plugin (Doube et al. (2010)). This module estimates pore size distribution by computing the Euclidean transformation distance (distance between two points) of the segmented pore phase and extracts the distance ridge. In other words, the solid surface is identified and the straight distance between opposite walls is determined. By fitting the largest spheres locally at each point on the ridge the local pore diameter is obtained (Doube et al. (2010), Lu et al. (2017b)). Extracted sub-volumes used for these calculations were all 700x700x700 voxels in size.

4.2.3 Fourier-transform infrared spectroscopy

The functionalisation of the surface was investigated by Fourier transform infrared spectroscopy (FTIR) spectrum, which was collected at room temperature over a scanning range of 400-4000 cm^{-1} with a resolution of 2 cm (Nicolet Magna 560, Nicolet Instrument Corporation, Wisconsin, United States). Two samples were analysed: Dry pristine soda-lime glass and dry soda-lime glass samples functionalised with PFTS.

In FTIR infrared radiation is emitted over a range of wavelengths of 400-4000 cm^{-1}, and the absorption (or transmission) is measured. A FTIR spectrum shows absorption bands that are associated with vibrations of particular functional groups within the molecule. Identifying the bands result in the identification of the molecules that make up a material (Gaffney et al., 2012). The vibrational bands of interest in this research are associated with C-F in the range of 500-700 cm^{-1} and 1100-1300 cm^{-1}, and Si-O-Si bonds in the range of 1000-1100 cm^{-1} (Lu et al., 2017a, Mihály

et al., 2006). The change in transmittance at those regions between pristine soda-lime glass and modified soda-lime glass indicate the reaction between the surface modifying agent and the substrate.

4.2.4 Test cell for immersed super-hydrophobicity recovery tests

The hydrophobic porous glass tiles were analysed according to their ability to recover from the Wenzel to the Cassie-Baxter state under immersed conditions. The samples were sealed into an acrylic container (10.1 × 5.3 × 8.9 cm) using silicone, as shown in Figure 4.4. The sample was marked in the middle with a permanent marker to separate the sample into two sides. The top picture in Figure 4.5 shows the initial state of the sample in the test cell with 10 mm of water on top of the sample. Air pockets on the surface are reflected on the water layer. Air pockets at the porous glass-water interface were associated with a silvery appearance (Daniello et al., 2009), which was recorded using white light (Nikon D5600, Nikon Corporation, Japan). The top surface of the sample was then washed with surfactant solution (sodium dodecyl sulphate surfactant (SDS), diluted 1:800 with water). This altered the surface tension of water and the solid-liquid interface interaction, causing displacement of the air at the surface to produce a fully wet surface in the Wenzel state with low contact angle, illustrated in Figure 4.6. In the middle picture in Figure 4.5 it is shown the right side washed with the surfactant solution to forcibly remove the air pockets and change the wetting state to Wenzel, and the left side, that remained intact. Tap water was then poured onto the porous glass samples to a depth of 10 mm in order to fully immerse the surface. Then, air was pumped into the acrylic box. The inlet allowed air into the cavity below the sample to a maximum gauge pressure of 0.04 bar, measured using an analogue pressure gauge (Wica Instruments Ltd., UK). This recovered the Cassie-Baxter state on the right side of the sample. The absence of reflection of the air pockets in the middle picture can be clearly seen, which is then recovered and shown in the bottom picture.

The effect of applying air pressure to the sample was assessed from the formation of air pockets at the interface. This is visible because of the different refraction indices of air, water and the sample (Daniello et al., 2009).

Images were processed using MATLAB and binarised to black and white. Areas with air at the interface were bright with a silvery appearance as shown in Figure 4.5, whereas areas without air at the interface were dark.

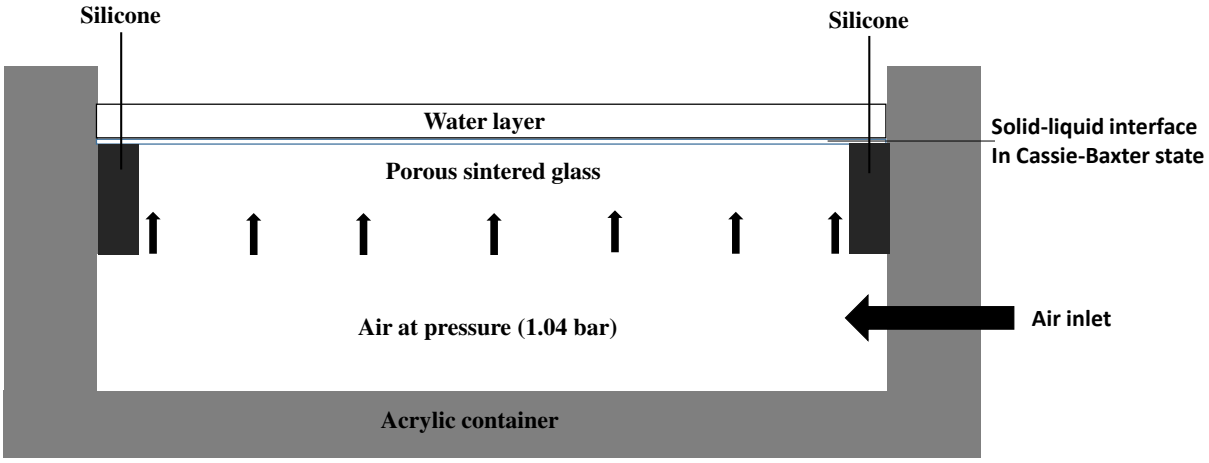

Figure 4.4: Schematic diagram showing the test cell containing the hydrophobic porous sintered glass tile, connected to an air supply to replenish the air pockets on the sample surface.

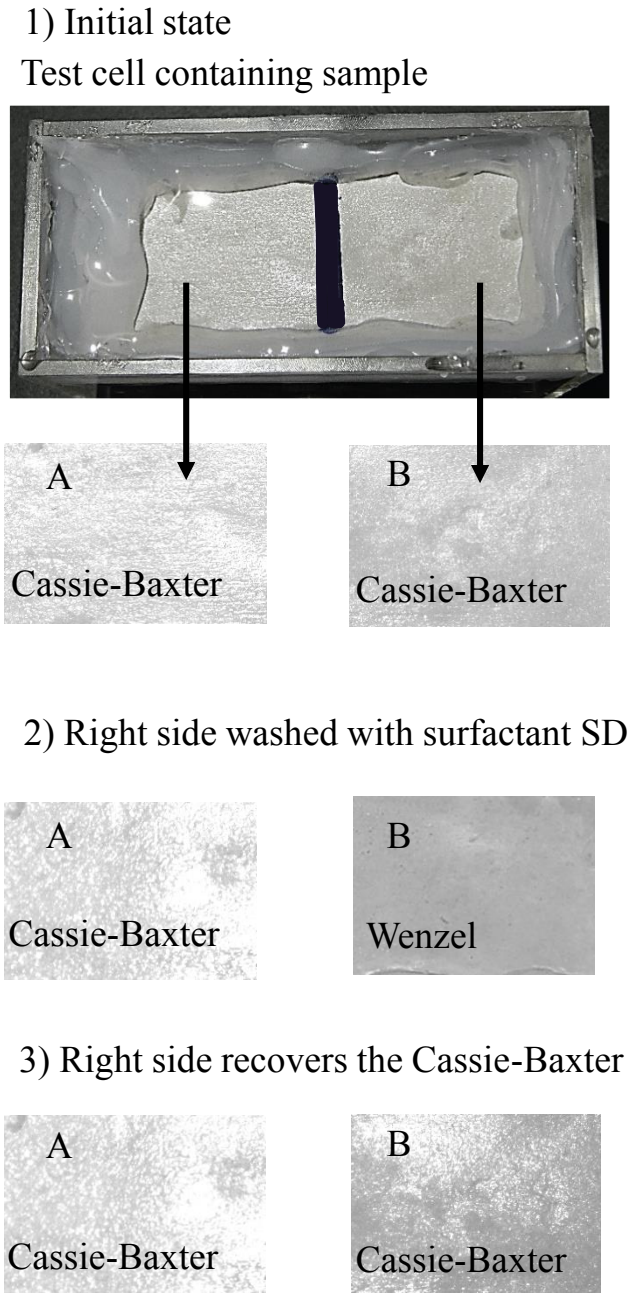

Figure 4.5: Recovery of the Cassie-Baxter state of wetting by recovering the air pockets on the surface of the sample.

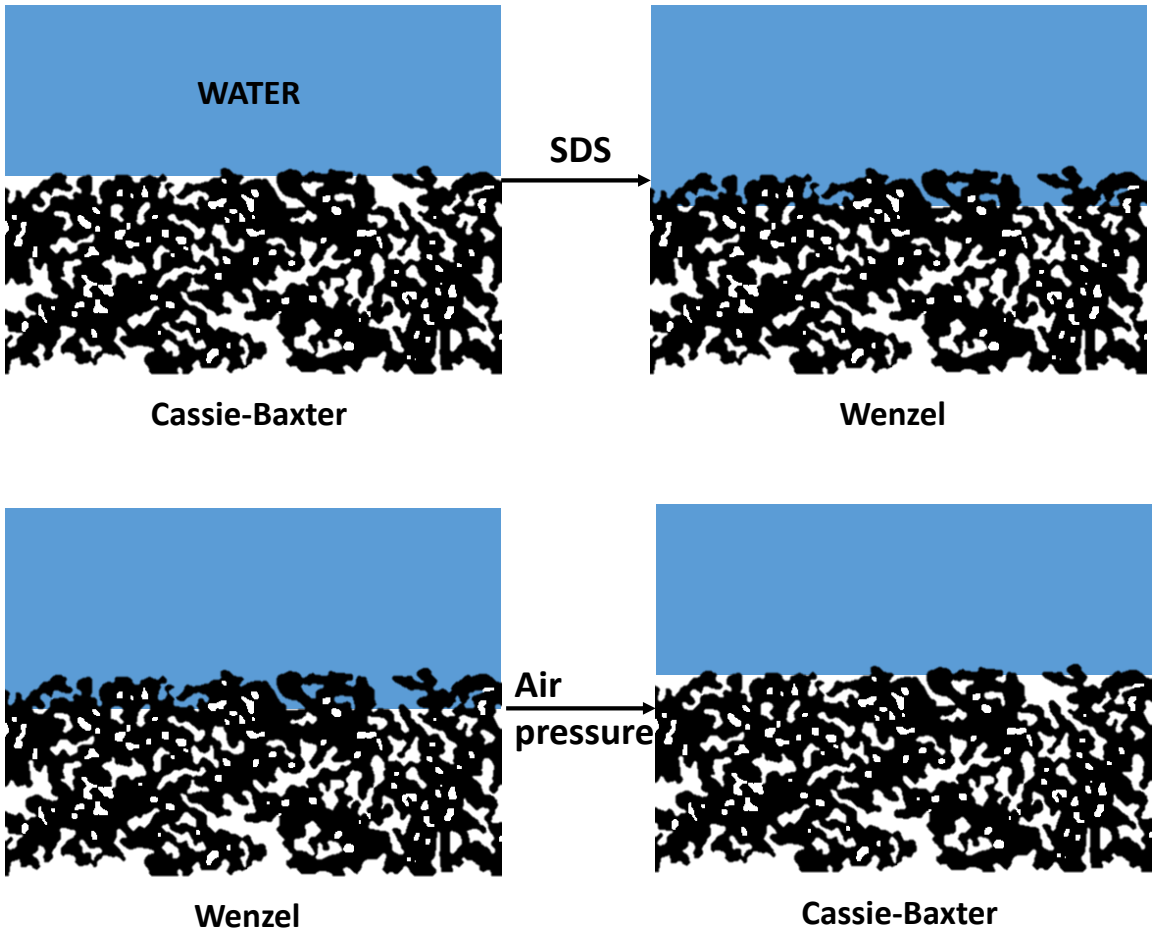

Figure 4.6: Illustration of water infiltration in the pores of the roughened surface by washing with with surfactant solution sodium dodecyl sulphate diluted 1:800 in water, then recovery of the air pockets by applying an air pressure across the material.

4.3 Sample characterisation

On the left side of Figure 4.7, SEM micrographs are shown. The binarised images are on the right side using the standard $\eta_{tr} = 0.5$. The calculated peak ratio using $\eta_{tr} = 0.4$ for samples E, D and ST was 62.8%, 89.3% and 61.1% respectively, and using $\eta_{tr} = 0.6$ the peak area for the samples E, D and ST was 39%, 54.3% and 38% respectively. This method was applied to three different SEM micrographs of each sample and it showed that the percentage of valleys of samples E and ST (d≤45

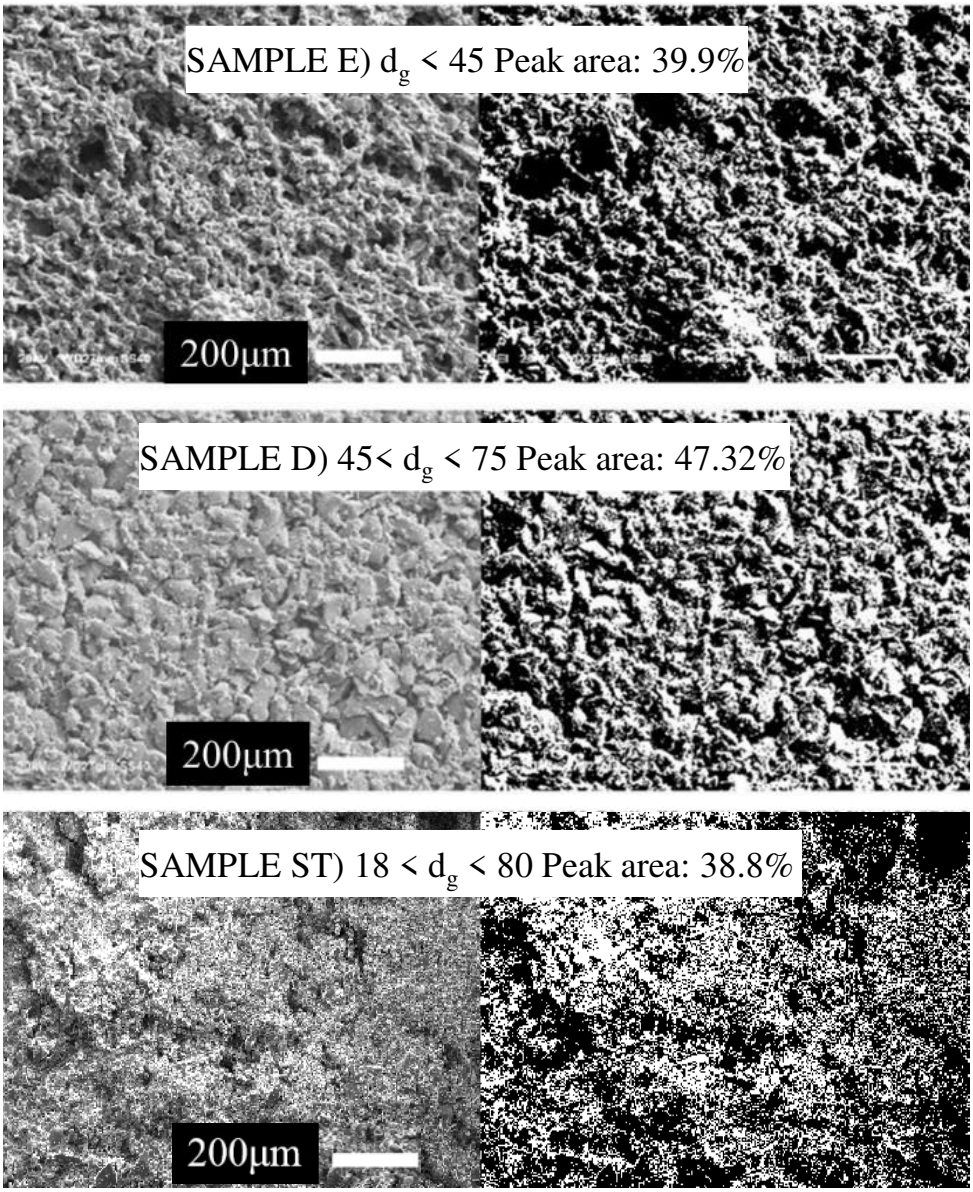

Figure 4.7: SEM micrographs showing surface roughness of samples. On the left side is the SEM micrographs, and on the right is the SEM images at standard threshold level $\eta_{tr} = 0.5$.

μm) were slightly higher than sample D. The surfaces of samples were not perfectly uniform with varying roughness as shown by the x-ray tomography images in Figure 4.8. The roughness of samples E and ST was approximately 70% higher than sample D. This result was expected because samples E and ST were formed with lower particle sizes.

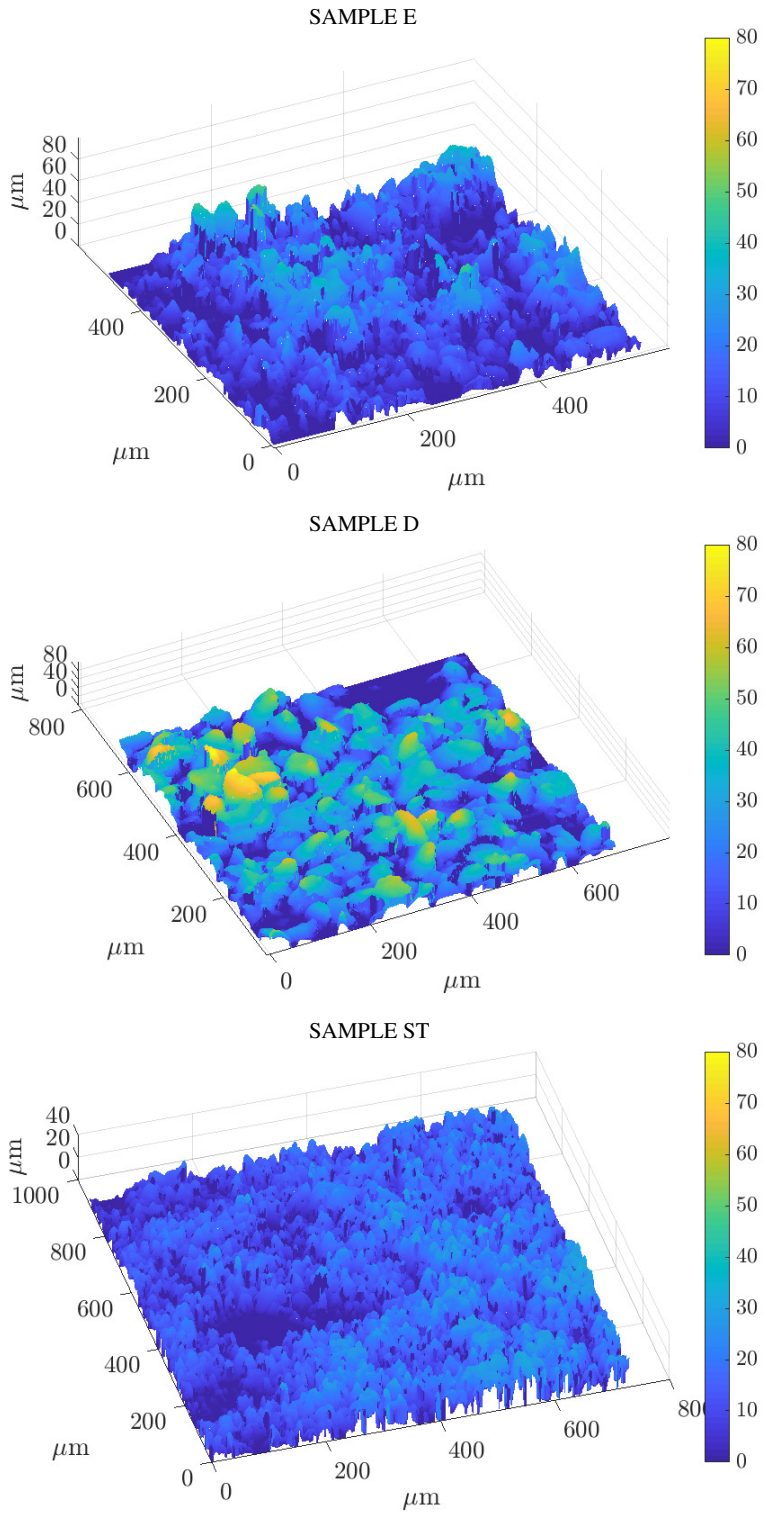

Figure 4.8: X-ray tomography showing surface roughness of samples. This shows that samples E and ST have higher surface roughness than sample D. This has been confirmed by calculating the relative roughness of samples using the triangulation method.

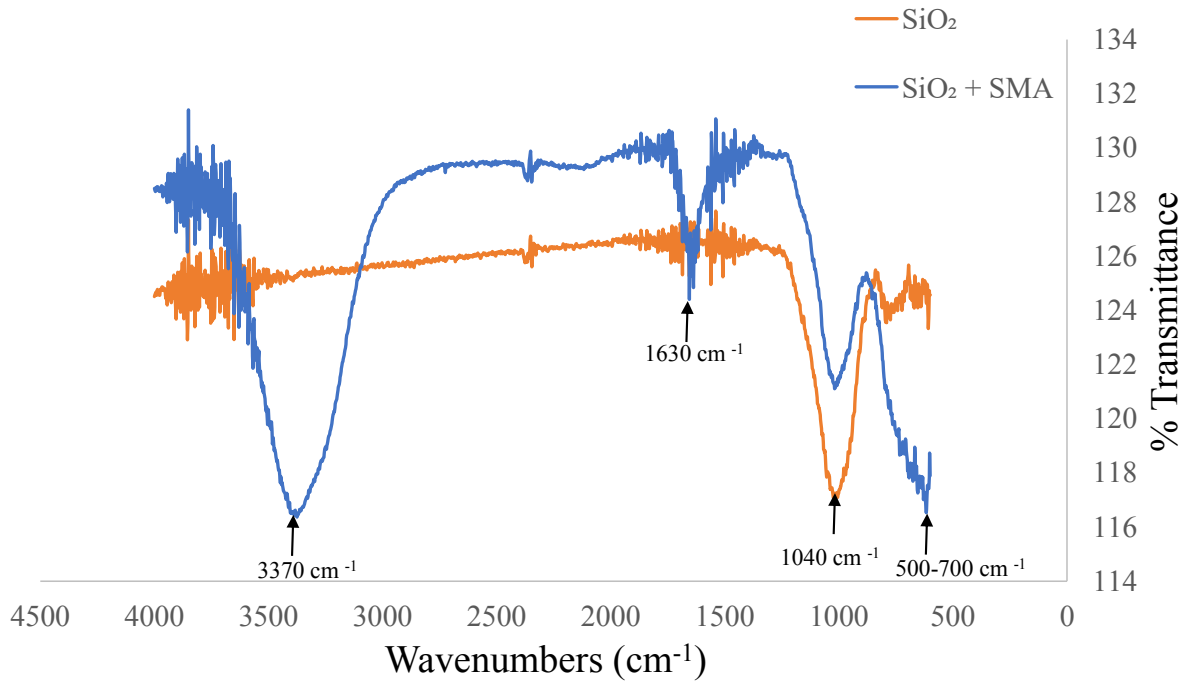

Figure 4.9: FTIR spectra of dry pristine soda-lime glass and dry soda-lime glass samples functionalised with PFTS.

The particle size distribution d_{50} of soda-lime glass powder that formed samples E and ST is (Table 4.1) approximately three times smaller than sample D. Figure 4.9 compares the spectra of dry pristine soda-lime glass and dry soda-lime glass samples functionalised with PFTS.

The change in intensity in the vibration band in the region 1040-1070 cm^{-1} points to the Si-O-Si characteristic peaks, suggesting the successful fluorinated silica coating on the soda-lime glass surface (Lu et al. (2017a)). Vibration bands at 1146-1299 cm^{-1} can be assigned to the asymmetrical and symmetrical stretching of CF_2 (Mihály et al. (2006), Lu et al. (2017a)), as well as in the region 500-700cm^{-1} indicates CF_2 bending and scissoring and CF deformation (Mihály et al. (2006)). A broad absorbance band is shown around 3300 cm^{-1}, characteristic of the OH bond. It is possible that OH bonds formed after immersion of the sample in water from incomplete reaction with PFTS - the Cl atoms attached to Si are substituted by oxygen atoms in the presence

Table 4.1: Composition and physical properties of different porous tile samples reacted with coated with trichloro(1H,1H,2H,2H-perfluorooctyl)silane.

Sample	Particle size dist. (μm)[xx]		Tile porosity (%)[xxi]	Open porosity (%)[xxi]	Mean pore size (μm)[xxi]	Rel. surface roughness[xxi]	Contact angle[xxii] (°)	Recovery of Cassie-Baxter state[xxi]
	d50	d90						
E	23.3	51.5	23.4	99.5	9	2.08	143.7	Yes
D	62.6	103.2	36.3	99.8	15	1.58	149.0	Partially
ST	18.0	80.0	33.7	99.8	8	2.00	153.3	Yes

[xx] Circa 0.5 g of sample was analysed
[xxi] n = 1
[xxii] n = 3

of water, and the Oxygen atoms should form another single bond with a neighbouring Si atom. The FTIR results indicate that it is possible that Cl atoms were substituted by hydroxyls instead of an oxygen with two single bonds attached to Si.

4.4 Recovering the Cassie-Baxter state under immersed conditions

Initial contact angles for different porous glass samples reacted with SMA are shown in Table 4.1. Sample ST had an average contact angle 153°, indicating super-hydrophobicity. Samples E and D had contact angles that varied across the surface with some areas demonstrating super-hydrophobicity. Washing the surface with SDS solution reduced the surface tension of water and the water infiltrated into pores on the surface, removing the air pockets. The wetting state changed from Cassie-Baxter to Wenzel and a water droplet on the surface exhibited complete wetting (contact angle $\leq 10°$).

Figure 4.10 shows the transition from the initial Cassie-Baxter state to Wenzel state after washing, with recovery to the Cassie-Baxter state after air was passed through the sample. All three sintered samples are porous with a high open porosity and consequently high pore connectivity as shown in Table 4.1. This allows the air

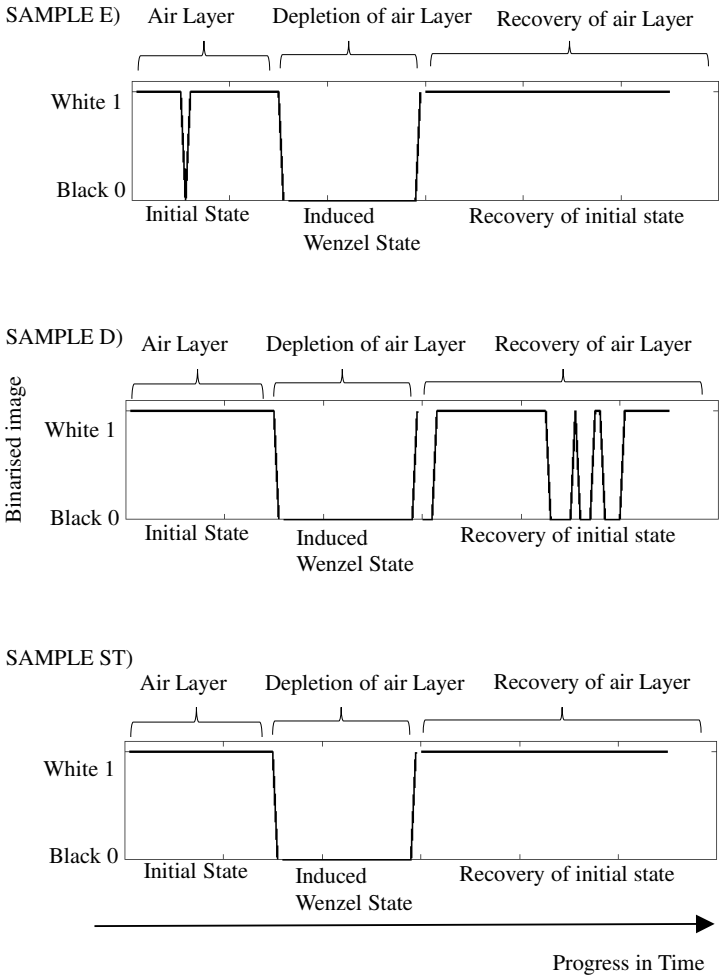

Figure 4.10: Recovery of the Cassie-Baxter state by replenishing the air pockets on the surface of porous glass samples. The samples were tested using the test cell shown in Figure 4.5. The surface was initially in the Cassie-Baxter state. After washing the Wenzel state was induced, hydrophobicity reduced and the air pockets was removed. Covering with water and applying air pressure across the porous material formed air pockets and increased hydrophobicity in samples E and ST, but only partial recovery in sample D.

pockets to be replenished at the surface in all samples. The mean pore size of sample D was approximately 40% larger than samples E and ST. However, the tile porosity (%) between samples D and ST is less than 3 percentage points. The porosity level of samples presented minor influence over the recovery of the air pockets on the surface compared to the relative surface roughness. Surface roughness affects the wetting dynamics of samples in the Cassie-Baxter state - higher relative surface roughness leads to smaller area of contact on the liquid-solid interface (Zheng & Lü, 2014). Moreover, the structure and surface free-energy influences the way air spreads over surfaces in the Cassie-Baxter state (Zhang et al. (2017)).

The formation of bubbles on the surface of the samples was different for each sample, and indicates differences in the level of hydrophobicity among samples. This has been reported by Zhang et al. (2017) by passing CO_2 through porous surfaces of different levels of hydrophobicty, sorted by their water contact angle. In Zhang et al. (2017) various small CO_2 bubbles formed on hydrophilic surfaces, whilst in super-hydrophobic surfaces gas bubbles merged across the surface forming an air film of approximately the size of the surface of the sample, indicating that the diameter of the gas bubbles changes as a function of interfacial roughness and energy. Similar bubble formation occurred in samples D, E and ST and is shown in Figure 4.11. When a gauge air pressure of 0.04 bar was applied across the material in the experiment of recovery of the Cassie-Baxter state, the air that left the surface formed different bubble sizes in each sample. In Figure 4.11 smaller bubbles form on the surface of sample D compared to figures of samples E and ST. Sample D is formed with d_g 75-45 μm and presented lower water contact angles. The formation of smaller bubbles indicate that the water-repelling properties of this surface is lower than of samples E and ST (Zhang et al., 2017).

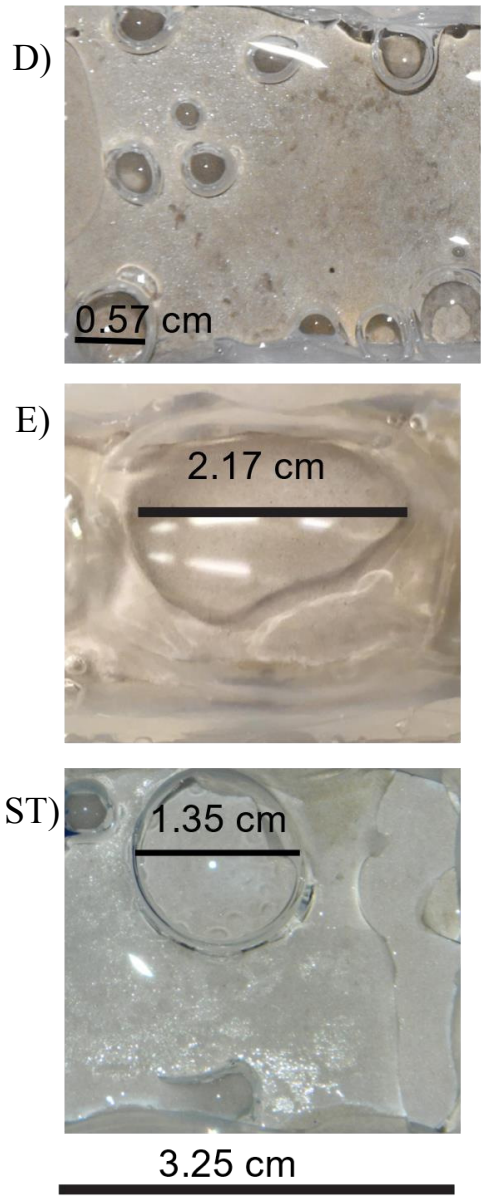

Figure 4.11: Bubble formation and merging in samples D, E and ST. Sample D is formed with d_g 75-45 μm and presented lower water contact angles. The formation of smaller bubbles indicate that the water repellent properties of this surface is lower than of samples E and ST.

4.5 Material behaviour in water containing free chlorine

4.5.1 Disinfection of drinking water using free chlorine

The surfaces produced in this study are intended to be used in water transport systems, and therefore the effects of water containing an oxidising agent on the super-hydrophobic material must be investigated, since these are used for disinfection purposes. Disinfection is the last step carried out in water treatment before transport water to the end user, and is aimed at removing possible pathogens from water by filtration, or inactivating these pathogens by applying a disinfecting agent that could be ultraviolet light, or an oxidising agent such as free chlorine, ammonia (NH_3), ozone (O_3) or chlorine dioxide (ClO_2). Free chlorine refers to both hypochlorous acid (HOCl) and the hypochlorite (ClO^-) ion, that are formed by the addition of sodium hypochlorite (NaClO) in water:

$$NaClO + H_2O \longrightarrow HOCl + NaOH$$

HOCl dissociates in aqueous solution to form ClO^-:

$$HOCl \rightleftharpoons ClO^- + H^+$$

The use of NaOCl to disinfect water and form the oxidising agents HOCl and ClO^- is common. The concentration of HOCl and ClO^- formed from the dissociation of HOCl depends on the pH of the solution, as shown in Figure 4.12.

The HOCl species contributes most to disinfecting water, and is more abundant at a pH range of 2-7, as seen in Figure 4.12 (James P. Farr & Steichen (2000), Staff et al. (2012)). Therefore in water treatment works the optimal pH for disinfection is kept close to neutral between 6.5-7, to provide an efficient water disinfection and drinking

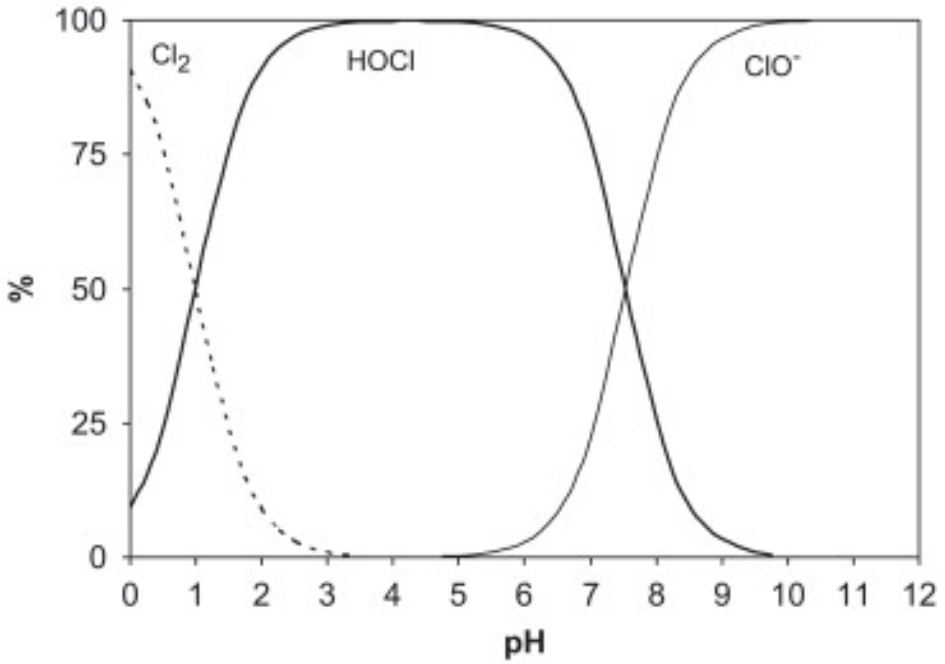

Figure 4.12: Balance of a solution of chlorine, hypochlorous acid and sodium hypochlorite at 25°C (Deborde & von Gunten (2008)).

water at a suitable pH. The concentration of free chlorine dissolved in water decays over time due to reactions with dissolved organic carbon, ammonia, wall reactions among others (Staff et al. (2012)). At the water treatment works, a calculated concentration of NaOCl is added in excess to ensure an optimal residual free chlorine of 0.2 to 0.5 mg/L (WHO (2003)). Even though HOCl is a weak acid, the surface used in this study remains in contact with water for long periods, therefore the possible effects of free chlorine on the super-hydrophobic surface were investigated.

Two experiments were performed to investigate the effects of free chlorine on the super-hydrophobic surface: a) decay of free chlorine over time in a solution with initial free chlorine concentration of 15 mg/L; and b) contact angle of the super-hydrophobic samples before and after immersion in solution with free chlorine.

4.5.2 Materials and methods

Two types of samples were used: super-hydrophobic samples (SH) prepared as in Chapter 3, and sintered hydrophilic samples (PH) before surface modification with PTFS. Free chlorine was obtained by diluting NaOCl in deionised water and measured using the DPD Colorimetric method test Kit (Merck, Germany). More details on the free chlorine measurement procedure are presented in Appendix D. The contact angle was measured using 4-8 μL of deionised water droplets. The difference in droplet volume is due to the low adhesion between the super-hydrophobic surface and water. Due to the low adhesion water droplets do not leave the tip of the polytetrafluoroethylene Drop Shape Analyzer syringe, and in some areas a droplet with higher volume was needed.

Super-hydrophobic samples were placed in a strong NaOCl oxidising solution to analyse the possible oxidising effects of NaOCl on the surface. The possible effects were quantified by measuring the decay of free chlorine over time, and by changes in the water contact angle of the surface. Possible reactions with NaOCl were monitored by the decay of free chlorine, by placing samples of surface area 1, 5 and 10 cm^2 in beakers containing 100 mL of a solution containing 15 mg/L free chlorine and stirred using a magnetic stirrer for the duration of the experiment. The high free chlorine dosage was used to ensure any possible reaction with the surface would occur, if any.

Free chlorine was measured using the DPD Colorimetric method. The DPD Colorimetric method utilised in this study is widely applied in water quality control. N,N-diethyl-p-phenylenediamine(DPD) is used as an indicator in the titrimetric procedure. The free chlorine compounds formed when NaOCl is diluted in water oxidise the colourless DPD, forming a magenta-coloured compound. The intensity of the colour indicates the concentration of free chlorine in the solution. Aliquots of 10 mL were taken at beginning of the experiment, then at 15, 30, 60, 120, 180 and 1200 minutes and used in the DPD reaction. The experimental procedure is described in Appendix D.

Table 4.2: Contact angles before and after immersion for 1200 minutes at pH 6.5 in sodium hypochlorite 15 mg/L solution.

Sample size (cm^2)	Contact Angle (°) Before	After
1	156.0 ± 5.1	161.6 ± 2.7
5	156.5 ± 2.9	159.5 ± 3.9
10	157.8 ± 3.9	160.3 ± 2.2

The contact angle was measured prior to immersion in NaOCl solution and after. A Drop Shape Analyzer using ADVANCE software (DSA30, KRÜSS GmbH, Hamburg, Germany) was used to measure the contact angle of 4-8 μL water droplets in at least 10 locations of each sample.

4.5.3 Measured contact angle of samples and free chlorine decay

The mean value of water contact angles before and after immersion in NaOCl solution is presented in Table 4.2. A minimum of 20 water contact angle measurements were taken for each sample. Two tailed t-tests were conducted and are presented in Appendix C. The t-test was performed for this experiment to investigate whether there was a significant difference between contact angle values before and after immersion in NaOCl solution. The results shown in Appendix C indicate with 95% confidence that there was no significant difference between contact angle values before and after immersion in NaOCl solution.

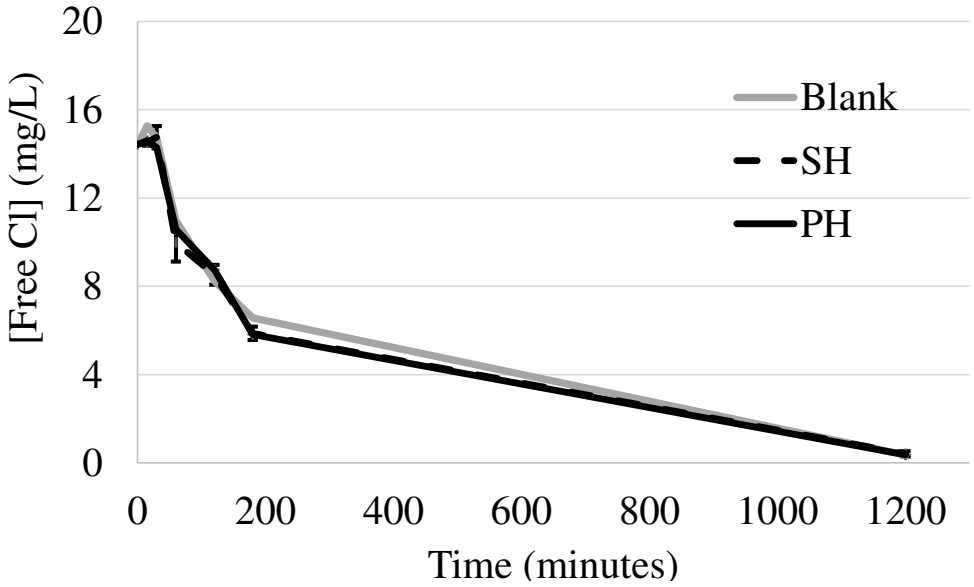

Figure 4.13: Decay of free chlorine over time. Super-hydrophobic (SH), hydrophilic (PH, samples before surface modification) and blank show similar free chlorine concentration decay.

The decay in free chlorine is presented in Figure 4.13, showing the blank (solution without super-hydrophobic sample), and the averaged results of super-hydrophobic and hydrophilic samples. The trend in free chlorine decay shown in Figure 4.13 show similar decay of HOCl and $^{-}$OCl species. The decay in free chlorine and results of student's t-test suggest that there is no reaction between free chlorine and the super-hydrophobic material, indicating that the super-hydrophobic material produced in this research is potentially safe to use in drinking water pipes.

4.6 Conclusions

In this Chapter the performance of three surfaces in the Cassie-Baxter state were quantified by their water contact angle, bubble formation on the surface and recovery of the air pockets by exposing the samples to static water to a depth of 10 mm and applying an air pressure of 0.04 bar. The application of air pressure gradient across the sample replenishes the air pockets at the liquid-solid interface allowing the

Cassie-Baxter state to be recovered. Results showed higher recovery for sample ST. To evaluate the new material as a drinking water pipe, the effects of free chlorine on the super-hydrophobic surface ST was investigated by measuring the concentration of free chlorine over time and the changes in contact angle of the material. The decay in free chlorine over time and measurements of water contact of the material before and after exposure to a high concentration of free chlorine suggest that there is no reaction between free chlorine and the super-hydrophobic material.

The results described in this Chapter form are important steps toward the objectives set in this dissertation: to manufacturing a surface able to maintain/recover the Cassie-Baxter state of wetting under fully immersed conditions for use in the water distribution systems. To investigate the use of sample ST for water transporting applications, further investigation is needed such as performance of the surface under turbulent conditions. Therefore, an experimental apparatus has been designed to measure the friction factor of the super-hydrophobic surface of sample ST under turbulent conditions in Chapter 5 and the performance and durability of the sample is investigated in Chapter 6.

5

Designing an experimental apparatus for quantifying drag and durability

This chapter presents the design of a new experimental set-up capable of measuring the friction factor of the super-hydrophobic sample produced in chapter 3 (sample ST) under turbulent flow conditions. The design of the experimental set-up was a critical step to fulfil Objectives 3 and 4 of this thesis. The sections presented in this chapters focus on: 1) a numerical simulation of water flow in a duct containing a super-hydrophobic top wall, used to determine the limitations to the dimensions of the experimental apparatus; and 2) the design and assembly of the experimental apparatus. Moreover, this chapter presents an estimation of accuracy of measurements of the piezometric height and volume flux, that were used to determine the friction factor.

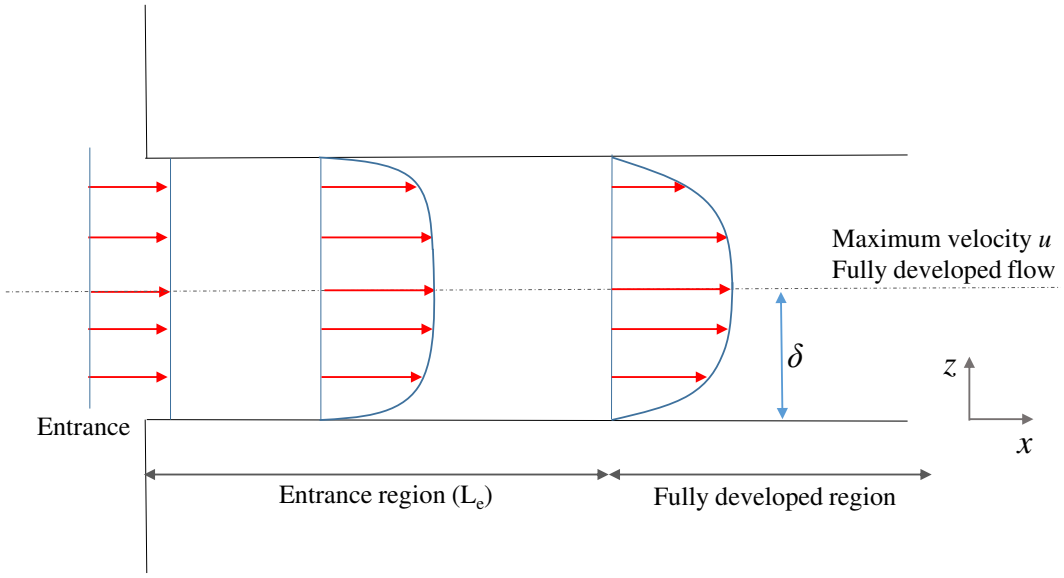

Figure 5.1: Illustration of entrance effects in a plane channel flow

5.1 Determination of entrance length

Entrance effects, which will contaminate accurate friction factor measurements, are estimated in this section by using a numerical model to determine the entrance length L_e for a smooth surface and a surface with partial slip. Here, the entrance length is defined as the length measured from entrance of the duct required for the flow to become fully developed. In the entrance region the flow enters the pipe uniformly. As the fluid gets in contact with the surface of interest, the flow profile changes due to friction between the material of the surface and the fluid. In a no-slip condition the velocity at the wall reduces until it is zero. Figure 5.1 shows the development of the flow profile at the entrance of a pipe.

5.1.1 Governing equations

The motion of a viscous incompressible flow is described by the Navier-Stokes equation:

$$\rho\Big(\frac{\partial \mathbf{u}}{\partial t} + \mathbf{u}\cdot\nabla\mathbf{u}\Big) = -\nabla\tilde{p} - \rho g\mathbf{e}_z + \mu\nabla^2\mathbf{u} \tag{5.1}$$

$$\nabla\cdot\mathbf{u} = 0 \tag{5.2}$$

where x, y and z denote the streamwise, spanwise and vertical direction respectively.

Reynolds-averaging (denoted by an overline) the equations above, assuming homogeneity in y and using that $\overline{v} = 0$, the 2D Reynolds-averaged Navier-Stokes equations are obtained:

$$\overline{u}\frac{\partial\overline{u}}{\partial x} + \overline{w}\frac{\partial\overline{u}}{\partial z} + \frac{\partial\overline{u'u'}}{\partial x} + \frac{\partial\overline{w'u'}}{\partial z} = -\frac{\partial\overline{p}}{\partial x} + \nu\Big(\frac{\partial^2\overline{u}}{\partial x^2} + \frac{\partial^2\overline{u}}{\partial z^2}\Big) \tag{5.3}$$

$$\overline{u}\frac{\partial\overline{w}}{\partial x} + \overline{w}\frac{\partial\overline{w}}{\partial z} + \frac{\partial\overline{u'w'}}{\partial x} + \frac{\partial\overline{w'w'}}{\partial z} = -\frac{\partial\overline{p}}{\partial z} + \nu\Big(\frac{\partial^2\overline{w}}{\partial x^2} + \frac{\partial^2\overline{w}}{\partial z^2}\Big) \tag{5.4}$$

$$\frac{\partial\overline{u}}{\partial x} + \frac{\partial\overline{w}}{\partial z} = 0 \tag{5.5}$$

where we have introduced the modified kinematic pressure $p = \tilde{p}/\rho + gz$ and the kinematic viscosity $\nu = \mu/\rho$.

The crucial assumptions made to simplify these equations are following:

- Streamwise advection dominates in the streamwise momentum equation. This implies that $\overline{u}\partial\overline{u}/\partial x \gg \overline{w}\partial\overline{u}/\partial z$ and $\overline{u}\partial\overline{u}/\partial x \gg \nu\partial^2\overline{u}/\partial z^2$.
- the vertical momentum balance is dynamically unimportant and will be modelled as if it were a fully developed channel flow. Under these conditions, all x-derivatives are zero, which then implies that $\overline{p} + \overline{w'w'} = P(x)$; that is, the total pressure does not depend on z and only on x.

Eliminating the pressure from the streamwise momentum equation, assuming that

$\overline{w'w'} - \overline{u'u'} \ll P(x)$, invoking the gradient diffusion hypothesis $\overline{w'u'} = -\nu_T \partial\overline{u}/\partial x$ and introducing $F = -\mathrm{d}P/\mathrm{d}x$ as the pressure gradient forcing, we obtain

$$\overline{u}\frac{\partial \overline{u}}{\partial x} = F(x) + (\nu + \nu_T)\frac{\partial^2 \overline{u}}{\partial z^2} \tag{5.6}$$

$$\frac{\partial \overline{u}}{\partial x} + \frac{\partial \overline{w}}{\partial z} = 0 \tag{5.7}$$

Volume conservation in equation (5.7) is enforced via the body force $F(x)$, which is discussed in appendix E. These equations need to be augmented by the following initial and boundary conditions:

$$u(0, z) = U \tag{5.8}$$

$$\frac{\partial u}{\partial z}(x, 0) = \frac{u(x, 0)}{\ell_s} \tag{5.9}$$

$$\frac{\partial u}{\partial z}(x, \delta) = 0 \tag{5.10}$$

The turbulence was modelled by applying the Prandtl mixing length theory (Schlichting & Gersten, 2017), i.e. ν_t is approximated as

$$\nu_t = l_m^2 \left|\frac{\partial u}{\partial z}\right| \tag{5.11}$$

where l_m is the mixing length. The Prandtl mixing length model is one of the simplest turbulence closures, and cannot be used in complex flows, e.g. with separation. However, in this simple flow, it can be expected to work reasonably well. The mixing length l_m is modelled by using the Van Driest closure:

$$l_m^+ = K z^+ \left(1 - \exp\left(\frac{-z^+ u_*}{A\nu}\right)\right), \quad A = 25, \tag{5.12}$$

where ν is the kinematic viscosity of water, u_* is the shear velocity close to the wall: $u_* = \sqrt{\tau_w/\rho}$, ρ the density of water and τ_w is the wall shear stress $\mu \frac{du}{dz}|_{z=0}$. Plus units denote normalising as $z^+ = z u_*/\nu$.

A typical value of van Kármán constant $K = 0.4$ is applied in this study. The van Driest mixing length model is a turbulence model that provides a good estimation of the velocity profile in the viscous sublayer and the buffer layer. With this model it is possible to produce accurate estimates of the turbulent viscosity ν_t (Lari et al., 2010).

The boundary conditions implemented to estimate the effects of slip on flow are presented in the following sections 5.1.2 and 5.1.3. The entrance effects of water flow in a duct were conducted to estimate the design parameters for the experimental work.

5.1.2 Semi-discretization of the momentum equation

The values of u are resolved as a function of x ($\frac{d\mathbf{u}}{dx} = \mathbf{f}(x, \mathbf{u})$) using MATLAB ordinary Differential Equation solver ODE45, where x was applied as the vector specifying the interval of integration to estimate the entrance effects, which are further used to estimate the entrance length when super-hydrophobic surfaces with slip are implemented. The momentum equation was discretised in z in a Cartesian coordinate system with a staggered grid-arrangement (Figure 5.2) using the method of lines (MoL) resulting in:

$$\left.\frac{\partial u}{\partial x}\right|_{z_k} = \frac{(\nu + \nu_{t,k+1})\frac{u_{k+1}-u_k}{\Delta z_{k+1/2}} - (\nu + \nu_{t,jk})\frac{u_k-u_{k-1}}{\Delta z_{k-1/2}}}{2u_k \Delta z_k} + F \tag{5.13}$$

In this simulation a grid was created for the velocity of the flow changes in the channel according to vertical and horizontal points. The grid shown in figure 5.2 shows the vertical points z, the velocity u and turbulent viscosity ν_t.

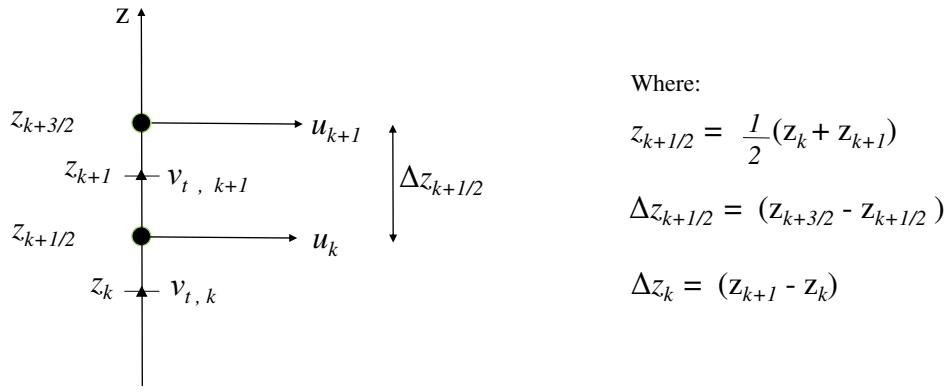

Figure 5.2: Grid of vertical points

5.1.3 Boundary conditions

To estimate the changes in wall shear stress using a surface with Cassie-Baxter state, a boundary condition with slip length ℓ_s was implemented. Values of slip velocity u_w and slip length vary with experimental conditions, and affect directly the entrance length L_e of the flow. The average discrete velocity at the wall is estimated to determine the boundary condition:

$$u_w \approx \frac{u_2 + u_1}{2} \tag{5.14}$$

As seen in Figure 1.10 the slip length is a prolongation distance to the wall that meets the tangential line from the velocity. If the velocity line is extrapolated then the prolonged velocity of the fluid beyond the wall is $\neq 0$ as well. The addition of this variable enables the velocity at the wall to be either zero (no slip, $u_w = 0$) and non-zero ($u_w > 0$). Figure 5.3 illustrates the theoretical velocity profile at the wall.

Taking Navier's slip equation (1.15) and applying u_w estimated in equation (5.1.3) results in:

$$\frac{1}{2}(u_2 + u_1) = \ell_s \frac{u_2 - u_1}{\Delta z} \tag{5.15}$$

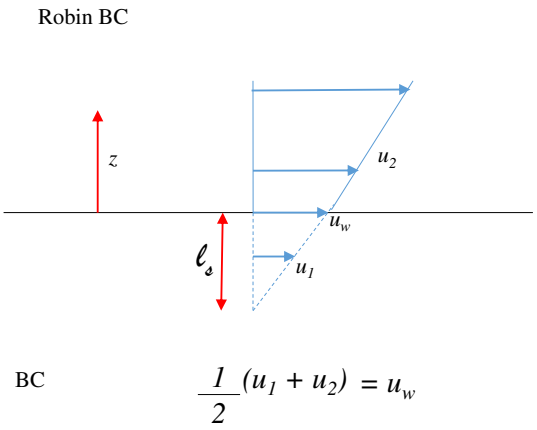

Figure 5.3: Velocities at extrapolated lines in a super-hydrophobic surface

The equation above can be differentiated to x to determine the boundary condition at the wall:

$$\left.\frac{du}{dx}\right|_1 = \frac{2\ell_s - \Delta z_k}{2\ell_s + \Delta z_k}\left.\frac{du}{dx}\right|_2 \tag{5.16}$$

The boundary condition at half channel height $z = \delta$, $\left.\frac{\partial u}{\partial z}\right|_h = 0$, can be obtained in a similar manner and is given by:

$$\left.\frac{du}{dx}\right|_{N+1} = \left.\frac{du}{dx}\right|_N \tag{5.17}$$

For a no slip condition $\ell_s = 0$, $\left.\frac{du}{dx}\right|_1 = -\left.\frac{du}{dx}\right|_2$; that is, the extrapolated velocity beyond the wall is negative. The gradient $\frac{du}{dx}$ is solved along the plane z between the solid-liquid boundary and half duct height δ. Three functions were used for solving $\frac{du}{dx}$ along z: (1) at the solid-liquid interface using a mixed boundary condition (Robin), (2) between the solid-liquid boundary and half duct height δ solved using the momentum equation, and (3) at the boundary at δ using an imposed gradient of $\frac{du}{dx}$ (Neumann). The resulting initial value problem $\frac{du}{dx} = f(x, u)$ was solved in

MATLAB using ODE45, where f is given by:

$$\mathbf{f}(x,\mathbf{u}) = \begin{cases} \left.\frac{2\ell_s-\Delta z_k}{2\ell_s+\Delta z_k}\frac{du}{dx}\right|_1 & k=0 \\ \frac{\nu_{t,k+1}\frac{u_{k+1}-u_k}{\Delta z_{k+1/2}}-\nu_{t,jk}\frac{u_k-u_{k-1}}{\Delta z_{k-1/2}}}{2u\Delta z_k}+\frac{F}{2u} & k\in[1,2,...N] \\ \left.\frac{du}{dx}\right|_N & k=N+1 \end{cases}$$

5.1.4 Estimating minimum experimental requirements

Table 5.1 shows the parameters used in the simulation to estimate values of τ_w among others between a smooth and super-hydrophobic surface, considering other design parameters previously selected. The wall shear stress τ_w was calculated using equation 1.12 from the estimates of velocity gradient du/dz close to the wall. The minimum length of the experiment was obtained by estimating the length at which τ_w becomes 90 to 95% of its final value. The lengths in metres were estimated for channel heights (δ) of 0.01 to 0.1 m and velocities of 1 and 1.5 m/s. The results are presented in Table 5.2, and in Figure 5.4.

Figure 5.4 shows the predicted wall shear stress along x. The values of τ_w were calculated based on a flow velocity of 1.5 m/s, and will be adjusted as the real

Table 5.1: Parameters implemented to estimate the values of wall shear stress, length of viscous sub-layer and others between a smooth and super-hydrophobic surface

Parameter	**Value**
Water depth (δ)	0.01 to 0.1 (m)
Kinematic viscosity (ν)	10^{-6} (m^2/s)
Mean velocity (u)	0.5 to 2 (m/s)
Integration interval	100 δ
Number of vertical grid points (z)	200
Dynamic viscosity (μ)	10^{-3} (N s/m^2)

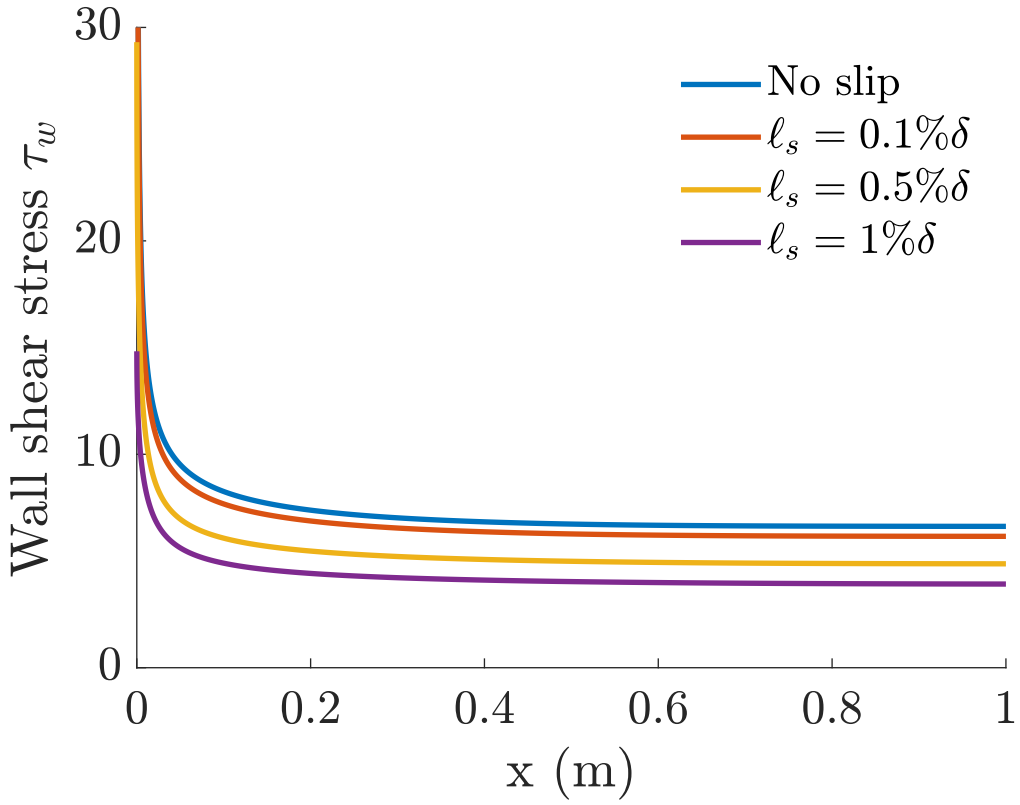

Figure 5.4: Development of shear stress for surfaces of slip length (ℓ) 0 to 1% (1×10^{-4} m) of the channel height (1×10^{-2} m).

values of flow velocity are obtained from experimental results. In the calculations using various slip lengths, τ_w is presented for a constant velocity. However, it is expected that the velocity for surfaces in the Cassie-Baxter state will be slightly higher than for the ones in the Wenzel state. The development of wall shear stress τ_w in Figure 5.4 occurs mostly on the first 0.2 m from the entrance, showing little variation between 0.3-1.0 m, which results in uniform values of f_d from $x = 0.3$ m since changes in τ_w affect f_d directly as shown previously in equation (1.9). It can be seen in Figure 5.4 that higher values of ℓ_s result in longer entrance lengths for τ_w to become steady. Fortunately studies have shown values of ℓ_s of approximately 1% δ. Therefore measurements of f_d can be taken from approximately $x = 0.3$ m from the entrance of the duct.

It can be seen from table 5.2 that for a duct with half channel height $\delta \geq 0.05$ m the minimum length required for τ_w to attain at least 90% of its developed flow rate

Table 5.2: Lengths for flow to develop

Wall shear stress (τ_w)	Velocity (m/s)	Channel height δ (m)	ℓ_s			
			0	1% δ	5% δ	10% δ
			x(m)			
90%	1.5	0.1	2.533	2.533	2.499	2.431
	1		2.482	2.482	2.482	2.448
95%	1.5		3.942	3.995	4.049	4.077
	1		3.862	3.862	3.942	3.995
90%	1.5	0.05	1.224	1.224	1.224	1.199
	1		1.191	1.199	1.207	1.199
95%	1.5		1.880	1.905	1.971	1.998
	1		1.829	1.842	1.905	1.944
90%	1.5	0.01	0.219	0.224	0.235	0.243
	1		0.215	0.218	0.230	0.243
95%	1.5		0.328	0.337	0.363	0.386
	1		0.317	0.324	0.349	0.373

is $x \geq$1.2 m for all slip cases. This would require an experimental apparatus of at least 1.5 m considering the minimum developing length of $x = 1.2$ m and 0.3 m total distance between three piezometric tubes placed along the duct for measurements of the pressure head h. Therefore a half channel $\delta = 0.01$ m is more suitable for this research because the minimum developing length (considering 90% developed shear stress) is approximately 0.215 m for a no-slip condition. That is, piezometric tubes could be placed at approximately 0.215 m from the entrance of the duct to take stable measurements of the pressure head. For flows on surfaces with slip conditions the development of the shear stress occurs at longer distances and increases with increasing slip, as shown in Table 5.2. Taking into consideration that previous studies found values of ℓ_s to be approximately 1% δ, piezometric tubes used in the estimation of head loss should be placed from 0.337 m from the entrance of the duct.

5.1.5 Expected roughness Reynolds number

In this section the predicted values of the thickness of the viscous sub layer are presented and compared with the values of surface roughness ε. The viscous sublayer δ_* corresponds to 5 wall units (y^+), $\delta_* = 5\ y^+$. The thickness of δ_* is estimated by: 5 $y^+ = y\ u_*/\nu$, for flow of velocity 1, 1.5 and 2.0 m/s calculated using the parameters shown in Table 5.1. Estimated roughness ε (local maxima) values of 30, 50 and 100 μm were applied because 50 μm corresponds to the maximum ε obtained with X-ray tomography data for sample made with d$\leq$ 75μm (see Chapter 3). The plots below show in terms of roughness Reynolds number $Re_s = \varepsilon u_t/\nu$ that for certain cases the roughness of the super-hydrophobic surface is higher than the height of the viscous sub-layer. Values of $Re_s \leq 5$ are considered hydraulic smooth, $5 < Re_s < 70$ are transitional and $Re_s > 70$ are considered rough. Surface roughness can have substantial effects on the turbulent layer, and cause drag to increase when the roughness of the surface if higher than the viscous sub-layer (Daniello et al., 2009, Colebrook & White, 1937).

5.2 Determination of required measurement accuracy

Previous methods to estimate the friction factor f_d of surfaces were analysed (Walker et al., 2016, Yao et al., 2015, Fuaad et al., 2016, Colebrook & White, 1937, Daniello et al., 2009, Rahman et al., 2013a). The parameters used to quantify wall friction and drag reduction are diverse and have been summarised in Table 5.1. Significant changes fluid velocity or wall friction have been reported in simple experimental designs (Walker et al., 2016), and parameters such as slip velocity and length are often obtained through methods such as Particle Image Velocimetry (PIV). The method used in this research consists of measuring the friction factor of a super-hydrophobic surface over time because as previously shown, the super-hydrophobic effects decrease with constant water contact. A schematic figure of the set-up is

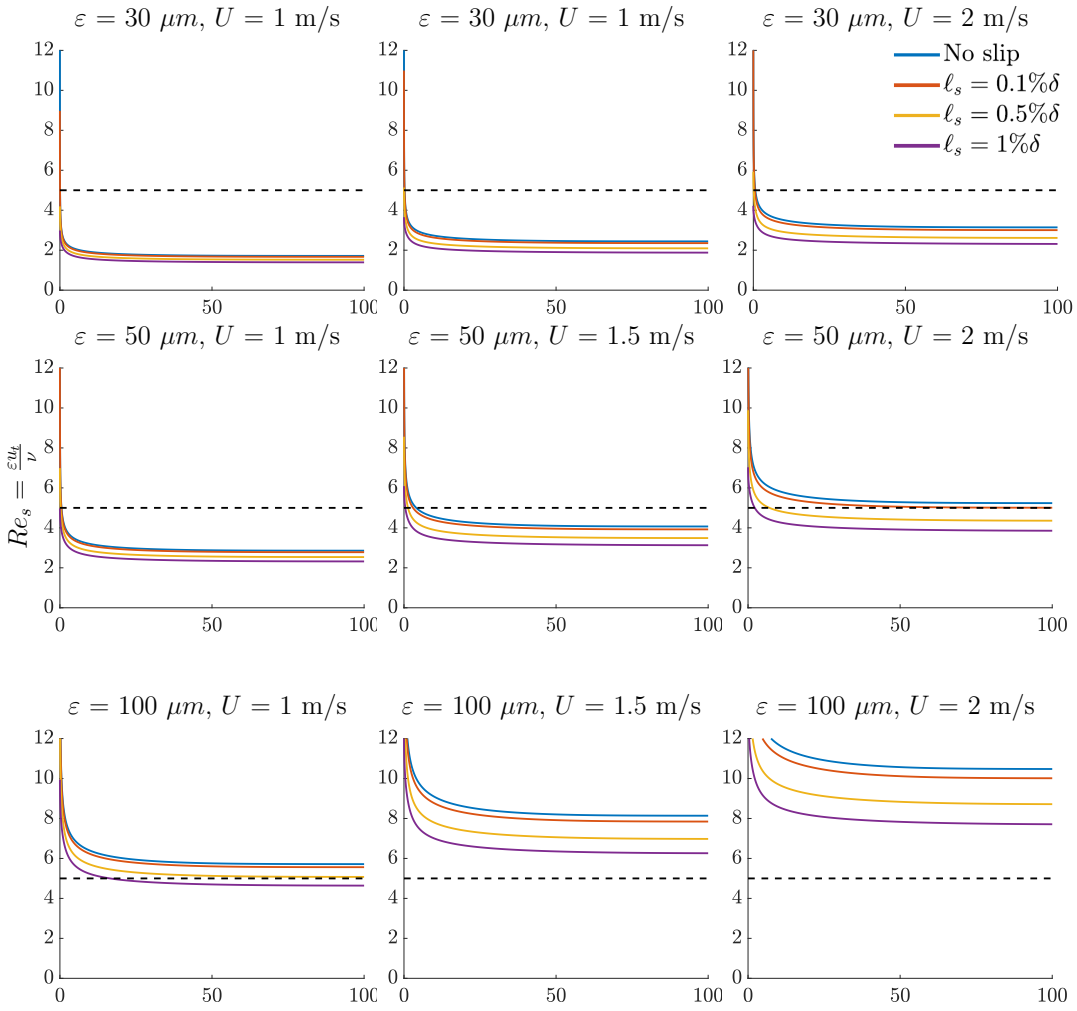

Figure 5.5: Estimation of roughness Reynolds number at three different velocities and slip conditions.

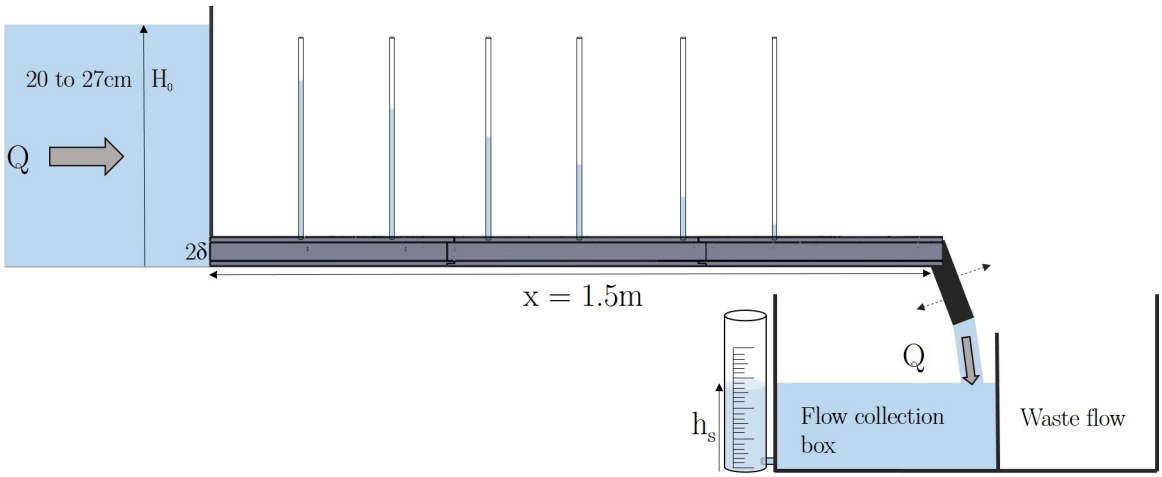

Figure 5.6: Schematic figure of experimental set-up. Water flows at a flow rate Q that is dependent on the initial head H_0. At the outlet the water flow can be directed to the collection or waste tank. In the collection tank level to which water rises (h_s is measured to obtain the volume of water (V) over a time period t ($Q = Vt$).

shown in Figure 5.6. The friction factor of the super-hydrophobic porous material will be measured by transporting water in a duct consisting of:

1 Side and bottom walls made of acrylic (purchased from Perspex Distribution Ltd., England)

2 Top wall made of super-hydrophobic porous surface

The inner dimensions of the duct in contact with water are 2 cm (height, 2δ) $\times$ 7 cm (width) $\times$ 150 cm (length, x). Values of half channel height and experiment length were selected following the results of entrance effects in section 5.1.4. The equipment was placed in a flume in the hydrodynamics laboratory located in the Civil Engineering Department at Imperial College London (ICL). The flume is used as a source of water to the duct, of maximum water height of 30 cm. The water is collected in a tank of area (A_t) $A_t = 0.894$ m^2, shown in Figure 5.7.

The wall friction reduction using the proposed experimental set-up is calculated using volume flux (Q) and head loss measurements (Δh). Previous studies estimated the friction factor difference between pipes made entirely with smooth (f_B) or super-hydrophobic surfaces (f_d) (Walker et al., 2016, Shirtcliffe et al., 2009, Rahman et al.,

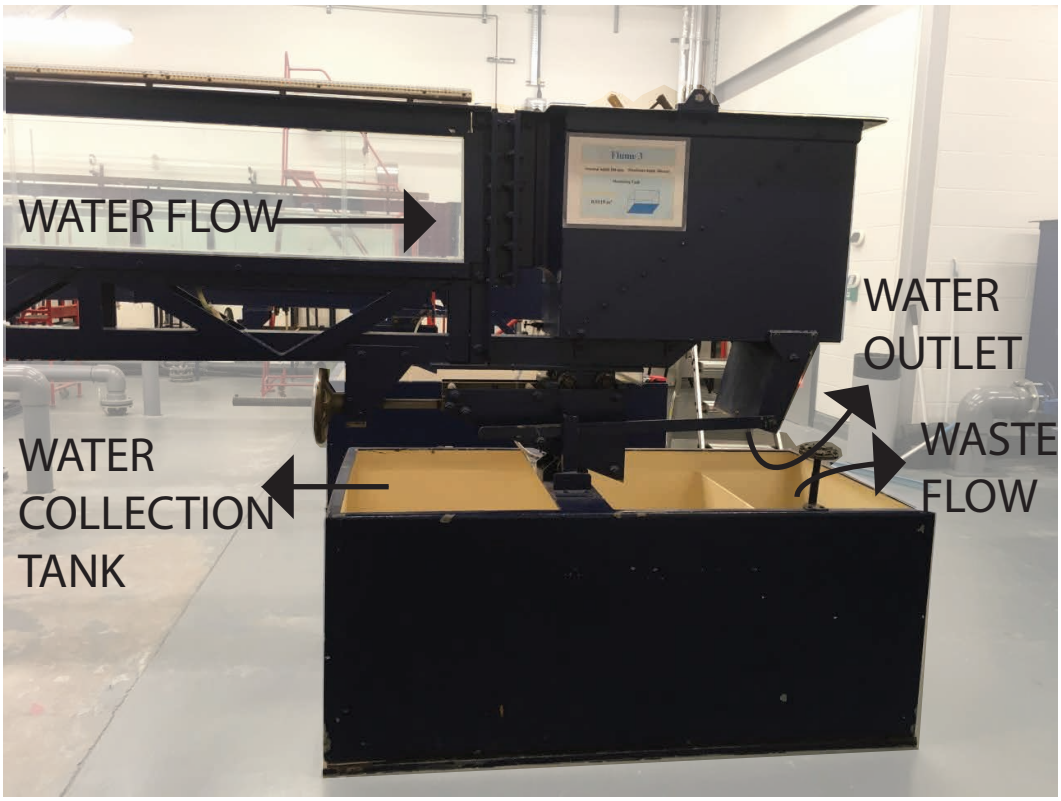

Figure 5.7: Water tank for collection of water that flows in the channel.

2013b). For smooth surface the friction factor is given by the Blasius equation (Nakayama, 2018):

$$f_B = \frac{0.316}{Re^{0.25}} \tag{5.18}$$

In this study two configurations of a duct were used: a) all four sides were made of acrylic walls; and b) three sides are made of acrylic walls and the top layer was composed of super-hydrophobic surfaces produced as shown in chapter 3. The duct was designed with four sides, of which only the top layer is detachable. To determine the friction factor for the top surface alone, it was assumed that the friction factor of all acrylic surfaces (sides and bottom) is given by (5.18), which leads to:

$$f_d = \frac{\overline{f}_d P - f_B(P - w)}{w}. \tag{5.19}$$

where P is the perimeter of the duct w is the width of the super-hydrophobic surface. The measured quantities of Q and Δh for the two configurations are subjected to systematic and random error. In light of this two questions will need to be answered:

1 What is the required accuracy of Q to determine f_d within 5%?

2 Will the difference in Q and Δh within each experimental set be higher than the estimated systematic and random errors?

In the eventuality that measured errors are larger than the difference in wall friction between a smooth and super-hydrophobic surface, the results would be considered insignificant. For instance, in the proposed set-up, water flows in a duct containing one super-hydrophobic top layer, and the volume of water is collected in a tank of $A_t = 0.894$ m^2, therefore every millimetre of water height corresponds to 0.894 L. Similarly, if the velocity of the water flow is 1.5 m/s, and opening/shutting down the water flow takes $\pm$ 1 second, the error is equivalent to 2.1 L. Therefore, a sensitivity

study is needed with the purpose of estimating the maximum error for measurements, to obtain significant results. The primary source of errors in this study are:

1 Reading error (h): up to 1mm;

2 Shutting down source of water flow at a given time (dQ): up to 1 second.

Super-hydrophobic surfaces have been reported to have a friction factor of f_d = 0.016-0.024 (Daniello et al., 2009, Walker et al., 2016). The difference in wall friction in studies with Re>4,000 is approximately df_d = 0.008-0.016. If a realistic scenario where df_d = 0.008 is considered, and a pessimistic (df_d = 0.004) and optimistic (df_d = 0.016) scenario, measurement errors may not exceed df_d = 0.004 for the results to be significant. The two main sources of errors are described above. Reading error is the error when obtaining the water height elevation of the water flow collected in a tank. These errors can be minimised by reducing the area of the collection tank and increasing the time of collecting the water flow. However, there are two limitations on the following: a) the tank cannot be replaced/removed; and b) the collection time is limited by the volume of the tank. Although these limiting parameters affect the sensitivity of the method, it is still possible to obtain significant results if a significant minimum collection time is established and feasible. The required accuracy of a measured volume flux (Q) and head loss (Δh) are calculated. A volume V ($V = Qt$, where t is time (s)) is collected for a minimum required time so the volume flux is considered significant. The flow is dependent on the cross-sectional area and velocity of the fluid: $Q = U \times A$, where U is the mean velocity of the fluid. Substituting $Q = UA$ in equation (1.11) results in:

$$f_d = \Delta h \frac{D_h}{L} 2g \frac{A^2}{Q^2} \tag{5.20}$$

In the equation above D_h, L, g and A are constants. The measurement of f_d depends primarily on Q and Δh, i.e $f_d = f(Q, \Delta h)$. Thus, the sensitivity df_d is given by:

$$df_d = \frac{\partial f_d}{\partial Q} dQ + \frac{\partial f_d}{\partial \Delta h} d\Delta h \tag{5.21}$$

where $\partial f_d/\partial Q$ and $\partial f_d/\partial \Delta h$ are given by:

$$\frac{\partial f_d}{\partial Q} = -\Delta h \frac{D_h}{L} 4g \frac{A^2}{Q^3} = \frac{-2 f_d}{Q} \tag{5.22}$$

$$\frac{\partial f_d}{\partial \Delta h} = \frac{D_h}{L} 2g \frac{A^2}{Q^2} = \frac{f_d}{\Delta h} \tag{5.23}$$

Substituting equations 5.22 and 5.23 into equation (5.21) and dividing by f_d results in:

$$\frac{df_d}{f_d} = -2\frac{dQ}{Q} + \frac{d\Delta h}{\Delta h} \tag{5.24}$$

equation (5.24) shows that measurements of Q are responsible for twice the systematic errors in comparison with errors in Δh. Variations in Q are given due to variations in the time T_f that the volume V is collected in the collection tank (Figure 5.7):

$$\begin{aligned} Q &= \frac{V}{T_f} \iff \\ dQ &= -\frac{V}{T_f^2} dT_f \iff \\ \frac{dQ}{Q} &= -\frac{dT_f}{T_f} \end{aligned} \tag{5.25}$$

The time deviation dT_f affect directly the accuracy of volume flux dQ that result in decrease of accuracy df_d. Table 5.3 shows the minimum time required to collect water flow to obtain values that will be within a maximum threshold, and the minimum

Variable	Unit	Smooth	Optimistic	Realistic	Pessimistic
f_d		0.024	0.008	0.016	0.020
		If $H_0 = 0.20$m			
dQ/Q	%	-0.663	-0.687	-0.672	-0.665
T_f	s	73.3	69.6	71.8	72.9
		If $H_0 = 0.27$m			
dQ/Q	%	-0.663	-0.687	-0.672	-0.665
T_f	s	63.1	59.9	61.8	62.8

Table 5.3: Values of accuracy and minimum time to measure flow in a duct with a super-hydrophobic top layer, to obtain significant experimental data.

accuracy required of experimental data that is obtained given the design parameters previously calculated in section 5.1.4.

Values of dQ were obtained by dividing assumed values of df_d by df_d/dQ calculated using equation 5.22. In equation 5.22 the values of D_h, L, g and A were known from the experimental design. The value of H was assumed to be 0.27 m, which was estimated as the highest initial head possible, due to the constrains of the experimental set-up, and Q was calculated by multiplying $U \times A$. Values of U calculated using equation 1.7 for estimated values of f_d of smooth perspex and optimistic to pessimistic values of the super-hydrophobic surface, presented in Table 5.3.

The minimum time T_f that the volume V is collected in the collection tank was calculated using the following equation:

$$T_f = \frac{A_t d_h}{dQ} \tag{5.26}$$

where d_h is the measurement tolerance of water height collected in the tank of area A_t.

The minimum accuracy for experimental data must be within approximately $\pm 0.66\%$ –this includes all systematic and random errors; and the water flow must be collected for at least 73 seconds.

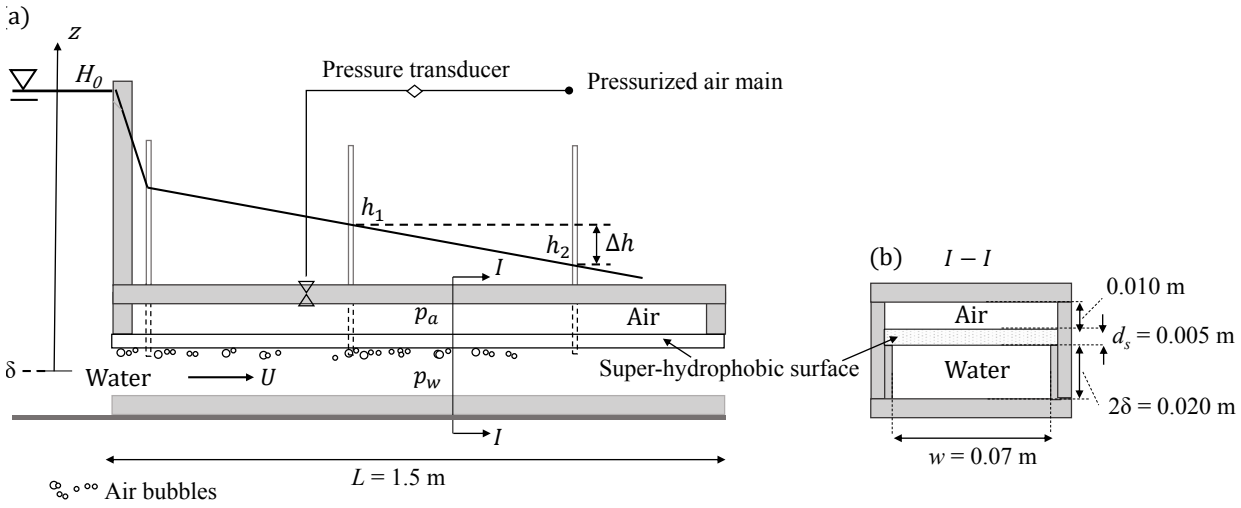

FIGURE 5.8: Definition sketch of experimental setup, showing the duct and the super-hydrophobic surface which separates the water layer from the air layer. The air layer can be pressurised to force air through the super-hydrophobic surface. (a) elevation view. (b) section I-I.

5.3 The experimental apparatus

The experimental apparatus used to determine the friction factor f_d is shown in Figure 5.8. The central element of the experimental setup was a duct of 0.055 m (height) × 0.1 m (width) × 1.5 m (length) made of acrylic. The duct was split into two compartments by an internal boundary which could be either super-hydrophobic or acrylic, and which separated the water below from an air layer above. The air layer could be pressurised to force air through the porous super-hydrophobic surface and thus recover the Cassie-Baxter state. The duct was placed in a flume of dimensions 0.3 m (height) × 0.1 m (width) × 3 m (length). Water was supplied at 18-19^{o}C from main tanks to the flume, and the height to which the water rises (initial head, $0.22 \leq H_0 \leq 0.27$ m) was controlled by changing the height of the spillway hole. A flow barrier wall was placed at the upstream side of the duct and the experimental setup was sealed into the flume, as seen in Figures 5.8 and 5.9.

Piezometric tubes were placed at 0.043, 0.145, 0.343, 0.686, 0.886 and 1.086 m from the upstream side of the duct, but head measurements are presented from 0.343 m

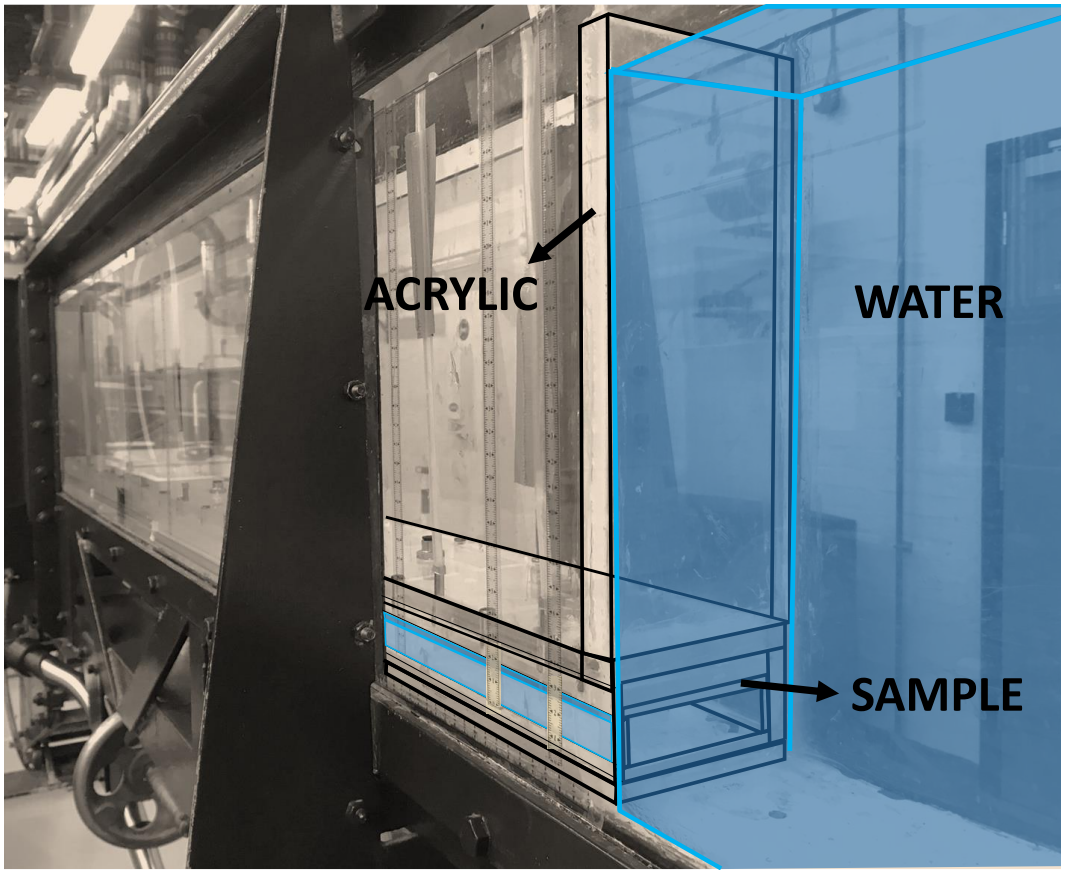

Figure 5.9: Experimental apparatus in flume

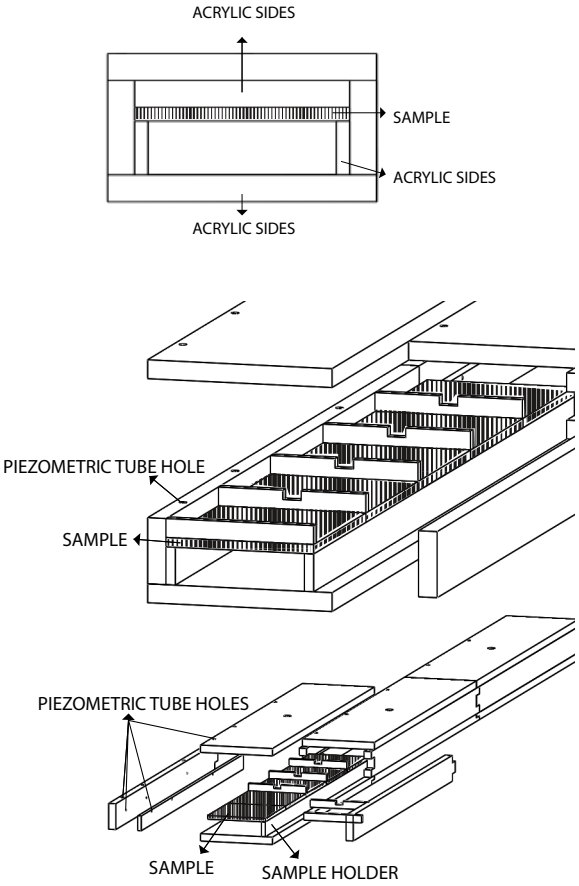

Figure 5.10: Exploded view of experimental apparatus

onwards to avoid contamination by entrance effects. Figure 5.10 shows the design of the experimental apparatus, drawn in SolidWorks®. The figure shows two exploded views that show the internal part of the apparatus. Acrylic pieces of $w = 0.005$ m were placed on the sides to provide support to the super-hydrophobic samples. Holes were drilled on the side to make the passage for the piezometric tubes. This was chosen because drilling the super-hydrophobic samples to place piezometric tubes could cause interference on the friction factor of the surface. The super-hydrophobic tiles were glued on to the acrylic sides in pairs with a two part epoxy adhesive (Araldite®, Basel, Switzerland) and sealed onto the duct with silicone glue (Marine High Modulous Silicone, Rhodorsil®, Lyon, France).

6

Experimental results for drag and durability

6.1 Introduction

This chapter focuses on presenting the results of f_d obtained by measuring the pressure drop of a turbulent water flow in a duct containing a super-hydrophobic wall produced as presented in Chapter 3 (sample ST). The recovery of the super-hydrophobic effects have been tested under static water pressure in Chapter 4. However, the advantages of using super-hydrophobic surfaces are in water flow applications, such as in the marine or drinking water industry, which are subjected to turbulent flows and high water pressure that could reduce significantly the robustness of the super-hydrophobic material. Of particular of interest is the recoverability of the Cassie-Baxter state and how the relaxation timescale T, that is, the typical time in which the surface transitions from the Cassie-Baxter to the Wenzel state, depends on the pressure difference across the surface.

The use of super-hydrophobic surfaces has been shown to be advantageous for applications such as the marine industry and transport of water in pipes (Fukuda et al., 2000, Yao et al., 2015, Moaven et al., 2013). However, the super-hydrophobic effect and the contact angle tend to decrease with time under continual water contact due to the loss of trapped air, causing the wetting state to transition from Cassie-Baxter to Wenzel. Super-hydrophobic surfaces that transition to the Wenzel state tend to have a higher drag than a smooth surface due to their high surface roughness (Du et al., 2017). The mechanism by which the air trapped in roughness elements of the super-hydrophobic surface is lost is via diffusion or air into the water and by dislocation of the air pockets (Brennan et al., 2015). The latter mechanism is particularly important for surfaces subjected to turbulent flow.

In section 6.2, the experimental setup is described. Section 6.3 presents the determination of f_d for the conditions described in 6.2 and the evolution of f_d over time. Section 6.4 explores models for the relation between relaxation time T and the pressure difference. Concluding remarks are made in section 6.5.

6.2 Methods - details of experimental sets

A series of nine experiments (3×3) were conducted, composed of three initial water pressure heads and three conditions of water flow-top surface of duct interaction. The three initial water heads H_0 were named: "**22**" for $H_0 = 0.22$ m; "**24**" for $H_0 = 0.24$ m; and "**27**" for $H_0 = 0.27$ m.

The top surface conditions were named: "**S**" for smooth acrylic; "**C**" for super-hydrophobic surface with air bubbles constantly applied across the surface; and "**I**" for super-hydrophobic surface with transient air bubbles applied across the surface.

Experiments S22 - S27 comprised an experiment with an acrylic top surface to verify the accuracy of the apparatus to determine the friction coefficient f_d. In addition to experiments S, two other measurement sets C and I, comprising of three experiments

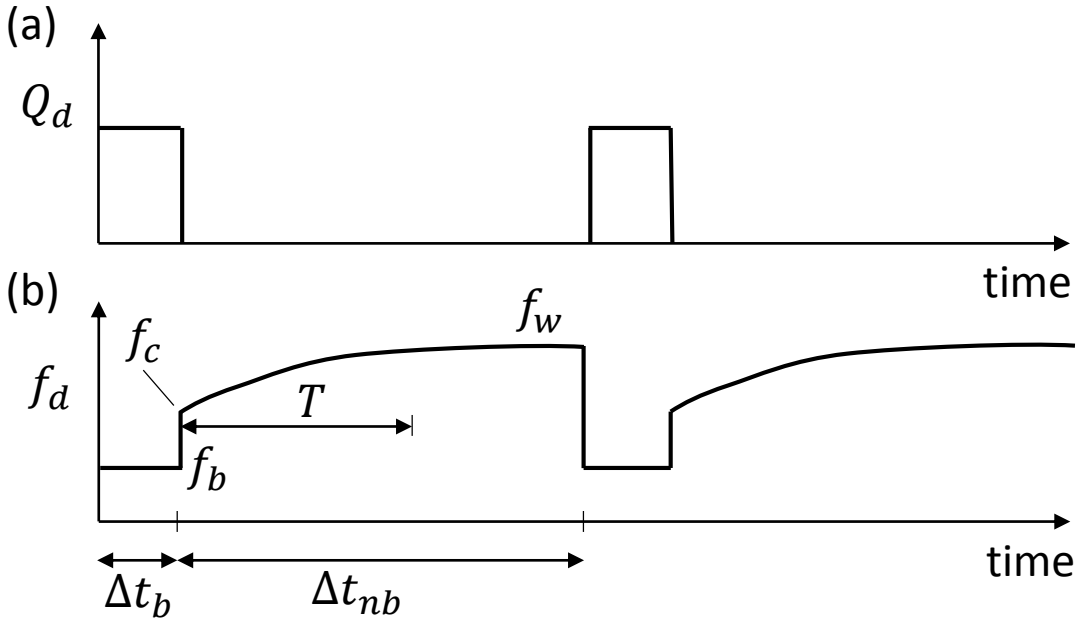

Figure 6.1: Schematic of the aeration strategy for experiment set I. Figure (a) shows the transient air flow Q_d applied across the surface and (b) shows the effect of (a) on the drag coefficient of the super-hydrophobic surface—when air bubbles are applied across the super-hydrophobic surface, the friction factor f_d is at its lowest (f_b), and as soon as the air bubbles stop, the friction factor of the surface increases from the moment the surface presents the friction factor at maximum super-hydrophobicity without air bubbles (f_c) and in the Cassie-Baxter state, to its maximum (f_w) when the surface has completely transitioned to the Wenzel state. The time of transition between f_c and f_w is the relaxation time T.

each, were performed with a super-hydrophobic top surface. Experiment sets S and C were performed for 2 hours, with measurements of water head and water flow taken every 30 minutes, and experiment set I was performed for 10 hours divided in 2 cycles of 5 hours with measurements of water head and water flow taken every 10 minutes in the first hour, and every 30 minutes in the following 4 hours, repeated at the end of the 5 hour cycle. In experiment set C continuous air bubble injection was applied through the surface for the whole duration of the experiment, and in experiment set I air bubbles were applied only prior to the start of the experiment and at specific times to recover the Cassie-Baxter state. The experiments were designed to measure the friction coefficient during fully aerated conditions (f_b), immediately after the aeration was stopped and the super-hydrophobic surface was in the Cassie-Baxter state (f_c) and the subsequent slow transition to the Wenzel state (f_w). This process is shown diagramatically in Figure 6.1. Aeration was performed for a time duration Δt_b, after which the super-hydrophobic surface transitions from Cassie-Baxter to Wenzel over a time-scale T, and the total time in which the surface was unaerated is denoted Δt_{nb}. The air hose was disconnected from the duct during Δt_{nb} to ensure p_a inside the aeration compartment was equal to the atmospheric pressure.

The aeration volume flux Q_d was achieved by applying an air pressure p_a to the air layer, and Q_d was measured using a Low Pressure Drop Flow Meter (Sensirion, Zürich, Switzerland). The air pressure p_a was obtained using a Gauge Pressure Sensor (Honeywell, New Jersey, United States) and an Arduino (Arduino, Turin, Italy) was used to record the analogue voltage output of the sensor.

Experiments C22-C27 were conducted to obtain f_b, whilst experiments I22-I27 were conducted to study the durability of the super-hydrophobicity of the surface. At $t = 0$ f_c was measured immediately after the experiment started. Between 0 and 1 hour f_d was measured every 10 minutes, and between 1 and 5 hours f_d was measured every 30 minutes. Values of f_w were taken when f_d was at its maximum at approximately t = 3-5 hours. Table 6.1 presents the experimental conditions.

Table 6.1: Conditions of experiments S22 - S27, C22 - C27 and I22 - I27.

Exp	H_0 (m)	Q_d (L min^{-1})	p_a (bar)	Δt_{nb} (min)	Δt_b (min)	Re (-) $\times 10^4$	n[xxiii]
S22	0.22	—	—	—	—	4.02	5
S24	0.24	—	—	—	—	4.45	5
S27	0.27	—	—	—	—	4.75	5
C22	0.22	1.5	0.10	0	300	4.38 —4.46	5
C24	0.24	2.0	0.11	0	300	4.57 —4.63	5
C27	0.27	2.2	0.15	0	300	4.77 —4.81	5
I22	0.22	1.5	0.10	300	10	4.00 —4.28	3
I24	0.24	2.0	0.11	300	10	4.40 —4.46	3
I27	0.27	2.2	0.15	300	10	4.50 —4.65	3

[xxiii] n = number of replicates

The average flow velocity U in the duct depends on the applied head H_0 and the friction factor of the duct f_d. The Reynolds number was sufficient for fully turbulent flow for all experiments, but the limited range in H_0 implies that the results are constrained to $Re = 4.0 - 4.8 \times 10^4$, as is shown in Table 6.1.

The super-hydrophobic surface across the top surface of the duct was prepared from single tiles of dimensions 0.1 m (length) $\times$ 0.08 m (width) $\times$ 0.005 m (d_s, height). A total of 15 tiles were placed along the duct as the top wall. The tiles were glued with silicone sealant to a piece of acrylic of width 0.05 m placed on both right and hand sides along the duct as an extra support for the tiles. Thus, the width of tiles exposed to the flow was 0.07 m. The volumetric flow rate Q, which is crucial to measure at high accuracy, was determined by collecting the water from the duct for three minutes.

The deviation in the flow rate Q within an experimental set, that is, the difference in the obtained values of Q between triplicate experiments (with the same configuration and conditions) was used to validate the precision of measurement of f_d of the acrylic walls. The friction factor of the acrylic was unknown, and values of f_d of the super-hydrophobic surface were expected to be similar to previous studies. For instance,

Walker et al. (2016) obtained a super-hydrophobic friction factor f_d 0.0164 ± 0.004[1] and a smooth f_d = 0.0240 for Re = 27,000. Other studies do not present values of f_d, but present values of drag coefficient and drag reduction, shown in Table 1.2. Measurements in drag reduction are directly proportional to reductions in the friction factor, as a consequence, the difference in the friction factor of a smooth surface and a super-hydrophobic surface under turbulent water flow could vary between 3% (Paik et al., 2015) and 50% (Daniello et al., 2009). The precision which f_d is measured is highly dependent on the precision measurement in Q, and if f_d of acrylic were similar to f_d of the super-hydrophobic surface, high precision measurements of Q would be needed. In this experiment a maximum df_d of 0.004 was considered for accurate results, as shown in section 5.2 in chapter 5.

6.3 Quantifying drag, recovery and durability of super-hydrophobic sample with turbulent water flow

6.3.1 Determination of f_d

Chapter 1 presented equation (1.11) ($\overline{f}_d = \Delta h\ D_h/L\ 2g/U^2$) that is used to estimate the friction factor by means of head losses, by measuring in terms of the difference in the piezometric head (Δh) between two piezometric tubes. Piezometric tubes at 0.343 (x_1), 0.686 m (x_2) and 0.886 m (x_3) from the upstream side of the duct were used to obtain the reading of water pressure head h_1 (at x_1), h_2 (at x_2) and h_3 (at x_3), from which three Δh were obtained from the difference h_1-h_2, h_1-h_3 and h_2-h_3.

Table 6.2 presents the results of friction factor of the super-hydrophobic surface f_d and the smooth surface f_B. For experiments S and C the measurements were taken throughout the 2 hour experimental period (t: —). For experiment set I, the friction

[1]Walker et al. (2016) presents the calculated *Fanning* friction factor f (f = 0.0041 ± 0.001). In this study the Darcy-Weissbach friction factor f_d is used, where $f_d = 4f$.

factor in table 6.2 is presented at specific times t, where $t = 0$ denotes that the measurement was taken immediately after the air bubbles supply was stopped (surface in the Cassie-Baxter state), and $t = 300$ denotes the time of the last measurement taken at the end of a 5 hour experimental period, after the surface transitioned to the Wenzel state.

Experiments S22 - S27 (all surfaces made from acrylic) were performed first, and the results of f_d for acrylic are presented in Table 6.2. Experiments S22 - S27 demonstrate that the mean value of f_d is within 99.5% of the expected value f_B, thereby clearly confirming the accuracy of the experimental setup, and indicate that the surface of acrylic is smooth, therefore f_B can be calculated using the Blasius equation for smooth surfaces at any $Re \geq 4{,}000$, presented in equation (5.18) (Nakayama, 2018). Results of experiments S22 - S27 were also used to measure the deviation in the flow rate Q. The flow rate was measured within sets S22, S24 and S27 and the deviation ΔQ of flow rate within each set was measured. Results showed a relative error $\Delta Q/Q$ of up to 0.5%, which suggests that the measured df_d is within the accepted range of precision. A previous study has reported a similar df_d between a super-hydrophobic and a smooth walls between flow in pipes of the same dimension at $Re \geq 4{,}000$ (Walker et al., 2016). Calculated values of f_d of the super-hydrophobic surface of experimental sets C and I are presented in Table 6.2. The results show a maximum decrease of 45% in f_d, in accordance with previous studies (Park et al., 2015, Murai et al., 2007). The distribution of points is given at different Re obtained by raising or lowering the initial head.

The reduction of f_d using the continuous bubble injection technique was due to the air pockets created by the air bubbles. The air pockets lower the interfacial contact between the fluid and the surface of the duct, and the increased contact between the gas-liquid lowers f_d due to the slip between the gas-liquid interface. Due to the continuous air bubble injection in experiments C22 - C27, Δf_d in all C-set experiments are lower than in experiments I22 - I27. For instance, experiments C22 and I22 were subjected to the same initial water head $H_0 = 0.22$ m, and the

Table 6.2: Friction coefficients f_d for acrylic reference surface (f_{d0}), super-hydrophobic surface with bubble injection (f_b), super-hydrophobic surface in Cassie-Baxter state (f_c) and in Wenzel state (f_w).

	Exp	t (minutes)	$f_d \pm$ std ($\times 10^{-2}$)	f_B ($\times 10^{-2}$)	Δf_d (%)
f_{d0}	**S22**	—	2.19 ± 0.17	2.20	7.7 [1]
	S24	—	2.19 ± 0.10	2.17	5.5 [1]
	S27	—	2.13 ± 0.14	2.13	6.5 [1]
f_b	**C22**	—	1.40 ± 0.08	2.56	-45
	C24	—	1.42 ± 0.22	2.53	-44
	C27	—	1.58 ± 0.08	2.51	-37
f_c	**I22**	0	1.53 ± 0.06	2.22	-31
	I24	0	1.57 ± 0.04	2.22	-29
	I27	0	1.52 ± 0.15	2.16	-29
f_w	**I22**	300	2.74 ± 0.06	2.23	+23
	I24	300	2.93 ± 0.04	2.20	+33
	I27	300	2.81 ± 0.15	2.17	+30

[1] Denotes the accuracy of the measurement technique.

presence of continuous air bubbles in experiment C22 reduced the friction factor 45% in relation to the smooth surface f_B whilst experiment I22 reduced 31% the friction factor in relation to the smooth surface, showing a Δf_d difference of 14% between C22 and I22 which is almost half of the Δf_d obtained in I22. This is also valid between experiment sets C24 and I24, and a lower Δf_d difference of 8% is found between the friction reduction Δf_d between experiment sets C27 and I27, which shows the friction reducing effect of air bubbles on the surface.

The super-hydrophobic surface holds the air pockets on the surface for a certain period without the continuous bubble injection. Without the slip effect of the air pockets the surface enters the Wenzel wetting state, and the friction factor increases to approximately 30% higher than f_B.

Results of f_d in the Cassie-Baxter state without continuous bubble injection are presented in Table 6.2 and show a reduction in the f_d of approximately 30%. Measurements of f_d were taken immediately after the air bubble injection was switched off. Figure 6.2 presents the normalised values of f_c and f_b, indicating little difference between the reduction in the friction factor between the two sets, showing it is possible to decrease f_d at similar rates but without the energy demand required to inject air bubbles.

The friction coefficient in the Wenzel state f_w can be used to estimate the relative roughness height ε of the surface by means of the Colebrooke-White equation (Colebrook & White, 1937):

$$\frac{1}{\sqrt{f_d}} = -2\log\left\{\frac{\varepsilon}{3.7D_h} + \frac{2.51}{Re\sqrt{f_d}}\right\} \tag{6.1}$$

The calculated values of ε for experiments I22 - I27 was found to be 70 $\pm$ 23 μm. Results from X-ray micrographs presented in Chapter 4 indicated a mean value of $\varepsilon = 30$ μm. X-ray micrographs analysis was obtained from a sample of dimensions 0.25×0.5×0.25 cm because a high resolution of the surface structure was required, and consequently the sample size analysed was substantially smaller than the sur-

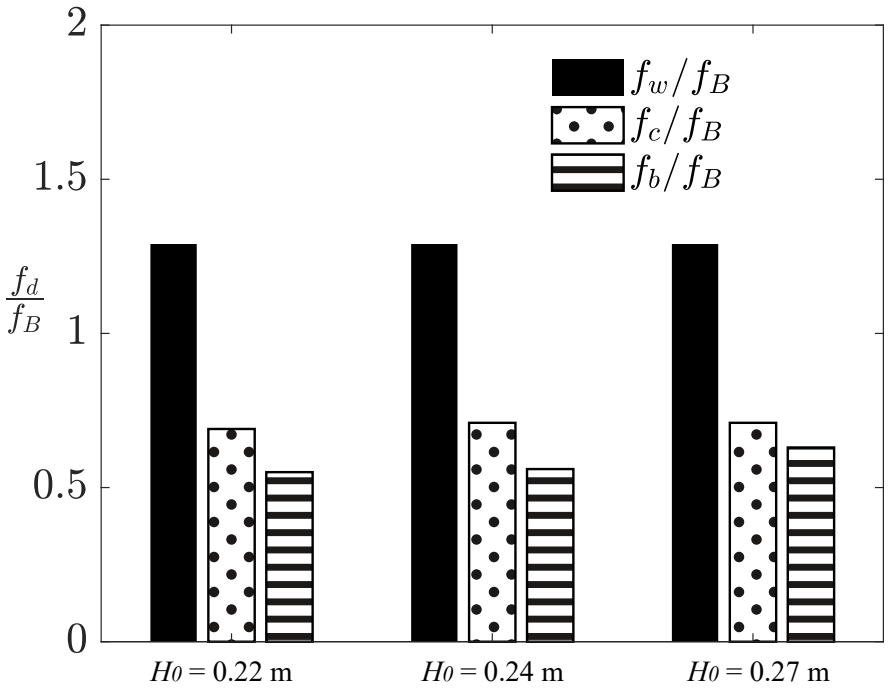

Figure 6.2: Comparison of normalised friction factor of a smooth surface (f_B) against the friction factor of the super-hydrophobic surface in the wetting state f_w, and the super-hydrophobic surface in the Cassie-Baxter state f_d with and without continuous bubble injection. The figure shows the ratios of f_w/f_B, f_c/f_B and f_b/f_B for the experiment set I at three initial water heads H_0.

face area applied in this study. Other studies of turbulent water flow on super-hydrophobic surfaces have applied engineered surface features of similar size range of 30-60 μm (Daniello et al., 2009). The size of features in super-hydrophobic surfaces of random surface structures presented in other studies range from 1 μm to 1 mm (Abu Rowin et al., 2018, Crick & Parkin, 2009).

The estimated values of ε/D_h of the super-hydrophobic surface in the Wenzel state is approximately 0.002, which is similar to the materials in modern commonly used pipes (Farshad & Rieke, 2006). In Figure 6.3 the values of f_d from experiment 4-6 for t up to 5 hours are compared with the calculated values of f_d obtained using relative roughness ratios (ε/D_h) from equation (6.1) for t up to 120 μm. As a consequence, when the lubricating air layer is decreased and the wetting state changes to Wenzel, the roughness of the surface is higher than a regular surface used in water transport, resulting in a drag increase of approximately 30% when compared with a completely smooth surface.

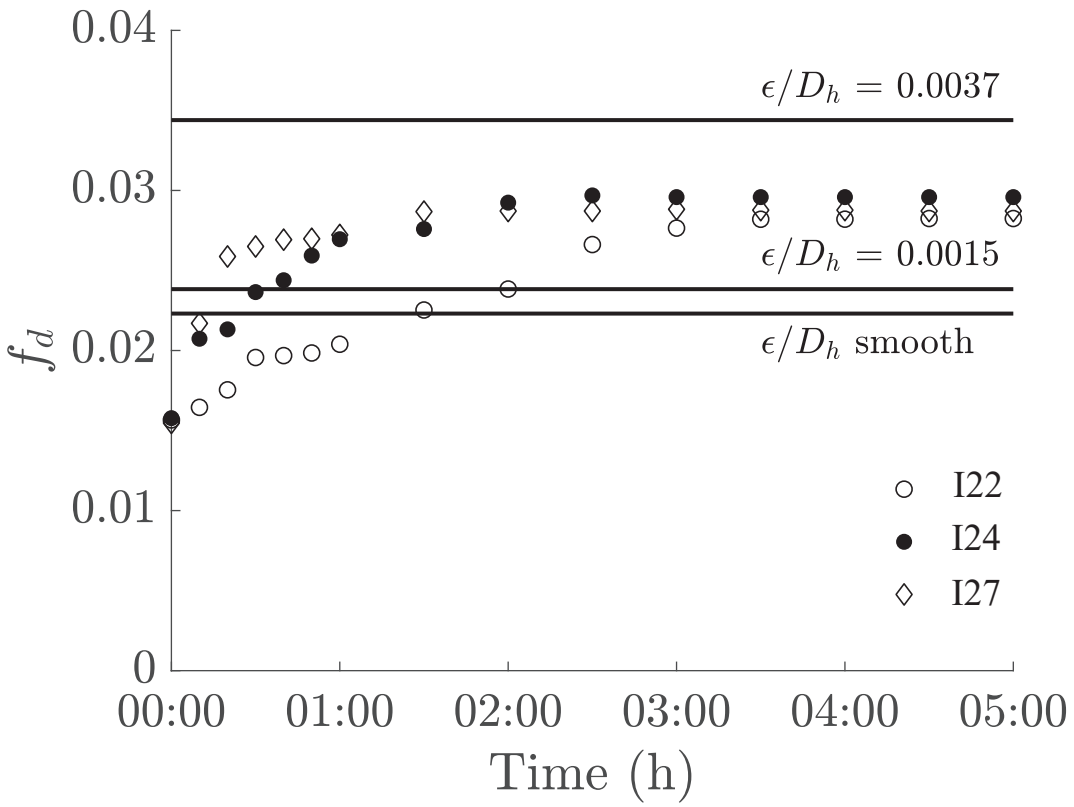

Figure 6.3: Experimental values of f_d without bubble injection compared with theoretical values of f_d of three relative roughness values. Values of f_d were calculated with equation (6.1). The data points of lower f_d are f_0. Values of f_d increase over time, and at approximately $t = 3$ hours f_d reaches the maximum relative roughness of approximately $\varepsilon/D_h = 0.003$. Some data points overlap at t = 3-5 hours, and consequently are not noticeable in the figure.

Surface roughness has a major effect in the wall friction factor of a surface. When the surface loses its super-hydrophobic effects and the flow is exposed to the surface roughness without the lubricating air layer, the wall friction increases to approximately 1.29 f_B because the roughness height is likely above the thickness of the viscous sub-layer. The ratio of the roughness elements is estimated in the form of roughness Reynolds number $Re_s = u_*\varepsilon/\nu$ which was defined in the introduction. The calculated Re_s was between 7 and 9, which indicates that the roughness elements are not considerably higher than the estimated viscous sub-layer and therefore are in the surface roughness is in the transitional regime.

6.3.2 Estimating the slip length ℓ_s in experiments I22 - I27

Previous studies have measured fluid slip at the wall ℓ_s from measurements of the velocity at the wall u_w, which can be obtained by using, for instance, Particle Image Velocimetry. Here ℓ_s is estimated from an estimation of the friction factor f_d and the correspondent values of $U\ell_s/\nu$ for a range of ℓ_s of 0-5% δ.

The experimental rig half channel height δ of 0.01 m was applied to estimate ℓ_s. Values of mean velocity U for each case I22, I24 and I27 obtained from the experimental results shown in Table 6.3 were used and the kinematic viscosity ν of water at 20°C of 1×10^{-6} m^2/s was used. These parameters were applied in the numerical simulation of water flow, presented in Chapter 5. The wall shear stress τ_w was calculated in Chapter 5 and is also mentioned in equation (1.9) where it is associated with the friction factor ($\tau_w = \frac{1}{8} f_d \rho U^2$). The slip length was estimated using equation (1.15) from the velocity output u obtained from the numerical simulation in Chapter 5 ($u_w = \ell_s \frac{du}{dz}\Big|_w$). To correlate the friction factor to ℓ_s, the term $\frac{du}{dz}\Big|_w$ from equation (1.15) is substituted in equation (1.12) ($\tau_w = \mu \frac{du}{dr}\Big|_w$), then τ_w from equation (1.9) into equation (1.12):

Table 6.3: Calculated values of ℓ_s based on comparing results of calculated f_d and experimental f_c

	$U\ell_s/\nu$	U	ℓ_s (μm)	% δ
I22	131.12	1.285	102.04	1.020
I24	108.16	1.325	81.63	0.816
I27	114.94	1.408	81.63	0.816

$$f_d = 8\frac{\nu}{U\ell_s}\frac{u_w}{U} \tag{6.2}$$

Calculated values of f_d from equation (1.9) were plotted against $U\ell_s/\nu$ using a range of ℓ_s of 1 to 10^4 μm and U from experiments I22, I24 and I27. The result is plotted in Figure 6.4 where each line corresponds to a Re calculated using the velocities U presented in table 6.3. The lines in Figure 6.4 are close because the velocities obtained from each experiment varied little. Then, values of the friction factor at t = 0 (f_c, table 6.2) of experiments I22, I24 and I27 were added to the lines of each respective Re by matching with the y-axis of the friction factor f_d calculated using the numerical simulation.

From each value of f_c of experiments I22, I24 and I27, a correspondent value of $U\ell_s/\nu$ was taken and used to calculate the estimated ℓ_s. The variables U and ν are known values. Then, U and ν were substituted to $U\ell_s/\nu$ to obtain the estimate value of ℓ_s. A summary of the estimated values of ℓ_s is presented in Table 6.3.

It can be seen in Table 6.3 that values of ℓ_s are approximately 1% δ (100 μm). Similar values have been found in (Daniello et al., 2009).

6.3.3 Durability of the super-hydrophobic surface and recovery of the Cassie-Baxter state

The evolution of the friction factor over time for experiments I22, I24 and I27 is presented in Figure 6.5. The figure shows a left-y axis showing the values of friction factor of the super-hydrophobic surface, a right-y axis showing the air pressure (bar)

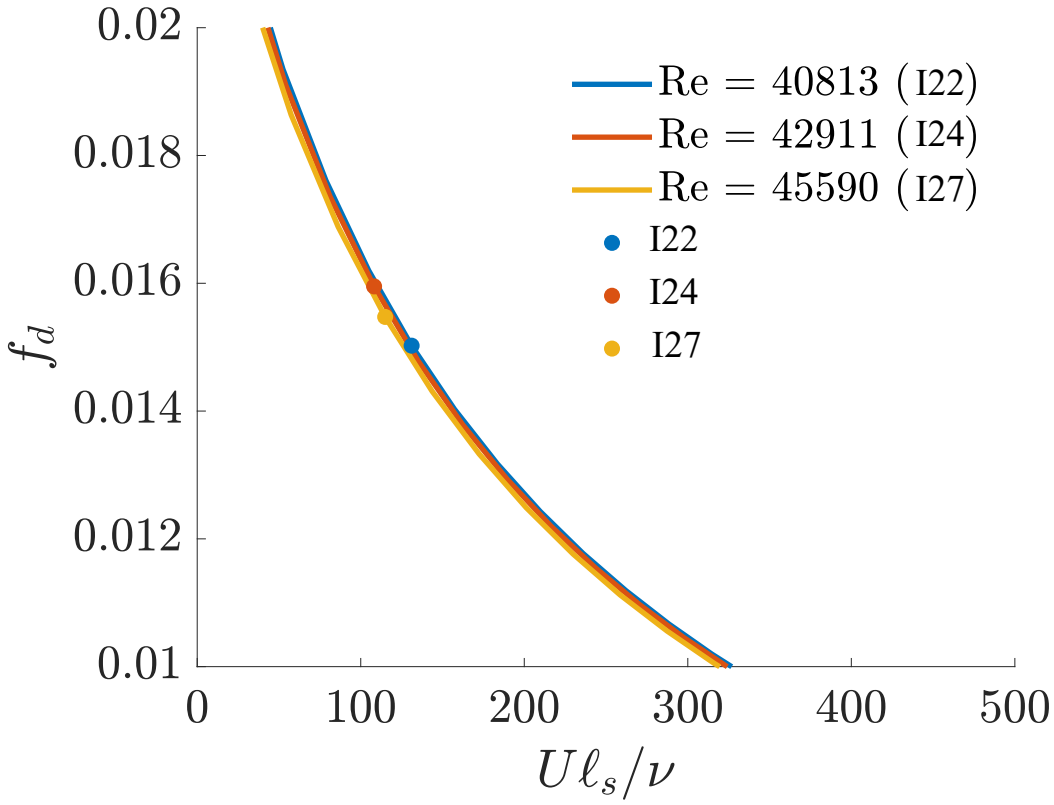

Figure 6.4: Friction factor f_d as a function of ℓ_s and U

applied across the porous material, and a x-axis showing the time evolution. The error bars show the deviation of the friction factor for each experiment I22, I24 and I27, calculated using the function *STDEV.S* of Microsoft Excel® (Microsoft, United States). The function *STDEV.S* estimates the standard deviation based on a sample. A sample size of 9 values of f_d was used for each experiment I22, I24 and I27. Immediately after the super-hydrophobic surface had been fully restored to the Cassie-Baxter state by blowing air through the surface, at $t = 0$, the experiments have a friction coefficient equal to f_c (Table 6.2). As time passes, the air pockets required for maintaining the Cassie-Baxter state disappear, thereby increasing f_d, passing the friction factor of an equivalent smooth surface (f_B) and settling onto the friction coefficient associated with the Wenzel state f_w due to the surfaces roughness. Once an air pressure was applied across the super-hydrophobic surface (see secondary axis in Figure 6.5) at the specified times in Table 6.2, the Cassie-Baxter state was recovered, as evident from the drop in f_d similar to that in the previous cycle. This

Table 6.4: Values of f_c, f_w and R^2 from best fit of first and second cycles of experiments I22, I24 and I27.

	First cycle t = 0-5 hours			Second cycle t = 5-10 hours		
Experiment	f_c	f_w	R^2	f_c	f_w	R^2
I22	0.0153	0.0274	0.96	0.0179	0.0280	0.96
I24	0.0157	0.0293	0.97	0.0170	0.0270	0.97
I27	0.0152	0.0281	0.97	0.0187	0.0290	0.94

is evidence of the capability of the material to recover the Cassie-Baxter state under turbulent conditions, confirming the results presented in Chapter 4 under static pressure.

The reference smooth wall value f_B (dashed line in Figure 6.5) is a useful indicator for the durability of the friction-reduction. The friction coefficients f_d are equal to f_B at different times for the three experiments, indicating that the durability of the Cassie-Baxter state depends strongly on the water pressure head (h) applied to the surface. Values of f_d show that once the top surface has transitioned from the Cassie-Baxter to the Wenzel state, f_d remains constant, and the values of f_d are then equivalent to that of a normal rough surface, as discussed in the previous section. A trend-line was fitted for each 5 hour cycle. More details of the trend-line fitting the evolution of f_d shown in Figure 6.5 are presented in the following section 6.4. The cycle starting at t = 5 hours presents the best fit line for the data of t = 5-10 hours, and a brighter grey line that is the best fit line of the first cycle of t = 0-5 hours for comparison. The second cycle at t = 5-10 hours shows that for experiment I22, the material displays fully repeatable behaviour, demonstrating the recoverability of the super-hydrophobicity. For experiments I24 and I27, the deviations with the first cycle are larger, although the period T over which the material transitions to the Wenzel state remains roughly the same. Table 6.4 summarises the values of f_c, f_w and R^2 (correlation coefficient) for experiments I22, I24 and I27 in the first cycle (t = 0-5 hours) and second cycle (t = 5-10 hours).

In experiment I22 f_d increased slowly, and the Cassie-Baxter state was retained for 1 hour. The initial friction factor value f_c was 0.0153 and increased gradually. At t =

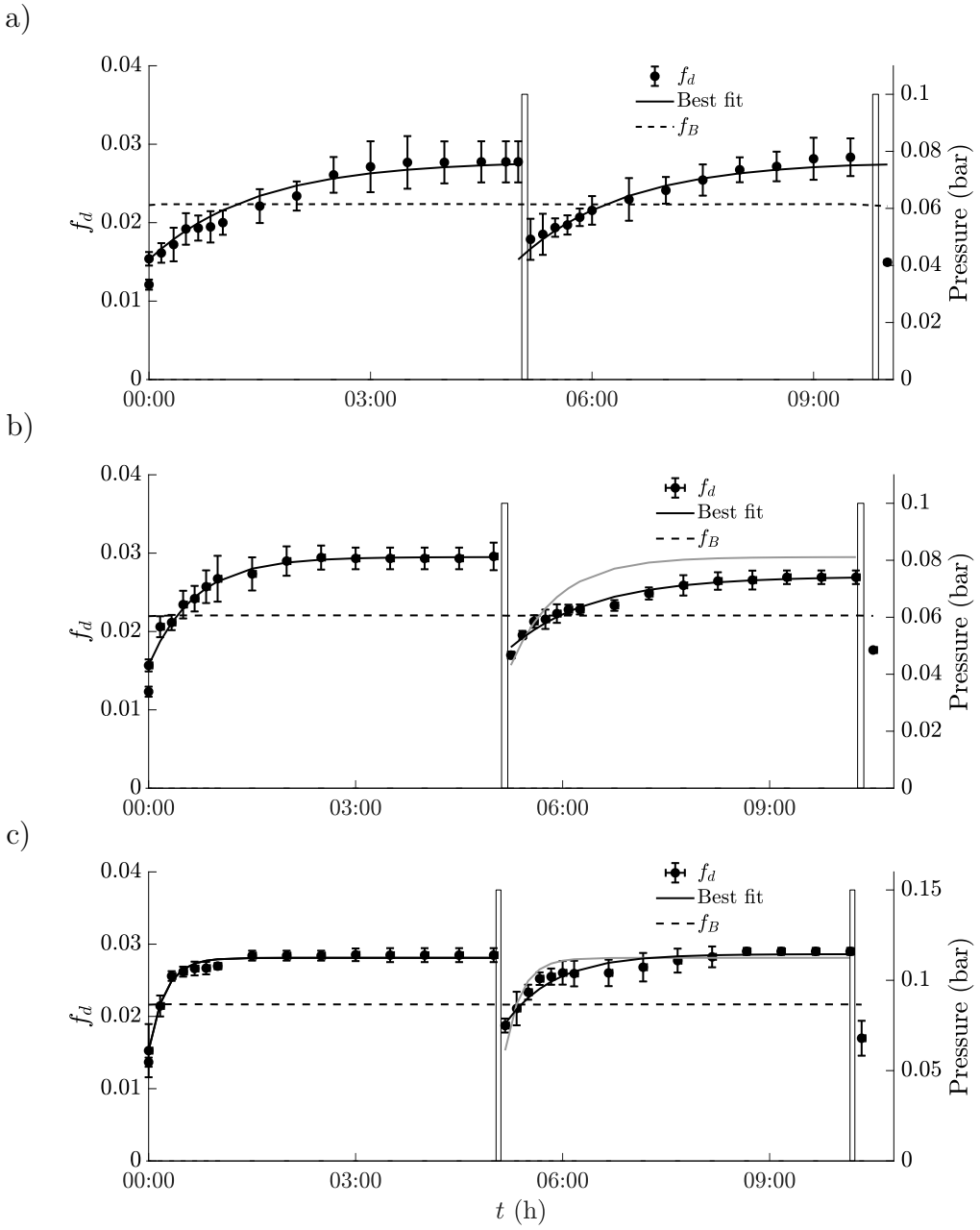

Figure 6.5: Evolution of f_d over time for experiments I22 (a), I24 (b) and I27 (c). The lowest data point at the initial time correspond to the values of f_d in C22 - C27. The data points are the measured values for f_d, the dashed line is the smooth wall value calculated using equation (5.18), and the solid lines are the best fit for each case. The secondary y axis denotes the pressure in the air chamber above the surface, and the bar plot shows when air pressure was applied at $t = 5$h and 10h. A pressure of 0.1 bar was applied to experiments I22 and I24, and 0.15 bar to experiment I27. In the second cycle $t = 5$-10 hours, the trend line of the first cycle is shown in grey for comparison.

40 minutes f_d becomes close to f_B. The trend-line suggests that f_d becomes equal to f_B at $t = 1$ hour. At t = 3 hours the surface had transitioned entirely to the Wenzel state and f_d increased to 0.0274, showing an increase of 1.8 f_c. After five hours, the air later was replenished by gently blowing air through the surface for 10 minutes. After the air flow was stopped, f_c was 0.0179, returning to values below the dashed f_B line and recovering the Cassie-Baxter state, but not fully to the initial value of 0.0153, i.e. an increase of 17% f_c. After the first recovery of the Cassie-Baxter state, f_d increase slowly once more and crossed f_B line after 1 hour from $f_c = 0.0179$. At t = 10.25 hr an air pressure was applied once more and f_c decreased to 0.0150, showing the full recovery of the Cassie-Baxter state for the second time.

In experiment I24 the surface transitioned from the Cassie-Baxter to the Wenzel state much more rapidly. The initial f_c value in Figure 6.5b was 0.0157 and crossed the f_B line between t = 35 and 40 minutes, as suggested by the trend-line. At t = 3 hours the Cassie-Baxter effect was completely depleted and f_d increased to 0.0293, showing an increase of 1.9 f_c. After replenishing the air layer $t = 5$ hours, f_d decreased to 0.0170, similarly to the case presented in Figure 6.5a. After the first recovery of the Cassie-Baxter state, f_c increased slowly once more and crossed f_B line after 30 minutes from $f_c = 0.0170$. The second cycle between $t = 5$ to 10 hr deviates from the data points between t = 0 and 5 hours. The data points after f_d crossed f_B line do not increase by as much as 1.9 f_c, but by 1.6 f_c at t=5hours. A second recovery of the Cassie-Baxter state occurred at $t = 10.25$ hours after a second air replenishment event after which f_d decreased to 0.0176. This is higher than the first and second f_c immediately taken after the first air pressure was applied.

In experiment I27 f_d increased rapidly and crossed the f_B line in under only 10 minutes. The initial friction factor f_c was 0.0153 and increased to a maximum of 0.0281 (1.8 f_c) at approximately t = 1.5 hours. At $t = 5$ hours an air pressure of 0.15 bar was applied and f_d decreased to 0.0187, 23% higher than f_c. In this experiment, a higher pressure was applied to inject air through the porous surface because it was observed that with 0.1 bar there were no bubbles leaving the surface. After the

recovery of the Cassie-Baxter state, f_c increased rapidly again, crossing f_B line in under 10 minutes and up to a maximum of 0.0290 at t = 9 hours (4 hours after f_d decreased to 0.0187). At t = 10.25 an air pressure of 0.15 bar was applied again and f_c decreased to 0.0170, which is 12% higher than f_c in the first cycle, but 20% lower than f_B, indicating the recovery of the Cassie-Baxter state.

6.4 Modelling the durability of the Cassie-Baxter state in the super-hydrophobic surface

To determine the relaxation time T in which the surface transitions from a Cassie-Baxter to a Wenzel state systematically, a best-fit to the data of f_d is applied for a function of the form

$$f_d = f_w + (f_c - f_w)\exp\left\{\left(-\frac{t}{T}\right)\right\} \tag{6.3}$$

This expression provides a robust means to define a T the relaxation (e-folding) time for the transition from Cassie-Baxter to Wenzel state. The best fit was determined using the MATLAB Curve Fitting App using values of T from the first cycle (t = 0 to 5 hours). Relaxation time T was 60 minutes for I22, 30 minutes for I24 and 10 minutes for I27. The correlation (R^2) for each case was at least R^2>0.94, which shows good data correlation. The time (T) of the Cassie-Baxter to Wenzel transition is compared in Figure 6.6 with the pressure of water to which the super-hydrophobic surface was subjected. Figure 6.6 shows the experimental results of T for I22 - I27 plotted against $1/\Delta p$ (p_a = 0 in I22 - I27 at t between 0-5 hours, therefore $\Delta p = p_w$). The data was fitted into a line following the linear equation $T = 1.97 \times 10^5/\Delta p$ - 1.91×10^2 obtained by linear regression and $R^2 \geq 0.997$, which indicates good data correlation. The regression line shows the relaxation time T tending to zero (Cassie-Baxter state lost immediately) at a pressure p_w of 1.0314×10^3 Pa, or h = 0.1051 m in terms of pressure head at the surface, which is only 5 mm higher than the maximum h obtained from the piezometric tube reading at x = 0.343 m. It was not

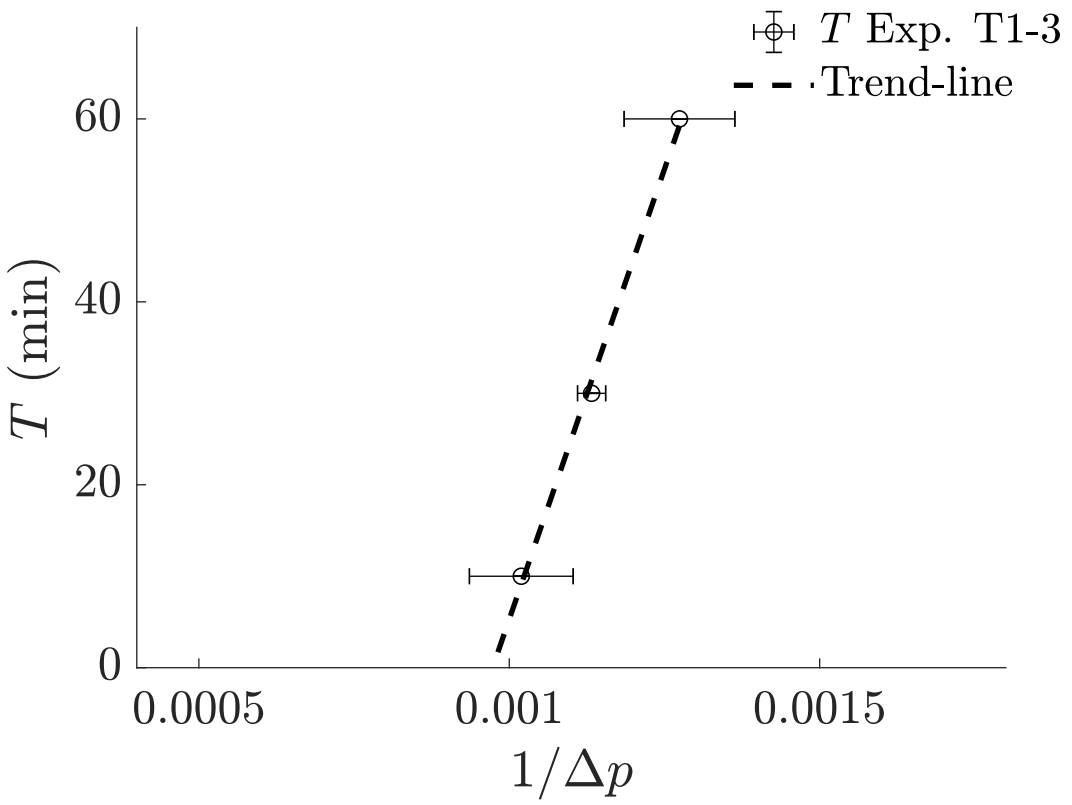

Figure 6.6: Values of T obtained at Δp of Exp. I22 - I27. Horizontal error bars were obtained from variations in height in piezometric tubes. Vertical error bars are not visible because no variation in the relaxation time T was observed. The dashed line is the linear regression following the linear equation $T = 1.97 \times 10^5/\Delta p$ - 1.91×10^2 and $R^2 \geq 0.997$.

possible to apply a higher p_w by raising the initial head H_0 due to the dimensions of the flume. It can be inferred from Figure 6.6 that the durability of the wetting state is linked to the pressure of water applied against the super-hydrophobic surface.

From the values of T for experiments I22 - I27, it is evident that there is a strong relationship dependence between the relaxation time T and the initial head H_0. Previous studies have shown a relationship between pressure of water and durability of the Cassie-Baxter state under static conditions, and durability of the air pockets and surface structure dependence. In regular super-hydrophobic surfaces the air pockets trapped on the surface are dislocated due to various factors including turbulence (Nosonovsky & Bhushan, 2008a). When not physically removed from the surface, the remaining air pockets are subjected to diffusion into water following Henry's gas law (Sander, 2015). The super-hydrophobic surface applied in this study was

developed with a porous structure to allow the injection of air bubbles by applying an air pressure across the porous medium. Whilst the continuous bubble injection allows the replenishment of the air layer and consequently the recovery of the Cassie-Baxter state, the material also is subjected to permeability of water due to the water pressure. The air trapped on the surface and throughout the material is connected due to high pore connectivity and can be dislocated/pushed upwards when another fluid applies pressure on the surface. The dislocation of the air pockets by water results in the transition of the Cassie-Baxter to Wenzel wetting state, presented as the evolution of f_d over time and correlating T and p_w in Figure 6.5.

The permeability of a porous medium depends on the viscosity and pressure of the fluid applied, and the permeability coefficient κ of the material. Predicting the permeability of water in the super-hydrophobic surface is an advantage because it allows the estimation of the longevity of the air pockets on the surface, and consequently the longevity of low f_d values. The permeability coefficient κ of the porous medium is generally estimated using the Darcy equation:

$$q = -\frac{\kappa \Delta p}{\mu d_S} \tag{6.4}$$

where Δp is the pressure difference (p_w - p_a) across the porous medium, d_S is the thickness of the super-hydrophobic surface, μ is the viscosity of the fluid, and the q is the Darcy velocity. To determine the reference permeability of the super-hydrophobic surface, the measurements taken during the air replenishment phase can be used. In this case, the Darcy velocity q can be obtained directly from the air flow rate Q_d. The pressure difference can be calculated from the the gauge pressure p_a in the air and in the water p_w. The latter was calculated from water head readings $h{=}p_w/\rho_w g + z$ at x = 0.343 m, where z is the elevation head, and here was considered $z = \delta$ for obtaining p_w at the surface of the duct. The dynamic viscosity of air is $\mu = 1.8 \times 10^{-5}$ Ns/m^2 at 20^{o}C, and the values of h were taken from the piezometric tube located at x = 0.343 m, used as the mean water pressure head value. The estimated permeability coefficient κ was $4.8 \pm 1 \times 10^{-15}$ m^2, which is of the same order of magnitude as

other super-hydrophobic porous materials (Patel et al., 2012). Using (6.4), the time for water to fill roughness elements ε on a rough surface can be argued to scale as:

$$T \sim \frac{\varepsilon}{q} = \frac{\varepsilon \mu d_S}{\kappa \Delta p} \tag{6.5}$$

Hence, T can expected to be inversely proportional to the pressure difference. By applying κ in the equation above to estimate the intrusion of water ($\mu = 1 \times 10^{-3}$ Ns/m^2 at 20^{o}C) and using $\varepsilon \approx 70$ μm results in a T of approximately one minute only, which does not correspond to the experimental data, where the relaxation time is approximately 60 minutes for I22, 30 minutes for I24 and 10 minutes for I27. Therefore the permeability of water in porous super-hydrophobic surfaces does not occur as in regular porous materials and the Darcy equation cannot be applied without considering the air bubble-water interaction at the super-hydrophobic surface.

6.5 Conclusion

For the first time the durability of friction reduction of a porous super-hydrophobic surface that can recover the Cassie-Baxter wetting state by blowing air through the surface under turbulent flow conditions was demonstrated. In the Cassie-Baxter state, the material under consideration showed reductions in the friction factor f_d of 31-45% relative to a standard hydraulically smooth surface. In the Wenzel state, the friction factor was 23-33% larger than for a smooth surface due to the surface roughness, which was estimated to be 70 μm. The Cassie-Baxter state could be recovered by gently blowing air through the super-hydrophobic surface for a short period of time.

It was shown that lifetime of the Cassie-Baxter state T depends strongly on the pressure of water applied against the super-hydrophobic surface. Observed values of T ranged from 10 to 60 minutes for a short head difference of only 5 cm. For a standard porous surface, the relaxation time T can be expected to scale inversely

proportional to the pressure difference Δp as $T = a\Delta p^{-1}$, where a is a constant. However, for the material under consideration this behaviour was not observed. A best fit of the data agreed best with $T = a(\Delta p^{-1} - \Delta p_{\max}^{-1})$, where $a = 1.97 \times 10^5$ and $\Delta p_{\max} = 1.031 \times 10^3$ Pa. This suggests that there is a critical pressure difference beyond which the Cassie-Baxter state cannot be sustained for the material under consideration. It was not possible to verify experimentally what happens at the critical pressure difference $\Delta p_{\max}$ due to the height of the flume in which the apparatus was placed which limits the initial head that can be applied. It was demonstrated that the observed behaviour for T was not consistent with existing theories that include super-hydrophobic effects in porous media for the material under consideration. Future research should concentrate on understanding this behaviour, how it links with the surface properties and the flow regime (laminar/turbulent).

The current study has shown that the material under consideration is able to recover the Cassie-Baxter state under fully immersed conditions. An important advantage of this material is that it is intrinsically hydrophobic – it does not rely on a surface coating which can be removed. This makes the surface suitable to achieve drag reduction in situations where the material is immersed for extended periods of time. However, the application should be one where the pressure difference is relatively small, as the relaxation time T was shown to be highly dependent on the pressure difference. This rules out, for the current time, applications in the water industry since the pressure heads inside water pipes far exceed those considered here.

7

Conclusion

The aim of this thesis was to reduce the energy needed for transporting water in pipes by implementing a robust super-hydrophobic surface. To achieve this aim, four objectives were addressed: 1) Manufacture a robust super-hydrophobic material able to maintain/recover a Cassie-Baxter state underwater; 2) Evaluate the viability of the new material for use in water transport applications; 3) Determine experimentally the friction factor as a function of time for the new super-hydrophobic material; and 4) Study the durability of the drag reduction for the new super-hydrophobic material.

This chapter presents this dissertation's distinct contributions to knowledge (section 7.1), a summary of the work (section 7.2), and recommendations for future research (section 7.3).

7.1 Contribution to knowledge

This dissertation focused on the application of friction-reducing super-hydrophobic materials for use in water distribution networks. In this environment, the material

will be constantly submerged, will be subjected to oxidising agents, and will be pressurised. The main contributions to knowledge are:

1. the development of a novel porous super-hydrophobic material which which is able to recover its super-hydrophobic and associated drag-reducing properties underwater. This is one of the key requirement to durability, since the friction-reduction relies on the existence of trapped air pockets on the surface of the material, and these need to be replenished regularly. The porosity of the novel material allows for air to be transported through the material so the air pockets can be replenished from the inside;

2. that the material appears safe for use in drinking water applications. This was established by immersing the material in a solution of high free chlorine concentration. The material was shown to maintain its super-hydrophobic properties and did not show any indication of reaction with the high free chlorine solution.

3. an extensive evaluation of the friction-reducing properties and durability of the new super-hydrophobic material. This involved the design of a new experimental apparatus able to measure the friction factor f_d and the volume flux Q within a margin of 7.7% and 0.5% respectively. The subsequent measurements showed that reductions in f_d (and thus of the power required) of up to 30% could be achieved.

7.2 Summary of key findings

One of the key problems of permanent friction-reduction by super-hydrophobic surfaces is that the air trapped between the rough surface and water is dislocated or diffused (the Cassie-Baxter state of wetting). The depletion of trapped air results in increased contact between the surface of the material and water, which increases the friction (the Wenzel state of wetting). The depletion of air was solved by applying an air flow through the material. To achieve this, a porous material was produced

with a super-hydrophobic surface. This enabled air to spread across the surface due to the high porous structure.

Chapter 2 presented the loss of super-hydrophobicity of three super-hydrophobic coatings: a) hydrophobic Paper Sludge Ash (HPSA); b) TiO_2 based super-hydrophobic paint; and c) NeverWet®. The loss of trapped air pockets was confirmed in the commercial spray coat NeverWet, and the loss of surface structure by analysing the sample using SEM and ultrasound. This chapter showed that the super-hydrophobic coatings under consideration are not suitable for drag reducing applications under constant water contact due to the low durability of the coatings.

Chapter 3 discussed the development and testing of a new super-hydrophobic material by sintering with various particle sizes and modifying with three different surface modifying agents. In this chapter three samples (sample number D, E and ST) modified with PFTS were selected to be evaluated on their ability to recover the Cassie-Baxter state under static water pressure in chapter via contact angle measurements. 4.

Chapter 4 evaluated the recovery of the Cassie-Baxter state of the novel material under static water pressure, and characterised samples D, E and SG according to their surface structure and properties. Sample SG showed full recovery of the Cassie-Baxter state (**objective 1**). The effects of free chlorine on the super-hydrophobic surface were investigated by measuring the concentration of free chlorine over time and the changes in contact angle of the material. Results showed there was no reaction of the material with the oxidising agents (NaOCl; **objective 2**).

Chapter 5 presented the considerations underpinning the design of the experimental setup. Numerical simulation was used to estimate the required setup length by determining the entrance length L_e for a smooth and super-hydrophobic surface with partial slip. Then, the required measurement accuracy was estimated in order to obtain be able to determine f_d with sufficiently small error bars. Estimating the entrance effects and required accuracy were important steps in the design of the

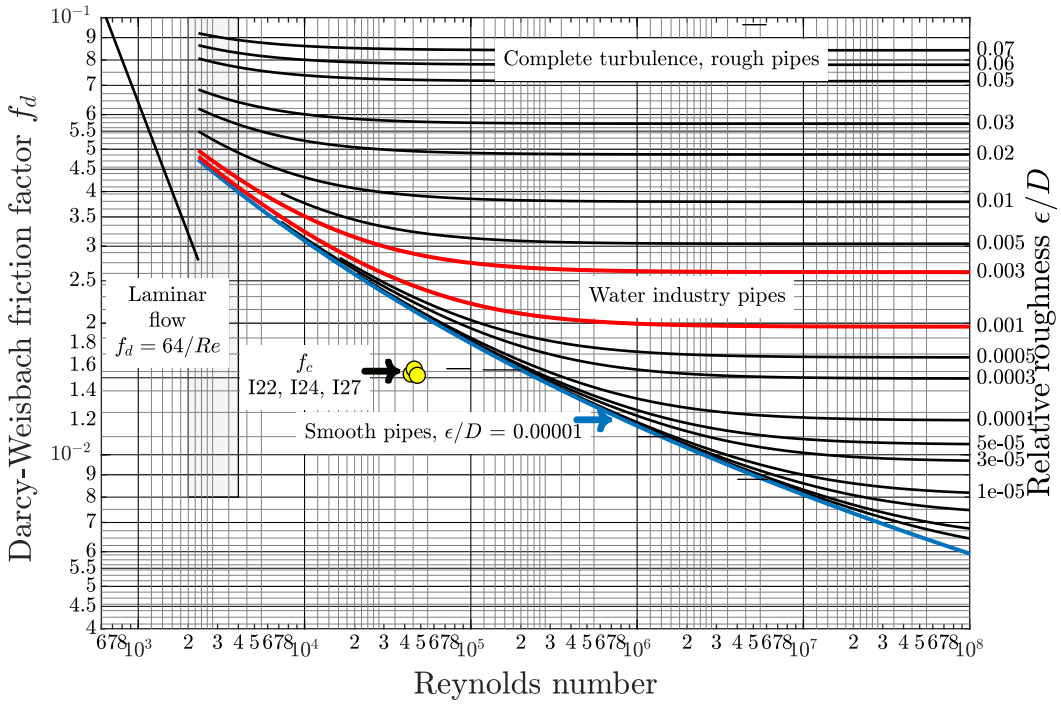

FIGURE 7.1: Moody diagram with values of f_c in yellow from experiments I22, I24 and I27. The data points are close because the difference in Re between each experiment set was small. The lowest possible friction factor for smooth surfaces is shown in blue, and below this line are the friction factor values obtained using the novel super-hydrophobic surface.

experimental apparatus.

Chapter 6 presented the friction-reduction experiments in the duct made with one super-hydrophobic wall. Friction-reductions of up to 45% were observed, which results in direct reduction in power consumption since $P_w = a\ \rho\ f_d\ U^3$. The friction factor at a $Re \sim 45{,}000$ is far below the line of the lowest possible friction factor (smooth surfaces) in the Moody diagram (See Figure 7.1). The durability of the super-hydrophobicity could be recovered by blowing air through the surface under turbulent flow conditions (**objectives 3 and 4**). Measurements of the friction factor over time showed that the durability of the Cassie-Baxter state is pressure dependent and restricted to applications of Re of up to approximately 45,000. One limitation found in this chapter is that the high pressure dependency of the durability of the Cassie-Baxter state limits the application of the current material for water transport purposes since these tend to be subjected to high water pressure.

7.3 Recommendations for future research

The research described in this dissertation led to a new material with a low-friction super-hydrophobic surface that is able to reduce the friction of a surface under turbulent flow. However further optimisation of this surface is recommended to address key issues raised below:

1. ***Producing a lighter porous super-hydrophobic material*** In this study a porous material was produced by sintering soda-lime glass powder, which is dense and fragile. For future studies, it is recommended the use of a lighter hydrophobic powder, such as hydrophobic thermoplastics. The use of a hydrophobic thermoplastic would eliminate the modification of surface chemistry step, and increase the potential uses of the material, since materials such as High-density Polyethylene and other similar materials are well accepted in various industries, including for drinking water distribution;

2. ***Roughness height of surface features:*** The estimation of the roughness Reynolds number Re_s ($Re_s = \varepsilon u_t/\nu$) in chapter 6 estimated that Re_s was in the transition between smooth and rough flow when subjected to a $Re > 45{,}000$ flowing on a super-hydrophobic surface with surface features sizes $\varepsilon > 50\ \mu m$. It is recommended that future work considers producing surfaces with smaller surface features, i.e. nano-metre size range.

3. ***Surface chemistry:*** FTIR spectroscopy results showed a broad absorbance band around 3300 cm^{-1}, possibly from an incomplete reaction with PFTS. The sintered soda-lime glass material should be subjected to another step before reaction with PFTS to promote hydrolysis of the Si-O bonds into Si-O-H.

Further optimisation of analysis methods are also recommended:

1. ***Obtaining measurements of the velocity at the wall:*** The slip length was calculated based on numerical simulation and estimated from the f_d, as

shown in Chapter 6. This estimation could be confirmed by direct measurements of the slip velocity at the wall with particle image velocity analysis (PIV). PIV has been used by other authors to estimate l_s and confirm the presence of a partial slip on the surface of super-hydrophobic surfaces. By measuring directly a partial slip on the surface, this could be linked to the changes in friction factor, that is, how much slip affects the drag reduction;

2. ***Observing the mechanism by which air pockets disappear:*** Air pockets are the key to decrease friction in super-hydrophobic surfaces. Understanding the main mechanism by which they decrease leads to improvement in manufacturing a surface that can hold the Cassie-Baxter state under turbulent conditions for longer periods.

These recommendations would assist in improving the durability of the Cassie-Baxter state under pressurised conditions. Improvements to the material could lead to the manufacturing of a lighter, more robust structure. The effects of surface structure on the durability of the Cassie-Baxter state need to be better analysed by measuring directly the slip and the decrease of air pockets on the surface. These are measures that could improve the feasibility of the material as a drinking water pipe. Moreover, the proposed improvements could broaden the use of the material in applications that do not require the surface to be under pressurised conditions indefinitely. For instance, applying the material for biofouling and self-cleaning purposes in the built environment and vessels. In the built environment, the use of a super-hydrophobic surface has the potential to decrease the frequency of which surfaces require maintenance. In vessels, biofouling additives are key factors in the formulation of protective coatings. An improved, lighter version of the material presented in this thesis could enhance the durability and efficiency of materials that are of engineering interest in the built environment and maritime applications.

References

Abramoff, M., Magalhaes, P., & Ram, S. (2004). Image processing with imagej. http://webeye.ophth.uiowa.edu/dept/BIOGRAPH/ABRAMOFF/ImageJ.pdf. 64

Abu Rowin, W., Hou, J., & Ghaemi, S. (2018). Turbulent channel flow over riblets with superhydrophobic coating. *Experimental Thermal and Fluid Science*, *94*, 192–204. DOI http://dx.doi.org/10.1016/j.expthermflusci.2018.02.001. 112

Ahsan, M. S., Dewanda, F., Lee, M. S., Sekita, H., & Sumiyoshi, T. (2013). Formation of superhydrophobic soda-lime glass surface using femtosecond laser pulses. *Applied Surface Science*, *265*, 784 – 789. DOI http://dx.doi.org/10.1016/j.apsusc.2012.11.112. 56

Bahng, J. H., Yeom, B., Wang, Y., Tung, S. O., Hoff, J. D., & Kotov, N. (2015). Anomalous dispersions of hedgehog particles. *Nature*, *517*(7536), 596–599. DOI http://dx.doi.org/10.1038/nature14092. 13

Barthlott, W., Mail, M., Bhushan, B., & Koch, K. (2017). Plant surfaces: Structures and functions for biomimetic innovations. *Nano-Micro Letters*, *9*. DOI http://dx.doi.org/10.1007/s40820-016-0125-1. 5

Bennett, D., & Glaser, R. (2011). Common pitfalls in hydraulic design of large diameter pipelines: Case studies and good design practice. *Pipelines*, (pp. 961–971). DOI http://dx.doi.org/10.1061/41187(420)88. 2

Bhushan, B. (2001). *Surface Roughness Analysis and Measurement Techniques*, book section 2, (pp. 1–71). CRC Press. 61, 62

Binder, K., Müller, M., Kremer, M., & Schnurpfeil, A. (Eds.) (2016). *NIC Symposium 2016*, vol. 48 of *Publication Series of the John von Neumann Institute for Computing (NIC) NIC Series*. Jülich: Forschungszentrum Jülich GmbH Zentralbibliothek, Verlag. 6

Bobji, M. S., Kumar, S. V., Asthana, A., & Govardhan, R. N. (2009). Underwater sustainability of the cassie state of wetting. *Langmuir*, *25*(20), 12120–12126. DOI http://dx.doi.org/10.1021/la902679c. 8, 24, 42

Boinovich, L., Emelyanenko, A., & Pashinin, A. (2010). Analysis of long-term durability of superhydrophobic properties under continuous contact with water. *ACS Applied Materials and Interfaces*, *2*(6), 1754–1758. DOI http://dx.doi.org/10.1021/am100241s. 30, 42

Boreyko, J. B., & Chen, C.-H. (2009). Restoring superhydrophobicity of lotus leaves with vibration-induced dewetting. *Physical Review Letters*, *103*(17), 174502. DOI https://dx.doi.org/10.1103/PhysRevLett.103.174502. 24

Boulos, P. F., & Bros, C. M. (2010). Assessing the carbon footprint of water supply and distribution systems. *Journal - AWWA*, *102*(11), 47–54. DOI http://dx.doi.org/10.1002/j.1551-8833.2010.tb11338.x. 1

Brassard, J.-D., Sarkar, D. K., & Perron, J. (2015). Studies of drag on the nanocomposite superhydrophobic surfaces. *Applied Surface Science*, *324*, 525–531. DOI http://dx.doi.org/10.1016/j.apsusc.2014.10.084. 23

Brennan, J. C., Geraldi, N. R., Morris, R. H., Fairhurst, D. J., McHale, G., & Newton, M. I. (2015). Flexible conformable hydrophobized surfaces for turbulent flow drag reduction. *Scientific Reports*, *5*, 10267. DOI http://dx.doi.org/10.1038/srep10267. 104

Callies, M., & Quere, D. (2005). On water repellency. *Soft Matter*, *1*(1), 55–61. DOI http://dx.doi.org/10.1039/B501657F. 8

Chakraborty, A., Xiang, M., & Luo, C. (2013). Fabrication of super-hydrophobic microchannels via strain-recovery deformations of polystyrene and oxygen reactive ion etch. *Materials (Basel, Switzerland)*, *6*(8), 3610–3623. DOI http://dx.doi.org/10.3390/ma6083610. 33, 35

Chen, B., Qiu, J., Sakai, E., Kanazawa, N., Liang, R., & Feng, H. (2016). Robust and superhydrophobic surface modification by a paint + adhesive method: Applications in self-cleaning after oil contamination and oil-water separation. *ACS Applied Materials & Interfaces*, *8*(27), 17659–17667. DOI http://dx.doi.org/10.1021/acsami.6b04108. 56

Colebrook, C. F., & White, C. M. (1937). Experiments with fluid friction in roughened pipes. *Proceedings of the Royal Society of London. Series A, Mathematical and Physical Sciences*, *161*(906), 367–381. 2, 3, 92, 111

Costantini, R., Mollicone, J.-P., & Battista, F. (2018). Drag reduction induced by superhydrophobic surfaces in turbulent pipe flow. *Physics of Fluids*, *30*(2), 025102. DOI http://dx.doi.org/10.1063/1.5011805. 21

Crick, C. R., & Parkin, I. P. (2009). A single step route to superhydrophobic surfaces through aerosol assisted deposition of rough polymer surfaces: duplicating the lotus effect. *Journal of Materials Chemistry*, *19*(8), 1074–1076. DOI http://dx.doi.org/10.1039/B820102C. 13, 112

Crick, C. R., & Parkin, I. P. (2010). Superhydrophobic polymer films via aerosol assisted deposition - taking a leaf out of nature's book. *Thin Solid Films*, *518*(15), 4328–4335. DOI http://dx.doi.org/10.1016/j.tsf.2010.02.040. 12, 13

Crick, C. R., & Parkin, I. P. (2011). Superhydrophobic silica films on glass formed by hydrolysis of an acidic aerosol of tetraethylorthosilicate. *Journal of Materials Chemistry*, *21*(25), 9362–9366. DOI http://dx.doi.org/10.1039/C1JM10825E. 11, 14, 47, 48, 51, 55, 56, 153

Daniello, R. J., Waterhouse, N. E., & Rothstein, J. P. (2009). Drag reduction in turbulent flows over superhydrophobic surfaces. *Physics of Fluids*, *21*(8), 085103. DOI doi:http://dx.doi.org/10.1063/1.3207885. 15, 21, 22, 54, 65, 66, 92, 97, 108, 112, 115

Davis, A. M. J., & Lauga, E. (2009). Geometric transition in friction for flow over a bubble mattress. *Physics of Fluids*, *21*(1), 011701. DOI http://dx.doi.org/10.1063/1.3067833. 21

Deborde, M., & von Gunten, U. (2008). Reactions of chlorine with inorganic and organic compounds during water treatment-kinetics and mechanisms: A critical review. *Water Research*, *42*(1), 13–51. DOI http://dx.doi.org/10.1016/j.watres.2007.07.025. 77

Dou, W., Wang, P., Zhang, D., & Yu, J. (2016). An efficient way to prepare hydrophobic antireflective SiO_2 film by sol-gel method. *Materials Letters*, *167*, 69–72. DOI http://dx.doi.org/10.1016/j.matlet.2015.12.146. 12, 47, 55

Doube, M., Klosowski, M. M., Arganda-Carreras, I., Cordeliéres, F. P., Dougherty, R. P., Jackson, J. S., Schmid, B., Hutchinson, J. R., & Shefelbine, S. J. (2010). Bonej: Free and extensible bone image analysis in imagej. *Bone*, *47*(6), 1076–1079. DOI http://dx.doi.org/10.1016/j.bone.2010.08.023. 64

Drinking Water Inspectorate (2016). Regulation 31 of the water supply (water quality) regulations. Http://www.dwi.gov.uk/drinking-water-products/approved-products/soslistcurrent.pdf. 26

Du, P., Wen, J., Zhang, Z., Song, D., Ouahsine, A., & Hu, H. (2017). Maintenance of air layer and drag reduction on superhydrophobic surface. *Ocean Engineering*, *130*, 328 – 335. DOI http://dx.doi.org/10.1016/j.oceaneng.2016.11.028. 8, 24, 26, 30, 104

Farshad, F. F., & Rieke, H. H. (2006). Surface roughness design values for modern pipes. *SPE Drilling and Completion*, *21*(03), 212–215. DOI http://dx.doi.org/10.2118/89040-PA. 112

Fuaad, P. A., Baig, M. F., & Ahmad, H. (2016). Drag-reduction in buoyant and neutrally-buoyant turbulent flows over super-hydrophobic surfaces in transverse orientation. *International Journal of Heat and Mass Transfer*, *93*, 1020–1033. DOI http://dx.doi.org/10.1016/j.ijheatmasstransfer.2015.10.068. 23, 92

Fukuda, K., Tokunaga, J., Nobunaga, T., Nakatani, T., Iwasaki, T., & Kunitake, Y. (2000). Frictional drag reduction with air lubricant over a super-water-repellent surface. *Journal of Marine Science and Technology*, *5*(3), 123–130. DOI http://dx.doi.org/10.1007/s007730070009. 24, 25, 104

Gaffney, J. S., Marley, N. A., & Jones, D. E. (2012). *Fourier Transform Infrared (FTIR) Spectroscopy*, (pp. 1–33). American Cancer Society. 64

Guan, N., Liu, Z., Jiang, G., Zhang, C., & Ding, N. (2015). Experimental and theoretical investigations on the flow resistance reduction and slip flow in super-hydrophobic micro tubes. *Experimental Thermal and Fluid Science*, *69*, 45–57. DOI http://dx.doi.org/10.1016/j.expthermflusci.2015.08.003. 11, 12

IEA (2016). *Water Energy Nexus*. International Energy Agency. 1

James P. Farr, W. L. S., & Steichen, D. S. (2000). *Kirk-Othmer Encyclopedia of Chemical Technology*. John Wiley & Sons. 76

Jenner, E., Barbier, C., & D´ Urso, B. (2013). Durability of hydrophobic coatings for superhydrophobic aluminum oxide. *Applied Surface Science*, *282*, 73–76. DOI http://dx.doi.org/10.1016/j.apsusc.2013.05.049. 25, 30, 42

Jones, G. F. (2011a). *Chapter 2 - The Fundamental Principles*. No. 5 in Gravity-Driven Water Flow in Network. John Wiley and Sons, Inc. 1

Jones, G. F. (2011b). *Chapter 6 -Natural diameter of a pipe: local static pressure*. No. 5 in Gravity-Driven Water Flow in Network. John Wiley and Sons, Inc. 16

Kang, S.-J. L. (2005). 1 - sintering processes. In S.-J. L. Kang (Ed.) *Sintering*, (pp. 3 – 8). Oxford: Butterworth-Heinemann. 47

Kay, M. (1998). *Practical Hydraulics*. Taylor and Francis. 2

Knaust, S., Andersson, M., Hjort, K., & Klintberg, L. (2016). Influence of surface modifications and channel structure for microflows of supercritical carbon dioxide and water. *The Journal of Supercritical Fluids*, *107*, 649–656. DOI http://dx.doi.org/10.1016/j.supflu.2015.07.027. 10, 12

Kota, K. G., A., & Tuteja, A. (2014). The design and applications of superomniphobic surfaces. *NPG Asia Mater*, *8*. DOI http://dx.doi.org/10.1038/am.2014.34. 8

Krevelen, D. V., & Nijenhuis, K. T. (2009). Chapter 8 - Interfacial Energy Properties. In D. V. Krevelen, & K. T. Nijenhuis (Eds.) *Properties of Polymers (Fourth Edition)*, (pp. 229 – 244). Amsterdam: Elsevier, fourth edition ed. 6

La, D.-D., Nguyen, T. A., Lee, S., Kim, J. W., & Kim, Y. S. (2011). A stable superhydrophobic and superoleophilic Cu mesh based on copper hydroxide nanoneedle arrays. *Applied Surface Science*, *257*(13), 5705–5710. DOI http://dx.doi.org/10.1016/j.apsusc.2011.01.078. 14

Lari, K. S., Reeuwijk, M. v., & Maksimović, Č. (2010). Simplified numerical and analytical approach for solutes in turbulent flow reacting with smooth pipe walls. *Journal of Hydraulic Engineering*, *136*(9), 626–632. DOI http://dx.doi.org/10.1061/(ASCE)HY.1943-7900.0000229. 86

Lee, C., & Kim, C.-J. (2011). Underwater restoration and retention of gases on superhydrophobic surfaces for drag reduction. *Physical Review Letters*, *106*(1), 014502. DOI http://dx.doi.org/10.1103/PhysRevLett.106.014502. 24, 25, 42

Leung, W. M., Axelson, D. E., & Van Dyke, J. D. (1987). Thermal degradation of polyacrylamide and poly(acrylamide-co-acrylate). *Journal of Polymer Science Part A: Polymer Chemistry*, *25*(7), 1825–1846. DOI http://dx.doi.org/10.1002/pola.1987.080250711. 151

Li, J., Fu, J., Cong, Y., Wu, Y., Xue, L., & Han, Y. (2006). Macroporous fluoropolymeric films templated by silica colloidal assembly: A possible route to super-hydrophobic surfaces. *Applied Surface Science*, *252*(6), 2229–2234. DOI http://dx.doi.org/10.1016/j.apsusc.2005.03.224. 9, 13

Li, W., & Amirfazli, A. (2008). Hierarchical structures for natural superhydrophobic surfaces. *Soft Matter*, *4*(3), 462–466. DOI http://dx.doi.org/10.1039/B715731B. 48, 50, 54

Lin, J., Lin, F., Liu, R., Li, P., Fang, S., Ye, W., & Zhao, S. (2020). Scalable fabrication of robust superhydrophobic membranes by one-step spray-coating for gravitational water-in-oil emulsion separation. *Separation and Purification Technology*, *231*, 115898. DOI http://dx.doi.org/10.1016/j.seppur.2019.115898. 14

Lu, N., Zhang, W., Weng, Y., Chen, X., Cheng, Y., & Zhou, P. (2016a). Fabrication of PDMS surfaces with micro patterns and the effect of pattern sizes on bacteria adhesion. *Food Control*, *68*, 344–351. DOI http://dx.doi.org/10.1016/j.foodcont.2016.04.014. 10

Lu, N., Zhang, W., Weng, Y., Chen, X., Cheng, Y., & Zhou, P. (2016b). Fabrication of PDMS surfaces with micro patterns and the effect of pattern sizes on bacteria adhesion. *Food Control*, *68*, 344–351. DOI http://dx.doi.org/10.1016/j.foodcont.2016.04.014. 11, 12

Lu, X., Peng, Y., Qiu, H., Liu, X., & Ge, L. (2017a). Anti-fouling membranes by manipulating surface wettability and their anti-fouling mechanism. *Desalination*, *413*, 127–135. DOI http://dx.doi.org/10.1016/j.desal.2017.02.022. 64, 71

Lu, X., Taiwo, O. O., Bertei, A., Li, T., Li, K., Brett, D. J. L., & Shearing, P. R. (2017b). Multi-length scale tomography for the determination and optimization of the effective microstructural properties in novel hierarchical solid oxide fuel cell anodes. *Journal of Power Sources*, *367*, 177–186. DOI http://dx.doi.org/10.1016/j.jpowsour.2017.09.017. 64

Lu, Y., Sathasivam, S., Song, J., Crick, C. R., Carmalt, C. J., & Parkin, I. P. (2015). Robust self-cleaning surfaces that function when exposed to either air or oil. *Science*, *347*(6226), 1132–1135. DOI http://dx.doi.org/10.1126/science.aaa0946. 14, 31, 32, 33

Maharjan, S., Liao, K.-S., Wang, A. J., Barton, K., Haldar, A., Alley, N. J., Byrne, H. J., & Curran, S. A. (2020). Self-cleaning hydrophobic nanocoating on glass: A scalable manufacturing process. *Materials Chemistry and Physics*, *239*, 122000. DOI http://dx.doi.org/10.1016/j.matchemphys.2019.122000. 12

Masad, J. (1995). On the Roughness Reynolds Number Transition Criterion. *ASME. J. Fluids Eng*, *117*, 727–729. DOI http://dx.doi.org/10.1115/1.2817329. 19

Mihály, J., Sterkel, S., Ortner, H. M., Kocsis, L., Hajba, L., Furdyga, E., & Mink, J. (2006). FTIR and FT-Raman spectroscopic study on polymer based high pressure digestion vessels. *Croatica Chemica Acta*, *79*(3), 497–501. ISSN-0011-1643. 64, 71

Min, T., & Kim, J. (2004). Effects of hydrophobic surface on skin-friction drag. *Physics of Fluids*, *16*(7), L55–L58. DOI http://dx.doi.org/10.1063/1.1755723. 21, 22

Moaven, K., Rad, M., & Taeibi-Rahni, M. (2013). Experimental investigation of viscous drag reduction of superhydrophobic nano-coating in laminar and turbulent flows. *Experimental Thermal and Fluid Science*, *51*, 239–243. DOI http://dx.doi.org/10.1016/j.expthermflusci.2013.08.003. 22, 23, 104

Mohamed, A. M. A., Abdullah, A. M., & Younan, N. A. (2015). Corrosion behavior of superhydrophobic surfaces: A review. *Arabian Journal of Chemistry*, *8*(6), 749–765. DOI http://dx.doi.org/10.1016/j.arabjc.2014.03.006. 24

Mohammadi, R., Wassink, J., & Amirfazli, A. (2004). Effect of surfactants on wetting of super-hydrophobic surfaces. *Langmuir*, *20*(22), 9657–9662. DOI http://dx.doi.org/10.1021/la049268k. 25

Moody, L. (1944). Friction factors for pipe flow. *Trans. ASME*, *66*(8), 671–677. 3, 18

Munson, B. R., Young, D. F., & Okiishi, T. H. (2009). *Fundamentals of fluid mechanics*. Hoboken, N.J. Chichester: Wiley ; John Wiley [distributor], 6th ed. xiii, 3

Murai, Y., Fukuda, H., Oishi, Y., Kodama, Y., & Yamamoto, F. (2007). Skin friction reduction by large air bubbles in a horizontal channel flow. *International Journal of Multiphase Flow*, *33*(2), 147–163. DOI http://dx.doi.org/10.1016/j.ijmultiphaseflow.2006.08.008. 24, 25, 26, 109

Nakayama, Y. (2018). *7. Flow in Pipes*. Elsevier. 2, 19, 96, 109

Navier, C. (1823). Memoire sur les lois du mouvement des fluids. *l' Académie Royale des Sciences de l' Institut de France, Mém. Acad. R. Sci. Inst. Fr.*, *6*, 389–440. 20

Nikuradse, J. (1933). Laws of flow in rough pipes. *VDI Forschungsheft*, (p. 361). 2, 3

Nosonovsky, M., & Bhushan, B. (2008a). *Friction, Superhydrophobicity, and Biomimetics*. Springer-Verlag Berlin Heidelberg. 2, 4, 8, 9, 11, 121

Nosonovsky, M., & Bhushan, B. (2008b). *Friction, Superhydrophobicity, and Biomimetics*, book section 2, (pp. 13–26). Springer-Verlag Berlin Heidelberg. 4, 7

Nouri, N. M., Sekhavat, S., & Mofidi, A. (2012). Drag reduction in a turbulent channel flow with hydrophobic wall. *Journal of Hydrodynamics, Ser. B*, *24*(3), 458–466. DOI http://dx.doi.org/10.1016/S1001-6058(11)60267-9. 22

Ohkubo, Y., Tsuji, I., Onishi, S., & Ogawa, K. (2010). Preparation and characterization of super-hydrophobic and oleophobic surface. *Journal of Materials Science*, *45*(18), 4963–4969. DOI http://dx.doi.org/10.1007/s10853-010-4362-2. 13

Oyola-Reynoso, S., Wang, Z., Chen, J., CÄśnar, S., Chang, B., & Thuo, M. (2015). Revisiting the challenges in fabricating uniform coatings with polyfunctional molecules on high surface energy materials. *Coatings*, *5*(4), 1002–1018. DOI http://dx.doi.org/10.3390/coatings5041002. 56

Paik, B.-G., Pyun, Y.-S., Kim, K.-Y., Jung, C.-M., & Kim, C.-G. (2015). Study on the micro-dimpled surface in terms of drag performance. *Experimental Thermal and Fluid Science*, *68*, 247–256. DOI http://dx.doi.org/10.1016/j.expthermflusci.2015.04.021. 22, 23, 108

Pan, Q., Wang, M., & Wang, H. (2008). Separating small amount of water and hydrophobic solvents by novel superhydrophobic copper meshes. *Applied Surface Science*, *254*(18), 6002–6006. DOI http://dx.doi.org/10.1016/j.apsusc.2008.03.034. 13

Pantz, J. (2013). *Development of a high sorptivity porous material from waste glass*. Master's thesis, Imperial College London. 151

Park, H. J., Tasaka, Y., Oishi, Y., & Murai, Y. (2015). Drag reduction promoted by repetitive bubble injection in turbulent channel flows. *International Journal of Multiphase Flow*, *75*, 12–25. DOI http://dx.doi.org/10.1016/j.ijmultiphaseflow.2015.05.003. 24, 25, 109

Patel, S. U., Manzo, G. M., Patel, S. U., Kulkarni, P. S., & Chase, G. G. (2012). Permeability of electrospun superhydrophobic nanofiber mats. *Journal of Nanotechnology*, (p. 7). DOI http://dx.doi.org/10.1155/2012/483976. 123

Priezjev, N. V., Darhuber, A. A., & Troian, S. M. (2005). Slip behavior in liquid films on surfaces of patterned wettability: Comparison between continuum and molecular dynamics simulations. *Physical Review E*, *71*(4), 041608. DOI http://dx.doi.org/10.1103/PhysRevE.71.041608. 20

Rahman, N. A. A., Fowler, A., & Martin, P. J. (2013a). Wall slip and viscous dissipation in ice cream pipe rheometry. *Journal of Food Engineering*, *119*(4),

731–737. DOI http://dx.doi.org/10.1016/j.jfoodeng.2013.06.048. 20, 23, 92

Rahman, N. A. A., Fowler, A., & Martin, P. J. (2013b). Wall slip and viscous dissipation in ice cream pipe rheometry. *Journal of Food Engineering*, *119*(4), 731–737. DOI http://dx.doi.org/10.1016/j.jfoodeng.2013.06.048. 94

Sander, R. (2015). Compilation of henry's law constants (version 4.0) for water as solvent. *Atmospheric Chemistry and Physics*, *15*(8), 4399–4981. DOI http://dx.doi.org/10.5194/acp-15-4399-2015. 121

Schlichting, H., & Gersten, K. (2017). *Boundary-Layer Theory*. Springer, 9 ed. 85

Shirtcliffe, N. J., McHale, G., Newton, M. I., & Zhang, Y. (2009). Superhydrophobic copper tubes with possible flow enhancement and drag reduction. *ACS Applied Materials and Interfaces*, *1*(6), 1316–1323. DOI http://dx.doi.org/10.1021/am9001937. 25, 94

Sikka, V. K., Hurley, M., & Lim, Z. W. (2016). 32

Spathi, C., Young, N., Heng, J., Vandeperre, L., & Cheeseman, C. (2015). A simple method for preparing super-hydrophobic powder from paper sludge ash. *Materials Letters*, *142*, 80–83. DOI http://dx.doi.org/10.1016/j.matlet.2014.11.123. 13, 31

Staff, M. W. H. A., Crittenden Communications, S., Trussell, R. R., Hand, D. W., Tchobanoglous, G., Howe, K. J., & Crittenden, J. C. (2012). *Principles of Water Treatment*. Somerset, United States: John Wiley & Sons, Incorporated. 76, 77

Tao, C., Yan, H., Yuan, X., Yin, Q., Zhu, J., Ni, W., Yan, L., & Zhang, L. (2016). Sol-gel based antireflective coatings with superhydrophobicity and exceptionally low refractive indices built from trimethylsilanized hollow silica nanoparticles. *Colloids and Surfaces A: Physicochemical and Engineering Aspects*, *509*, 307–313. DOI http://dx.doi.org/10.1016/j.colsurfa.2016.08.055. 9, 13, 47, 48, 51, 153

Teisala, H., & Butt, H.-J. (2019). Hierarchical structures for superhydrophobic and superoleophobic surfaces. *Langmuir*, *8*, 10689–10703. DOI http://dx.doi.org/10.1021/acs.langmuir.8b03088. 10

Tian, H., Zhang, J., Wang, E., Yao, Z., & Jiang, N. (2015). Experimental investigation on drag reduction in turbulent boundary layer over superhydrophobic surface by trpiv. *Theoretical and Applied Mechanics Letters*, *5*(1), 45–49. DOI http://dx.doi.org/10.1016/j.taml.2015.01.003. 23

Tretheway, D. C., & Meinhart, C. D. (2002). Apparent fluid slip at hydrophobic microchannel walls. *Physics of Fluids*, *14*(3), L9–L12. DOI doi:http://dx.doi.org/10.1063/1.1432696. 20

Voronov, R. S., Papavassiliou, D. V., & Lee, L. L. (2007). Slip length and contact angle over hydrophobic surfaces. *Chemical Physics Letters*, *441*(4-6), 273–276. DOI http://dx.doi.org/10.1016/j.cplett.2007.05.013. 20

Walker, G. M., Albadarin, A. B., McGlue, A., Brennan, S., & Bell, S. E. J. (2016). Analysis of friction factor reduction in turbulent water flow using a superhydrophobic coating. *Progress in Organic Coatings*, *90*, 472–476. DOI http://dx.doi.org/10.1016/j.porgcoat.2015.08.002. 21, 23, 56, 92, 94, 97, 108, 109

Wang, B., Wang, J., Dou, Z., & Chen, D. (2014). Investigation of retention of gases in transverse hydrophobic microgrooved surfaces for drag reduction. *Ocean Engineering*, *79*, 58–66. DOI http://dx.doi.org/10.1016/j.oceaneng.2014.01.015. 24

Wenzel, R. N. (1936). Resistance of solid surfaces to wetting by water. *Industrial and Engineering Chemistry*, *28*(8), 988–994. DOI http://dx.doi.org/10.1021/ie50320a024. 9, 24

WHO (2003). Chlorine in drinking-water - background document for development of WHO guidelines for drinking-water quality. 77

Wong, H. S., Barakat, R., Alhilali, A., Saleh, M., & Cheeseman, C. R. (2015). Hydrophobic concrete using waste paper sludge ash. *Cement and Concrete Research*, *70*, 9–20. DOI http://dx.doi.org/10.1016/j.cemconres.2015.01.005. 32

Xu, M., Sun, G., & Kim, C.-J. (2014). Infinite lifetime of underwater superhydrophobic states. *Phys. Rev. Lett.*, *113*, 136103. DOI http://dx.doi.org/10.1103/PhysRevLett.113.136103. 25

Xu, Q., Shen, L., Duan, P., Zhang, L., Fu, F., & Liu, X. (2020). Superhydrophobic cotton fabric with excellent healability fabricated by the grafting to method using a diblock copolymer mist. *Chemical Engineering Journal*, *379*, 122401. DOI http://dx.doi.org/10.1016/j.cej.2019.122401. 13

Yan, L., qin Dong, F., Zhao, S., Yan, H., Lv, H., & Yuan, X. (2014). Hydrophobic MgF2 antireflective films with enhanced environmental durability by a sol-gel process. *Materials Letters*, *129*, 156–158. DOI http://dx.doi.org/10.1016/j.matlet.2014.05.036. 12

Yang, C., Tartaglino, U., & Persson, B. (2006). Influence of surface roughness on superhydrophobicity. *Physical review letters*, *97*, 116103. DOI 10.1103/PhysRevLett.97.116103. 61

Yao, Y., Luo, J.-l., Liu, H., & Zhu, K. (2015). Water tunnel experimental investigation on drag reduction of coating surface wall. *Procedia Engineering*, *126*, 247–253. DOI http://dx.doi.org/10.1016/j.proeng.2015.11.235. 21, 23, 92, 104

Ybert, C., Barentin, C., Cottin-Bizonne, C., Joseph, P., & Bocquet, L. (2007). Achieving large slip with superhydrophobic surfaces: Scaling laws for generic geometries. *Physics of Fluids*, *19*(12). DOI http://dx.doi.org/10.1063/1.2815730. 10, 21, 54

Yin, X., Wang, Z., Shen, Y., Mu, P., Zhu, G., & Li, J. (2020). Facile fabrication of superhydrophobic copper hydroxide coated mesh for effective separation of water-in-oil emulsions. *Separation and Purification Technology*, *230*, 115856. DOI http://dx.doi.org/10.1016/j.seppur.2019.115856. 13

Yuyang, L., Xianqiong, C., & Xin, J. H. (2008). Hydrophobic duck feathers and their simulation on textile substrates for water repellent treatment. *Bioinspiration & Biomimetics*, *3*(4), 046007. DOI http://dx.doi.org/10.1088/1748-3182/3/4/046007. 13

Zhang, J., Yang, S., & Liu, J. (2018). Numerical investigation of a novel device for bubble generation to reduce ship drag. *International Journal of Naval Architecture and Ocean Engineering*, *10*(5), 629 – 643. DOI http://dx.doi.org/10.1016/j.ijnaoe.2017.10.009. 24, 25

Zhang, P., Zhang, J., Xue, Z., Wang, J., & Jiang, L. (2017). Reliable manipulation of gas bubbles by regulating interfacial morphologies and chemical components. *Materials Horizons*, *4*(4), 665–672. DOI http://dx.doi.org/10.1039/C7MH00145B. 74

Zhang, Z., Ge, B., Men, X., & Li, Y. (2016a). Mechanically durable, superhydrophobic coatings prepared by dual-layer method for anti-corrosion and self-cleaning. *Colloids and Surfaces A: Physicochemical and Engineering Aspects*, *490*, 182–188. DOI http://dx.doi.org/10.1016/j.colsurfa.2015.11.049. 9

Zhang, Z., Ge, B., Men, X., & Li, Y. (2016b). Mechanically durable, superhydrophobic coatings prepared by dual-layer method for anti-corrosion and self-cleaning. *Colloids and Surfaces A: Physicochemical and Engineering Aspects*, *490*, 182–188. DOI http://dx.doi.org/10.1016/j.colsurfa.2015.11.049. 12, 13, 47, 55

Zhao, D.-Y., Huang, Z.-P., Wang, M.-J., Wang, T., & Jin, Y. (2012). Vacuum casting replication of micro-riblets on shark skin for drag-reducing applications. *Journal of Materials Processing Technology*, *212*(1), 198–202. DOI http://dx.doi.org/10.1016/j.jmatprotec.2011.09.002. 12

Zheng, Q., & Lü, C. (2014). Size effects of surface roughness to superhydrophobicity. *Procedia IUTAM*, *10*, 462 – 475. Mechanics for the World: Proceedings of the 23rd International Congress of Theoretical and Applied Mechanics, ICTAM2012. DOI http://dx.doi.org/10.1016/j.piutam.2014.01.041. 74

Zhou, C., & Michael, N. (2017). Revisiting lowest possible surface energy of a solid. *Surface Topography: Metrology and Properties*, *5*(4), 045001. DOI https://dx.doi.org/10.1088/2051-672X/aa84c9. 4, 6

Appendices

A

Loss of super-hydrophobicity in super-hydrophobic coatings

In this appendix a series of pictures showing the evolution of the loss of super-hydrophobicity is shown for the three coatings investigated in Chapter 2.3 - PSA, TiO_2 paint and NeverWet®. The pictures show firstly a droplet of water resting on the surface of each coating before the experiment had been initiated, then after 3 hours and finally after most of the surface had become hydrophiblic - 6 hours for the PSA, 78 hours for the TiO_2 paint and Neverwet®.

A.1 PSA

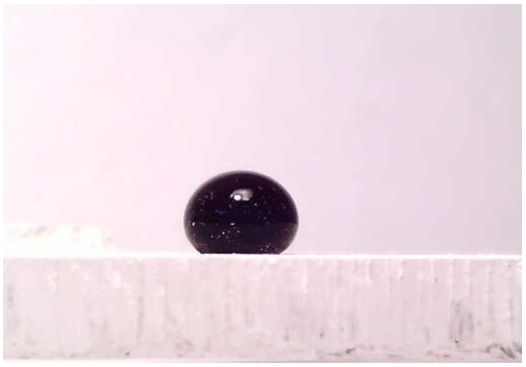

FIGURE A.1: Droplet of water resting on a surface coated with PSA before the preliminary experiment was initiated

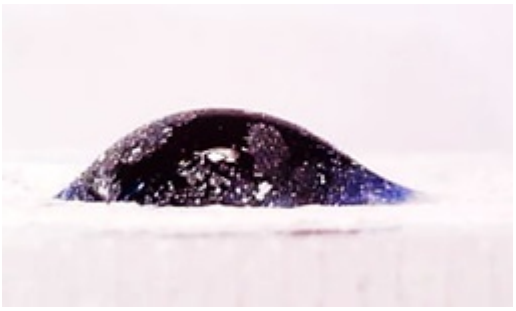

FIGURE A.2: Droplet of water resting on a surface coated with PSA after 3 hours the preliminary experiment was initiated

FIGURE A.3: Droplet of water resting on a surface coated with PSA after 6 hours the preliminary experiment was initiated

A.2 TiO_2 super-hydrophobic paint

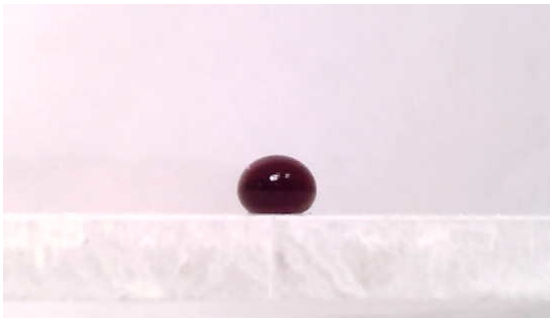

FIGURE A.4: Droplet of water resting on a surface coated with TiO_2 super-hydrophobic paint before the preliminary experiment was initiated

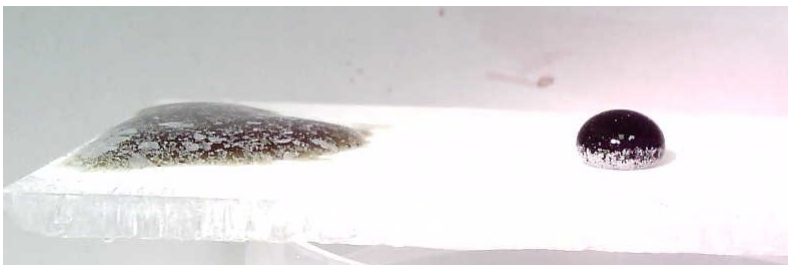

FIGURE A.5: Droplet of water resting on a surface coated with TiO_2 super-hydrophobic paint after 3 hours the preliminary experiment was initiated

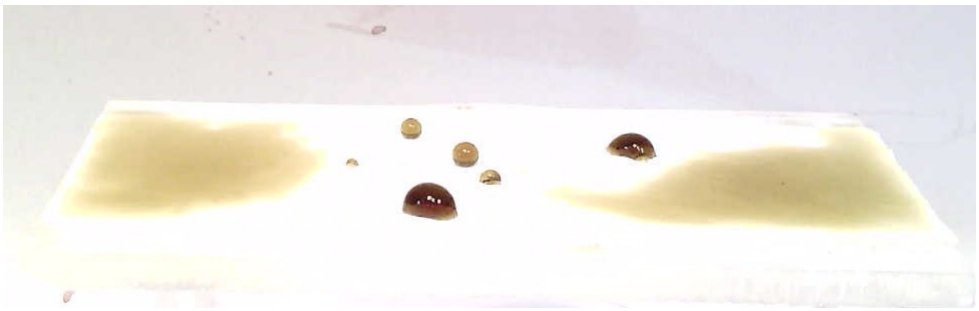

FIGURE A.6: Droplet of water resting on a surface coated with TiO_2 super-hydrophobic paint after 78 hours the preliminary experiment was initiated

A.3 NeverWet®

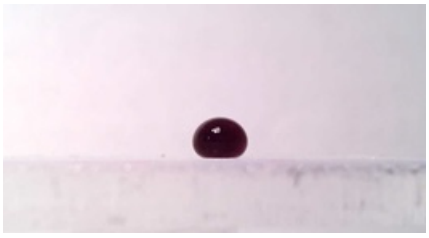

FIGURE A.7: Droplet of water resting on a surface coated with NeverWet® before the preliminary experiment was initiated

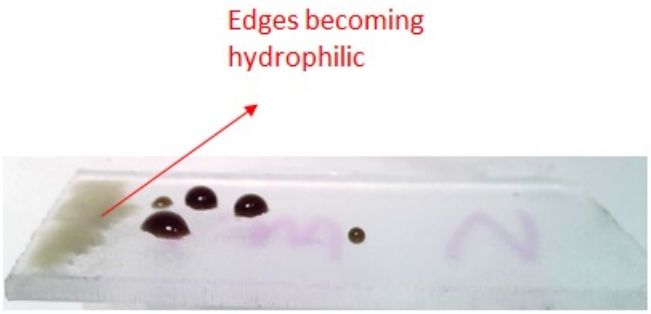

FIGURE A.8: Droplet of water resting on a surface coated with NeverWet® after 25 hours the preliminary experiment was initiated

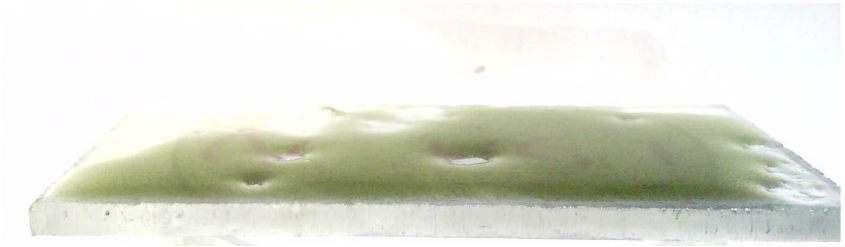

FIGURE A.9: Droplet of water resting on a surface coated with NeverWet® after 78 hours the preliminary experiment was initiated

B

Pressed soda-lime glass tiles

The first attempt of manufacturing a porous surface with the Cassie-Baxter state in this study was performed by following and modifying a method described in Pantz (2013). Soda-lime glass powder were mixed with a binder and pressed in a hydraulic press to form tiles that were fired at 680°. Samples manufactured following this procedure are more uniform than the procedure described in Chapter 3. They are produced with uniform dimensions and the binder keeps the particles together during handling of the material. The binder is non-toxic and consists of acrylamide copolymer. During sintering the binder decomposes into H_2O, NH_3, N_2, CO and CO_2 (Leung et al., 1987). The manufacturing procedure is described in this section.

B.1 Procedure

Step 1 Milling: Pieces of soda-lime glass was milled in a Hammer Mill in order to decrease the size of pieces into particles of size d$\leq$355 μm;

Step 2 Sieving: Five laboratory calibrated sieves were used to sort the particle sizes.

The sieves were mounted in series on a sieve shaker. The sieve apertures (μm) were the following: 355-212, 212-150, 150-75, 75-45 and <45;

Step 3 Mixing: 99 grams of each mixture of fine glass particles was mixed with 1 gram of Alcotac (binding agent, BASF®). Then, 10 mL of water is added to the mixture to provoke polymerization;

Step 4 Pressing: The mixture is pressed in pellets using a Nannetti hydraulic press (7 MPa);

Step 5 Drying: Pressed sample were dried at room temperature for 2 hours;

Step 6 Firing: The mixture is placed in a furnace pre-heated at 680°C for 30 minutes. The furnace is cooled down at a rate of 20°C/min. The sintered glass is taken out when the furnace is at a temperature below 200°C.

B.2 Results

Table B.1: Composition of samples and ideal firing temperatures

	Size range μm					Temperature (°C)	Contact angle
Sample id	355-212	212-150	150-75	75-45	<45		
A	1					680	105
B		1				680	112
C			1			680	110
D				1		680	113
E					1	660	136
F					1	670	112
G					1	680	95
H	0.5				0.5	680	118
I		0.5			0.5	680	113
J			0.5		0.5	680	110
K				0.5	0.5	680	105

None of the samples presented in Table 3.1 have water contact angles above 150 °, therefore are not super-hydrophobic. The contact angles of a water droplet on the surfaces presented in Table 3.1 are approximately 50 °below the ones presented by

Tao et al. (2016) and Crick & Parkin (2011). The highest contact angle in Table 3.1 was obtained for the surface formed with lowest particle size range (sample E). Sample F and G are variations of Sample E that were fired at higher temperatures which resulted in higher melting of the surface of the particles, and the relative roughness decreased.

C

Student's *t*-test of contact angle for free chlorine dependence

Student's *t*-test was applied to evaluate whether changes in the water contact angle of samples immersed in NaOCl solution were significantly different when comparing before and after immersion. Results are presented in tables C.1, C.2 and C.1, indicating that the water contact angles remained alike with 95% confidence.

TABLE C.1: Student's *t*-test results of contact angles measured from sample of 1 cm^2 surface area

	After	Before
Mean	161.16	157.27
Variance	4.69	20.86
Observations	14	23
Pooled Variance	14.85	
Hypothesized Mean Difference	0	
df	35	
t Stat	2.98	
P(T<=t) one-tail	2.60×10^{-3}	
t Critical one-tail	1.69	
P(T<=t) two-tail	5.21×10^{-3}	
t Critical two-tail	2.03	

TABLE C.2: Student's t-test results of contact angles measured from sample of 5 cm^2 surface area

	After	Before
Mean	159.71	156.84
Variance	20.20	12.79
Observations	33	65
Pooled Variance	15.26	
Hypothesized Mean Difference	0	
df	96	
t Stat	3.43	
P(T<=t) one-tail	4.42	
t Critical one-tail	1.66×10^{-4}	
P(T<=t) two-tail	8.85×10^{-4}	
t Critical two-tail	1.98	

TABLE C.3: Student's t-test results of contact angles measured from sample of 10 cm^2 surface area

	After	Before
Mean	161.09	156.94
Variance	15.62	12.21
Observations	30	65
Pooled Variance	13.27	
Hypothesized Mean Difference	0	
df	93	
t Stat	5.17	
P(T<=t) one-tail	6.66×10^{-7}	
t Critical one-tail	1.66	
P(T<=t) two-tail	1.33×10^{-6}	
t Critical two-tail	1.99	

D

Procedure to measure decay of free chlorine in NaOCl solution

D.1 Experimental procedure

This photometric method determines the concentration of free chlorine. In the absence of iodide ions, free chlorine (hypochlorous acid and hypochlorite ions) react instantly with Dialkyl-phenylenediamine to form a red dye. The intensity of the colour formed in both cases is measured photometrically. This method is capable of measuring free chlorine in the range of 0.05 to 6.0 mg/L.

D.1.1 Apparatus

a. Photometric equipment: spectrophotometer (for use at a wavelength of 515 nm);

D.1.2 Reagents and materials

a. Chlorine test Kit (free and total chlorine) Method: photometric, DPD 0.010 - 6.00 mg/l Cl_2 Spectroquant from Merck (ref 100599);

b. Super-hydrophobic soda-lime glass sample (sintered porous soda-lime glass with carbon-fluoride radical);

c. Sodium hypochlorite solution with 6-14% active chlorine.

D.1.3 Procedure

Step 1 Determine contact angle using Drop Shape Analyzer using ADVANCE software (DSA30, KRÜSS GmbH, Hambourg, Germany) for samples of size 1, 5 and 10 cm^2, then add one sample to each beaker;

Step 2 Add 100 mL of NaClO containing 6-14% active chlorine to each beaker;

Step 3 Take out 10 mL solution of the beakers at 15 min, 60 min, 120 min and 300 min for residual chlorine testing.

D.1.4 Method

Step 4 Calibration of photometric equipment: Potassium permanganate solutions-prepare a stock solution containing 891 mg $KMnO_4$/1000 mL. Dilute 10 mL stock solution to 100 mL with distilled water in a volumetric flask. When 1 mL of this solution is diluted to 100 mL, a chlorine equivalent of 1.00 mg/L will be produced in the DPD reaction procedure of Step 5;

Step 5 A 10 ml aliquot from Step 3 is transferred to a 16 × 100-mm test tube. The pH of new samples is checked. If the pH is outside the range of four to eight, adjust with dilute sodium hydroxide or sulfuric acid;

Step 6 N,N-Di-n-propyl-1,4 phenylenediamine DPD color indicator/EDTA buffer mixture (Spectroquant Reagent Cl2-1) is added to adjust the pH of the sample to 5.0 ± 0.5. Free Cl2 reacts with the DPD colour indicator to form a red dye;

Step 7 After a one minute reaction time, the solution is measured photometrically;

Step 8 The photometric measurements are conducted at or near 557 nm;

Step 9 Plot time vs concentration of residual chlorine vs time;

Step 10 Remove samples from beaker and let dry at room tenperature. Determine contact angle using Drop Shape Analyzer using ADVANCE software (DSA30, KRÜSS GmbH, Hambourg, Germany) for samples of size 1, 5 and 10 cm^2;

Step 11 Plot time vs contact angle graph; analysis whether the concentration of chlorine will impact the contact angle.

E

Enforcing volume conservation

Integrating equation 5.7 over z results in:

$$\int_0^h \frac{\partial u}{\partial x} dz + \int_0^h \frac{\partial w}{\partial z} dz = \frac{d}{dx} \int u dz + w(h) - w(0) = h \frac{dU}{dx} = 0 \tag{E.1}$$

where $U = 1/\delta \int u dz$ is the average depth velocity. The boundaries are impermeable, thus w=0. The pressure gradient $F(x)$ is responsible for ensuring that $\frac{dU}{dx} = 0$ and can be determined by rearranging the momentum equation:

$$\begin{aligned} 2u \frac{\partial u}{\partial x} &= \frac{\partial}{\partial z} \nu_t \frac{\partial u}{\partial z} + F \iff \\ \frac{\partial u}{\partial x} &= \frac{1}{2u} \frac{\partial}{\partial z} \nu_t \frac{\partial u}{\partial z} + \frac{1}{2u} F \end{aligned} \tag{E.2}$$

and integration over z:

$$\int_0^h \frac{\partial u}{\partial x} dz = \int_0^h \frac{1}{2u} \frac{\partial}{\partial z} \nu_t \frac{\partial u}{\partial z} dz + F \int_0^h \frac{1}{2u} dz \tag{E.3}$$

Volume conservation requires that the left-hand-side of the equation is zero, thus:

$$F(x) = -\int_0^h \frac{1}{2u}\frac{\partial}{\partial z}\left(\nu_t \frac{\partial u}{\partial z}\right) dz \Big/ \int_0^h \frac{1}{2u} dz \tag{E.4}$$

By calculating the pressure gradient F it is possible to calculate the difference and loss in pressure in the section, as well as the flow velocity at all points in the grid.

F

Raw values of channel flow experiment

F.1 Initial height: 0.22 m

TABLE F.1: Raw values of channel flow experiment

Time	**height (m)**	**z**	x **(m)**	**dL**	**Tank height reading (m)**	**Velocity**	**Re**	$\bar{f}_d$	f_B	f_d	**DR %**
10:23	0.216	0		0.043	0.374	1.285	40813	0.020	0.022	0.015	-30.8
	0.102	0.043		0.102							
	0.101	0.145		0.198							
	0.081	0.343		0.343							
	0.062	0.686		0.2							
	0.053	0.886		0.543							
10:35	0.216	0		0.043	0.372	1.260	40032	0.020	0.022	0.016	-27.8
	0.102	0.043		0.102							
	0.101	0.145		0.198							
	0.082	0.343		0.343							
	0.064	0.686		0.2							
	0.054	0.886		0.543							

10:45	0.216	0	0.043	0.373	1.260	40033	0.020	0.022	0.017	-23.0
	0.102	0.043	0.102							
	0.101	0.145	0.198							
	0.083	0.343	0.343							
	0.064	0.686	0.2							
	0.055	0.886	0.543							
10:55	0.216	0	0.043	0.373	1.259	39996	0.021	0.022	0.019	-14.1
	0.102	0.043	0.102							
	0.101	0.145	0.198							
	0.084	0.343	0.343							
	0.065	0.686	0.2							
	0.055	0.886	0.543							
11:12	0.216	0	0.043	0.372	1.260	40032	0.021	0.022	0.019	-13.6
	0.103	0.043	0.102							
	0.102	0.145	0.198							
	0.084	0.343	0.343							
	0.065	0.686	0.2							
	0.055	0.886	0.543							
11:20	0.216	0	0.043	0.356	1.261	40070	0.021	0.023	0.013	-12.9
	0.102	0.043	0.102							
	0.101	0.145	0.198							
	0.084	0.343	0.343							
	0.066	0.686	0.2							
	0.055	0.886	0.543							
11:38	0.216	0	0.043	0.356	1.261	40070	0.022	0.023	0.014	-10.5
	0.102	0.043	0.102							
	0.102	0.145	0.198							
	0.085	0.343	0.343							
	0.066	0.686	0.2							
	0.055	0.886	0.543							
	0.216	0	0.043	0.355	1.259	39994	0.023	0.023	0.016	-1.1
11:50	0.102	0.043	0.102							
	0.102	0.145	0.198							
	0.085	0.343	0.343							
	0.066	0.686	0.2							
	0.055	0.886	0.543							
12:20	0.216	0	0.043	0.355	1.259	39994	0.023	0.023	0.016	4.7
	0.103	0.043	0.102							
	0.102	0.145	0.198							
	0.087	0.343	0.343							
	0.066	0.686	0.2							
	0.056	0.886	0.543							
13	0.216	0	0.043	0.355	1.258	39956	0.025	0.023	0.018	16.7
	0.104	0.043	0.102							
	0.102	0.145	0.198							
	0.088	0.343	0.343							
	0.066	0.686	0.2							
	0.056	0.886	0.543							
13:25	0.216	0	0.043	0.354	1.255	39882	0.025	0.023	0.019	21.3
	0.104	0.043	0.102							
	0.102	0.145	0.198							
	0.088	0.343	0.343							

	0.066	0.686	0.2							
	0.055	0.886	0.543							
13:50	0.216	0	0.043	0.354	1.254	39845	0.025	0.023	0.020	23.7
	0.104	0.043	0.102							
	0.102	0.145	0.198							
	0.089	0.343	0.343							
	0.066	0.686	0.2							
	0.056	0.886	0.543							
	0.216	0	0.043	0.354	1.254	39845	0.025	0.023	0.020	23.7
14:20	0.098	0.043	0.102							
	0.104	0.145	0.198							
	0.089	0.343	0.343							
	0.066	0.686	0.2							
	0.055	0.886	0.543							
14:50	0.216	0	0.043	0.354	1.256	39900	0.025	0.023	0.020	24.1
	0.105	0.043	0.102							
	0.104	0.145	0.198							
	0.089	0.343	0.343							
	0.066	0.686	0.2							
	0.055	0.886	0.543							
15:20	0.216	0	0.043	0.354	1.256	39900	0.025	0.023	0.020	24.1
	0.105	0.043	0.102							
	0.104	0.145	0.198							
	0.089	0.343	0.343							
	0.066	0.686	0.2							
	0.055	0.886	0.543							
15:45	0.216	0	0.043	0.356	1.264	40146	0.023	0.023	0.016	-5.3
	0.106	0.043	0.102							
	0.104	0.145	0.198							
	0.086	0.343	0.343							
	0.067	0.686	0.2							
	0.056	0.886	0.543							
15:55	0.216	0	0.043	0.356	1.263	40107	0.021	0.023	0.013	-20.0
	0.105	0.043	0.102							
	0.102	0.145	0.198							
	0.084	0.343	0.343							
	0.066	0.686	0.2							
	0.056	0.886	0.543							
	0.216	0	0.043	0.356	1.263	40107	0.021	0.023	0.013	-17.1
16:05	0.105	0.043	0.102							
	0.101	0.145	0.198							
	0.085	0.343	0.343							
	0.065	0.686	0.2							
	0.056	0.886	0.543							
16:15	0.216	0	0.043	0.356	1.263	40107	0.022	0.023	0.013	-13.3
	0.104	0.043	0.102							
	0.101	0.145	0.198							
	0.085	0.343	0.343							
	0.066	0.686	0.2							
	0.056	0.886	0.543							
16:25	0.216	0	0.043	0.356	1.261	40069	0.022	0.023	0.014	-11.8

	0.105	0.043	0.102							
	0.101	0.145	0.198							
	0.085	0.343	0.343							
	0.066	0.686	0.2							
	0.056	0.886	0.543							
	0.216	0	0.043	0.357	1.265	40180	0.022	0.022	0.021	-7.4
16:40	0.105	0.043	0.102							
	0.101	0.145	0.198							
	0.086	0.343	0.343							
	0.065	0.686	0.2							
	0.056	0.886	0.543							
17	0.216	0	0.043	0.356	1.264	40143	0.022	0.022	0.022	-3.4
	0.105	0.043	0.102							
	0.102	0.145	0.198							
	0.086	0.343	0.343							
	0.065	0.686	0.2							
	0.056	0.886	0.543							
17:30	0.216	0	0.043	0.357	1.265	40179	0.023	0.022	0.023	2.9
	0.105	0.043	0.102							
	0.102	0.145	0.198							
	0.087	0.343	0.343							
	0.066	0.686	0.2							
	0.056	0.886	0.543							
18	0.216	0	0.043	0.357	1.266	40217	0.023	0.022	0.024	8.1
	0.105	0.043	0.102							
	0.102	0.145	0.198							
	0.088	0.343	0.343							
	0.066	0.686	0.2							
	0.056	0.886	0.543							
18:30	0.216	0	0.043	0.356	1.264	40141	0.024	0.022	0.025	13.9
	0.105	0.043	0.102							
	0.102	0.145	0.198							
	0.089	0.343	0.343							
	0.066	0.686	0.2							
	0.056	0.886	0.543							
	0.216	0	0.043	0.354	1.257	39919	0.024	0.022	0.027	19.6
	0.105	0.043	0.102							
19	0.102	0.145	0.198							
	0.089	0.343	0.343							
	0.066	0.686	0.2							
	0.056	0.886	0.543							
	0.216	0	0.043	0.355	1.258	39956	0.024	0.022	0.027	21.5
19:30	0.105	0.043	0.102							
	0.102	0.145	0.198							
	0.089	0.343	0.343							
	0.067	0.686	0.2							
	0.056	0.886	0.543							
	0.216	0	0.043	0.355	1.257	39937	0.025	0.022	0.028	25.9
20	0.105	0.043	0.102							
	0.102	0.145	0.198							
	0.089	0.343	0.343							

	0.067	0.686	0.2							
	0.056	0.886	0.543							
	0.216	0	0.043	0.354	1.257	39918	0.025	0.022	0.028	26.7
20:30	0.105	0.043	0.102							
	0.102	0.145	0.198							
	0.089	0.343	0.343							
	0.066	0.686	0.2							
	0.055	0.886	0.543							
20:50	0.216	0	0.043	0.372	1.319	41892	0.019	0.022	0.015	-32.3
	0.097	0.043	0.102							
	0.096	0.145	0.198							
	0.085	0.343	0.343							
	0.065	0.686	0.2							
	0.056	0.886	0.543							

F.2 Initial height: 0.24 m

Table F.2: Raw values of channel flow experiment

Time	height (m)	z	x (m)	dL	Tank height reading (m)	Velocity	Re	$\bar{f}_d$	f_B	f_d	DR %
10:50	0.236	0		0.043	0.37	1.325	42911	0.020	0.022	0.016	-19.7
		0.043		0.102							
	0.105	0.145		0.198							
	0.091	0.343		0.343							
	0.072	0.686		0.2							
	0.062	0.886		0.543							
11	0.236	0		0.043	0.37	1.313	42528	0.021	0.022	0.021	-4.0
		0.043		0.102							
	0.107	0.145		0.198							
	0.094	0.343		0.343							
	0.075	0.686		0.2							
	0.062	0.886		0.543							
11:10	0.236	0		0.043	0.37	1.306	42298	0.022	0.022	0.021	-2.5
		0.043		0.102							
	0.109	0.145		0.198							
	0.095	0.343		0.343							
	0.076	0.686		0.2							
	0.063	0.886		0.543							
11:20	0.236	0		0.043	0.37	1.300	42107	0.023	0.022	0.023	3.6
		0.043		0.102							
	0.110	0.145		0.198							
	0.096	0.343		0.343							
	0.075	0.686		0.2							
	0.063	0.886		0.543							
11:30	0.236	0		0.043	0.37	1.306	42298	0.023	0.022	0.024	5.7
		0.043		0.102							
	0.117	0.145		0.198							
	0.096	0.343		0.343							
	0.075	0.686		0.2							
	0.063	0.886		0.543							
11:40	0.236	0		0.043	0.37	1.303	42183	0.023	0.022	0.026	9.4
		0.043		0.102							
	0.117	0.145		0.198							
	0.097	0.343		0.343							
	0.076	0.686		0.2							
	0.063	0.886		0.543							
11:50	0.236	0		0.043	0.37	1.303	42183	0.024	0.022	0.027	11.8
		0.043		0.102							
	0.117	0.145		0.198							
	0.098	0.343		0.343							
	0.076	0.686		0.2							

	0.063	0.886	0.543							
12:20	0.236	0	0.043	0.37	1.302	42145	0.024	0.022	0.027	13.3
		0.043	0.102							
	0.110	0.145	0.198							
	0.098	0.343	0.343							
	0.076	0.686	0.2							
	0.063	0.886	0.543							
12:50	0.236	0	0.043	0.37	1.300	42107	0.025	0.022	0.029	17.0
		0.043	0.102							
	0.111	0.145	0.198							
	0.099	0.343	0.343							
	0.076	0.686	0.2							
	0.063	0.886	0.543							
13:20	0.236	0	0.043	0.37	1.300	42107	0.025	0.022	0.029	18.0
		0.043	0.102							
	0.111	0.145	0.198							
	0.099	0.343	0.343							
	0.076	0.686	0.2							
	0.063	0.886	0.543							
13:50	0.236	0	0.043	0.37	1.302	42145	0.025	0.022	0.029	17.8
		0.043	0.102							
	0.112	0.145	0.198							
	0.099	0.343	0.343							
	0.076	0.686	0.2							
	0.063	0.886	0.543							
14:20	0.236	0	0.043	0.37	1.302	42145	0.025	0.022	0.029	17.8
		0.043	0.102							
	0.112	0.145	0.198							
	0.099	0.343	0.343							
	0.076	0.686	0.2							
	0.063	0.886	0.543							
14:50	0.236	0	0.043	0.37	1.302	42145	0.025	0.022	0.029	17.8
		0.043	0.102							
	0.112	0.145	0.198							
	0.099	0.343	0.343							
	0.076	0.686	0.2							
	0.063	0.886	0.543							
15:20	0.236	0	0.043	0.37	1.302	42145	0.025	0.022	0.029	17.8
		0.043	0.102							
	0.112	0.145	0.198							
	0.099	0.343	0.343							
	0.076	0.686	0.2							
	0.063	0.886	0.543							
15:50	0.236	0	0.043	0.37	1.302	42145	0.025	0.022	0.030	18.3
		0.043	0.102							
	0.112	0.145	0.198							
	0.099	0.343	0.343							
	0.076	0.686	0.2							
	0.063	0.886	0.543							
16:05	0.236	0	0.043	0.37	1.312	42490	0.020	0.022	0.017	-15.3
		0.043	0.102							
	0.110	0.145	0.198							

	0.095	0.343	0.343							
	0.074	0.686	0.2							
	0.065	0.886	0.543							
16:15	0.236	0	0.043	0.37	1.310	42413	0.021	0.022	0.020	-7.2
		0.043	0.102							
	0.110	0.145	0.198							
	0.096	0.343	0.343							
	0.075	0.686	0.2							
	0.064	0.886	0.543							
16:25	0.236	0	0.043	0.37	1.306	42298	0.022	0.022	0.021	-2.2
		0.043	0.102							
	0.110	0.145	0.198							
	0.097	0.343	0.343							
	0.076	0.686	0.2							
	0.065	0.886	0.543							
16:35	0.236	0	0.043	0.37	1.306	42298	0.022	0.022	0.022	-1.4
		0.043	0.102							
	0.110	0.145	0.198							
	0.097	0.343	0.343							
	0.075	0.686	0.2							
	0.065	0.886	0.543							
16:45	0.236	0	0.043	0.37	1.306	42298	0.022	0.022	0.022	0.7
		0.043	0.102							
	0.110	0.145	0.198							
	0.097	0.343	0.343							
	0.076	0.686	0.2							
	0.065	0.886	0.543							
16:55	0.236	0	0.043	0.37	1.306	42298	0.022	0.022	0.023	2.1
		0.043	0.102							
	0.110	0.145	0.198							
	0.097	0.343	0.343							
	0.075	0.686	0.2							
	0.064	0.886	0.543							
17:05	0.236	0	0.043	0.37	1.309	42375	0.022	0.022	0.023	2.2
		0.043	0.102							
	0.110	0.145	0.198							
	0.098	0.343	0.343							
	0.076	0.686	0.2							
	0.065	0.886	0.543							
17:35	0.236	0	0.043	0.368	1.309	42375	0.023	0.022	0.023	3.5
		0.043	0.102							
	0.110	0.145	0.198							
	0.098	0.343	0.343							
	0.076	0.686	0.2							
	0.065	0.886	0.543							
18:05	0.236	0	0.043	0.367	1.305	42260	0.023	0.022	0.025	7.4
		0.043	0.102							
	0.110	0.145	0.198							
	0.098	0.343	0.343							
	0.076	0.686	0.2							
	0.064	0.886	0.543							

18:35	0.236	0	0.043	0.367	1.302	42145	0.024	0.022	0.026	9.9
		0.043	0.102							
	0.110	0.145	0.198							
	0.098	0.343	0.343							
	0.076	0.686	0.2							
	0.064	0.886	0.543							
19:05	0.236	0	0.043	0.368	1.304	42222	0.024	0.022	0.026	11.3
		0.043	0.102							
	0.110	0.145	0.198							
	0.099	0.343	0.343							
	0.076	0.686	0.2							
	0.064	0.886	0.543							
19:35	0.236	0	0.043	0.367	1.305	42260	0.024	0.022	0.027	11.6
		0.043	0.102							
	0.110	0.145	0.198							
	0.099	0.343	0.343							
	0.076	0.686	0.2							
	0.064	0.886	0.543							
20:05	0.236	0	0.043	0.367	1.304	42222	0.024	0.022	0.027	12.4
		0.043	0.102							
	0.110	0.145	0.198							
	0.099	0.343	0.343							
	0.076	0.686	0.2							
	0.064	0.886	0.543							
20:35	0.236	0	0.043	0.367	1.304	42222	0.024	0.022	0.027	12.4
		0.043	0.102							
	0.110	0.145	0.198							
	0.099	0.343	0.343							
	0.076	0.686	0.2							
	0.064	0.886	0.543							
21:05	0.236	0	0.043	0.367	1.304	42222	0.024	0.022	0.027	12.4
		0.043	0.102							
	0.110	0.145	0.198							
	0.099	0.343	0.343							
	0.076	0.686	0.2							
	0.064	0.886	0.543							
21:20	0.236	0	0.043	0.371	1.316	42604	0.020	0.022	0.018	-13.1
		0.043	0.102							
	0.108	0.145	0.198							
	0.095	0.343	0.343							
	0.075	0.686	0.2							
	0.065	0.886	0.543							

F.3 Initial height: 0.27 m

Table F.3: Raw values of channel flow experiment

Time	height (m)	z	x (m)	dL	Tank height reading (m)	Velocity	Re	$\bar{f}_d$	f_B	f_d	DR %
11:45	0.266	0.000	0.043	0.397	1.408	45590	0.019	0.022	0.015	-29.3	
		0.043	0.102								
	0.120	0.145	0.198								
	0.102	0.343	0.343								
	0.084	0.686	0.200								
	0.070	0.886	0.543								
11:55	0.266	0.000	0.043	0.393	1.395	45169	0.022	0.022	0.021	-1.0	
		0.043	0.102								
	0.123	0.145	0.198								
	0.107	0.343	0.343								
	0.084	0.686	0.200								
	0.071	0.886	0.543								
12:05	0.266	0.000	0.043	0.392	1.391	45054	0.023	0.022	0.026	18.1	
		0.043	0.102								
	0.129	0.145	0.198								
	0.109	0.343	0.343								
	0.085	0.686	0.200								
	0.070	0.886	0.543								
12:15	0.266	0.000	0.043	0.393	1.395	45169	0.023	0.022	0.026	20.9	
		0.043	0.102								
	0.129	0.145	0.198								
	0.109	0.343	0.343								
	0.084	0.686	0.200								
	0.070	0.886	0.543								
12:25	0.266	0.000	0.043	0.393	1.393	45093	0.024	0.022	0.027	22.9	
		0.043	0.102								
	0.129	0.145	0.198								
	0.109	0.343	0.343								
	0.084	0.686	0.200								
	0.070	0.886	0.543								
12:35	0.266	0.000	0.043	0.393	1.393	45093	0.024	0.022	0.027	23.2	
		0.043	0.102								
	0.129	0.145	0.198								
	0.109	0.343	0.343								
	0.083	0.686	0.200								
	0.070	0.886	0.543								
12:45	0.266	0.000	0.043	0.394	1.397	45246	0.024	0.022	0.027	24.5	
		0.043	0.102								
	0.129	0.145	0.198								
	0.109	0.343	0.343								
	0.083	0.686	0.200								

	0.069	0.886	0.543							
13:15	0.266	0.000	0.043	0.394	1.397	45246	0.024	0.022	0.028	31.2
		0.043	0.102							
	0.130	0.145	0.198							
	0.110	0.343	0.343							
	0.084	0.686	0.200							
	0.069	0.886	0.543							
13:45	0.266	0.000	0.043	0.394	1.397	45246	0.024	0.022	0.028	31.2
		0.043	0.102							
	0.130	0.145	0.198							
	0.110	0.343	0.343							
	0.084	0.686	0.200							
	0.069	0.886	0.543							
14:15	0.266	0.000	0.043	0.394	1.397	45246	0.024	0.022	0.028	31.2
		0.043	0.102							
	0.130	0.145	0.198							
	0.110	0.343	0.343							
	0.084	0.686	0.200							
	0.069	0.886	0.543							
14:45	0.266	0.000	0.043	0.394	1.398	45284	0.024	0.022	0.029	31.8
		0.043	0.102							
	0.130	0.145	0.198							
	0.110	0.343	0.343							
	0.084	0.686	0.200							
	0.069	0.886	0.543							
15:15	0.266	0.000	0.043	0.394	1.397	45246	0.024	0.022	0.028	31.5
		0.043	0.102							
	0.130	0.145	0.198							
	0.111	0.343	0.343							
	0.084	0.686	0.200							
	0.070	0.886	0.543							
15:45	0.266	0.000	0.043	0.394	1.397	45246	0.024	0.022	0.028	31.5
		0.043	0.102							
	0.130	0.145	0.198							
	0.111	0.343	0.343							
	0.084	0.686	0.200							
	0.070	0.886	0.543							
16:15	0.266	0.000	0.043	0.394	1.397	45246	0.024	0.022	0.028	31.5
		0.043	0.102							
	0.130	0.145	0.198							
	0.111	0.343	0.343							
	0.084	0.686	0.200							
	0.070	0.886	0.543							
16:45	0.266	0.000	0.043	0.395	1.401	45361	0.023	0.022	0.026	21.1
		0.043	0.102							
	0.130	0.145	0.198							
	0.110	0.343	0.343							
	0.084	0.686	0.200							
	0.070	0.886	0.543							
17:00	0.266	0.000	0.043	0.396	1.406	45514	0.021	0.022	0.019	-13.4
		0.043	0.102							
	0.130	0.145	0.198							

	0.106	0.343	0.343							
	0.084	0.686	0.200							
	0.071	0.886	0.543							
17:10										
	0.266	0.000	0.043	0.396	1.404	45475	0.021	0.022	0.021	-2.5
		0.043	0.102							
	0.130	0.145	0.198							
	0.106	0.343	0.343							
	0.084	0.686	0.200							
	0.070	0.886	0.543							
	0.043									
17:20	0.266	0.000	0.043	0.395	1.402	45399	0.022	0.022	0.023	7.9
		0.043	0.102							
	0.130	0.145	0.198							
	0.107	0.343	0.343							
	0.086	0.686	0.200							
	0.070	0.886	0.543							
17:30										
	0.266	0.000	0.043	0.396	1.404	45475	0.023	0.022	0.025	16.6
		0.043	0.102							
	0.130	0.145	0.198							
	0.109	0.343	0.343							
	0.085	0.686	0.200							
17:40	0.070	0.886	0.543							
	0.266	0.000	0.043	0.395	1.401	45361	0.023	0.022	0.026	17.8
		0.043	0.102							
	0.130	0.145	0.198							
	0.109	0.343	0.343							
	0.085	0.686	0.200							
	0.070	0.886	0.543							
17:50	0.266	0.000	0.043	0.394	1.397	45246	0.023	0.022	0.026	20.1
		0.043	0.102							
	0.130	0.145	0.198							
	0.109	0.343	0.343							
	0.084	0.686	0.200							
	0.070	0.886	0.543							
18:00										
	0.266	0.000	0.043	0.395	1.401	45361	0.023	0.022	0.026	19.8
		0.043	0.102							
	0.130	0.145	0.198							
	0.109	0.343	0.343							
	0.084	0.686	0.200							
	0.070	0.886	0.543							
	0.266	0.000	0.043	0.394	1.397	45246	0.023	0.022	0.026	20.1
18:30		0.043	0.102							
	0.130	0.145	0.198							
	0.109	0.343	0.343							
	0.084	0.686	0.200							
	0.070	0.886	0.543							
19:00	0.266	0.000	0.043	0.394	1.396	45207	0.024	0.022	0.027	23.7
		0.043	0.102							
	0.130	0.145	0.198							
	0.109	0.343	0.343							
	0.084	0.686	0.200							
	0.070	0.886	0.543							

	0.266	0.000	0.043	0.394	1.398	45284	0.024	0.022	0.028	27.9
19:30		0.043	0.102							
	0.130	0.145	0.198							
	0.110	0.343	0.343							
	0.084	0.686	0.200							
	0.069	0.886	0.543							
20:00	0.266	0.000	0.043	0.394	1.397	45246	0.024	0.022	0.028	30.3
		0.043	0.102							
	0.130	0.145	0.198							
	0.110	0.343	0.343							
	0.084	0.686	0.200							
	0.069	0.886	0.543							
20:30	0.266	0.000	0.043	0.394	1.397	45246	0.025	0.022	0.029	33.9
		0.043	0.102							
	0.130	0.145	0.198							
	0.110	0.343	0.343							
	0.083	0.686	0.200							
	0.069	0.886	0.543							
21:00	0.266	0.000	0.043	0.394	1.397	45246	0.025	0.022	0.029	33.9
		0.043	0.102							
	0.130	0.145	0.198							
	0.110	0.343	0.343							
	0.083	0.686	0.200							
	0.069	0.886	0.543							
21:30	0.266	0.000	0.043	0.394	1.397	45246	0.025	0.022	0.029	33.9
		0.043	0.102							
	0.130	0.145	0.198							
	0.110	0.343	0.343							
	0.083	0.686	0.200							
	0.069	0.886	0.543							
	0.266	0.000	0.043	0.394	1.397	45246	0.025	0.022	0.029	33.9
22:00		0.043	0.102							
	0.130	0.145	0.198							
	0.110	0.343	0.343							
	0.083	0.686	0.200							
	0.069	0.886	0.543							
22:15	0.266	0.000	0.043	0.396	1.404	45475	0.020	0.022	0.017	-21.6
		0.043	0.102							
	0.130	0.145	0.198							
	0.105	0.343	0.343							
	0.082	0.686	0.200							
	0.071	0.886	0.543							